SAND88-2895

Dynamic Simulation of a Molten-Salt Solar Receiver

Gregory J. Kolb
Douglas Neary
Michael R. Ringham
Terry L. Greenlee

Sandia National Laboratories

Prepared by
Sandia National Laboratories
Albuquerque, New Mexico 87185 and Livermore, California 94550
for the United States Department of Energy
under Contract DE-AC04-76DP00789

Issued by Sandia National Laboratories, operated for the United States Department of Energy by Sandia Corporation.

Printed in the United States of America
Available from
National Technical Information Service
U.S. Department of Commerce
5285 Port Royal Road
Springfield, VA 22161

NTIS price codes
Printed copy: A04
Microfiche copy: A01

Distribution
Category UC-235

SAND88-2895
Unlimited Release
Printed March 1989

Dynamic Simulation of a Molten-Salt Solar Receiver

Gregory J. Kolb
Division 6217
Sandia National Laboratories
Albuquerque, NM 87185-5800

Douglas Neary
Michael R. Ringham
Terry L. Greenlee
ESSCOR Corporation
512 Via de la Valle, Suite 311
Solana Beach, CA 92075

ABSTRACT

A dynamic simulation model of the solar subsystem of a molten-salt-in-tube central receiver power plant was constructed. It consists of 132 ordinary differential equations and is programmed in the System Simulation Language. The model was validated with experimental data obtained at the Central Receiver Test Facility and was shown to accurately predict actual receiver performance. It can be used to perform the following types of studies: (1) optimization of control algorithms for salt-in-tube receiver plants, (2) analysis of system performance during transient conditions, (3) response of the system following component failures, and (4) optimization of power production. The model is user friendly, includes several real-time graphic displays, and runs real time on a personal computer.

Acknowledgments

The authors would like to thank Gene Riley and Jim Grossman for providing much of the experimental data used in this analysis. Doug Adkins and Jim Pacheco provided excellent technical comments on the draft report. We also appreciate the efforts of Anne Poore and Jeana Pineau in helping us edit and prepare the final manuscript.

Table of Contents

Chapter 1

Introduction

In order to improve the design of solar-central-receiver systems, it is important to understand their performance during non-steady-state conditions. In addition, U. S. utilities who are interested in adding central receiver power plants to their generation base in the future, identified performance prediction as a major uncertainty issue that requires resolution (Arizona Public Service and Pacific Gas and Electric 1988). For these reasons, we developed a computer model of a molten-salt solar receiver system. The receiver system that we modeled was tested at the Central Receiver Test Facility (CRTF) at Sandia National Laboratories during 1986 and 1987 (Chavez and Smith 1988). We will show that the model accurately predicts actual system performance (i.e., within 5.5 percent). This should alleviate some of the concerns expressed by the U. S. utilities. The accuracy of the model also assures that it will be useful in future design improvement studies.

This report documents the development and validation of the PC-based simulator. The system we modeled consists of a cavity-type receiver, a thermal storage subsystem, and a heat rejection system. The 5-MW_t receiver has two flow paths, designated east and west, in which molten salt is used as the heat transfer fluid. A detailed system description can be found in Chavez and Smith. A brief overview of the system design is presented at the beginning of Chapter 2. Figure 1-1 presents a modeling schematic. The heat rejection system was not modeled.

The model can be utilized with either the simulator or analyzer interfaces. Both interfaces allow selected simulation outputs to be monitored as the simulation progresses. Both interfaces allow the user to modify selected input variables at any time. The interfaces differ principally in the method of display and in flexibility in terms of changing the display variables.

The simulator interface consists of ten color-background screens drawn with a commercial paint program. This interface is user-friendly; a detailed understanding of the simulator is not required to use it. Simulation variables are overlaid and updated at selected intervals. The identity of the variables is preselected for each of the ten background screens. The user can change background screens, but for a given screen, has access only to the preselected variables.

Black and white versions of the ten color screens are displayed in Figures 1-2 through 1-11. Figure 1-2 is the main menu. This screen provides access to the nine remaining screens. Figure 1-3 is the overall system schematic. This screen is accessed when the user wants a global understanding of the entire system. Figures 1-4, 1-5, and 1-6 provide detailed information regarding the performance of the receiver. Solar power incident on the receiver, salt temperatures, and tube temperatures are displayed, respectively. The height of the vertical bars changes during the simulation in proportion to the receiver powers and temperatures. The motion of these bars gives the user an intuitive feeling for the process dynamics. Figures 1-7 and 1-8 are simplified schematics of the receiver control system for the east and west flow paths. The valve in the lower right-hand corner of the screen is opened and closed by control signals originating from signals depicted in the remaining three corners of the screen. This screen is useful in understanding the performance of the individual control loops. Cloud transients are initiated from these screens by activating insolation switches. Figures 1-9 and 1-10 display additional control system information. These screens are used to change set points, adjust gains, and to activate manual control of the simulation. In the latter mode, the automatic control system is deactivated, and the user attempts to control the process manually. The final screen, Figure 1-11, is used to initiate component failure transients. The seven valves listed in Figure 1-11 (see Figure 1-1 for locations of these valves within the system) can be failed in either the open or closed position.

The analyzer interface is a single screen, without background, displaying ten variables. The user can reassign any or all variables as well as the values of the independent variables at any time. The analyzer is generally preferred for model development and analysis when the user is intimately familiar with the variable names and does not need a process or control schematic as background. A user who is less familiar with the variables' names would prefer the simulator interface, with its effective graphic display and user-friendly menus. Both versions provide a variety of printed or plotted output upon request.

This report is organized into four chapters and one appendix.

In Chapter 2 we present an overview of the system and discuss the development of the analytical model. The model is composed of 132 ordinary differential equations (ODEs) and associated algebraic equations. These equations were coded in Fortran and integrated into a system-level model using the SYSL simulation language (E^2 Consulting 1985). They can be solved at greater than real-time speeds on a personal computer. Also in Chapter 2, we demonstrate the capabilities of the model by simulating the failure of one of the valves listed in Figure 1-11.

In Chapter 3 we discuss the validation of the model with experimental data. We show that the model provides an excellent estimate of the actual receiver performance. For example, during 3 hours of continuous cloud transients, the actual and predicted energy produced by the receiver were within 5.5 percent.

Conclusions and recommendations are drawn in Chapter 4.

Appendix A relates the hardware and software requirements of the simulator/analyzer. Names and addresses of resource persons are also listed here.

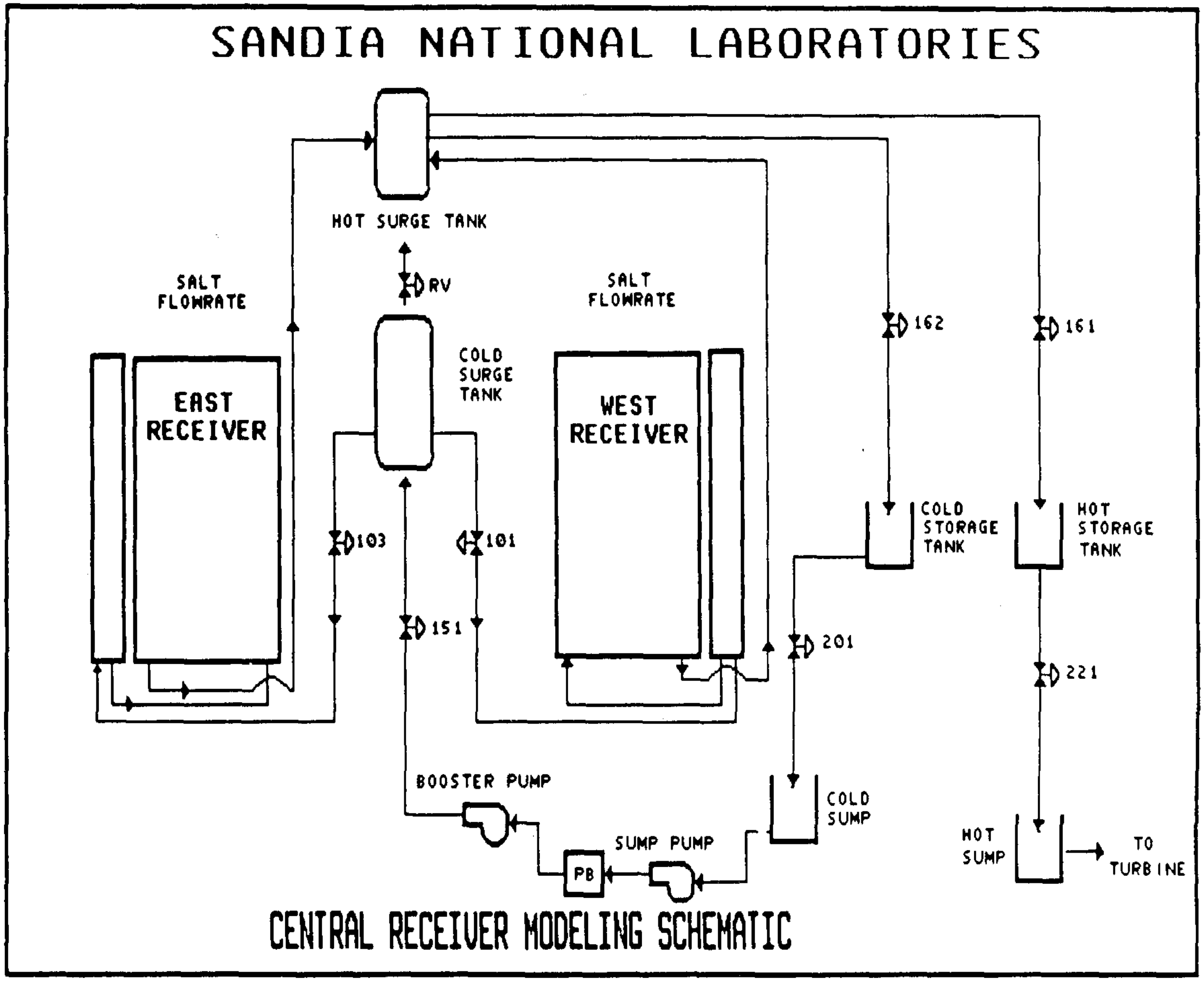

Figure 1-1 Modeling Schematic

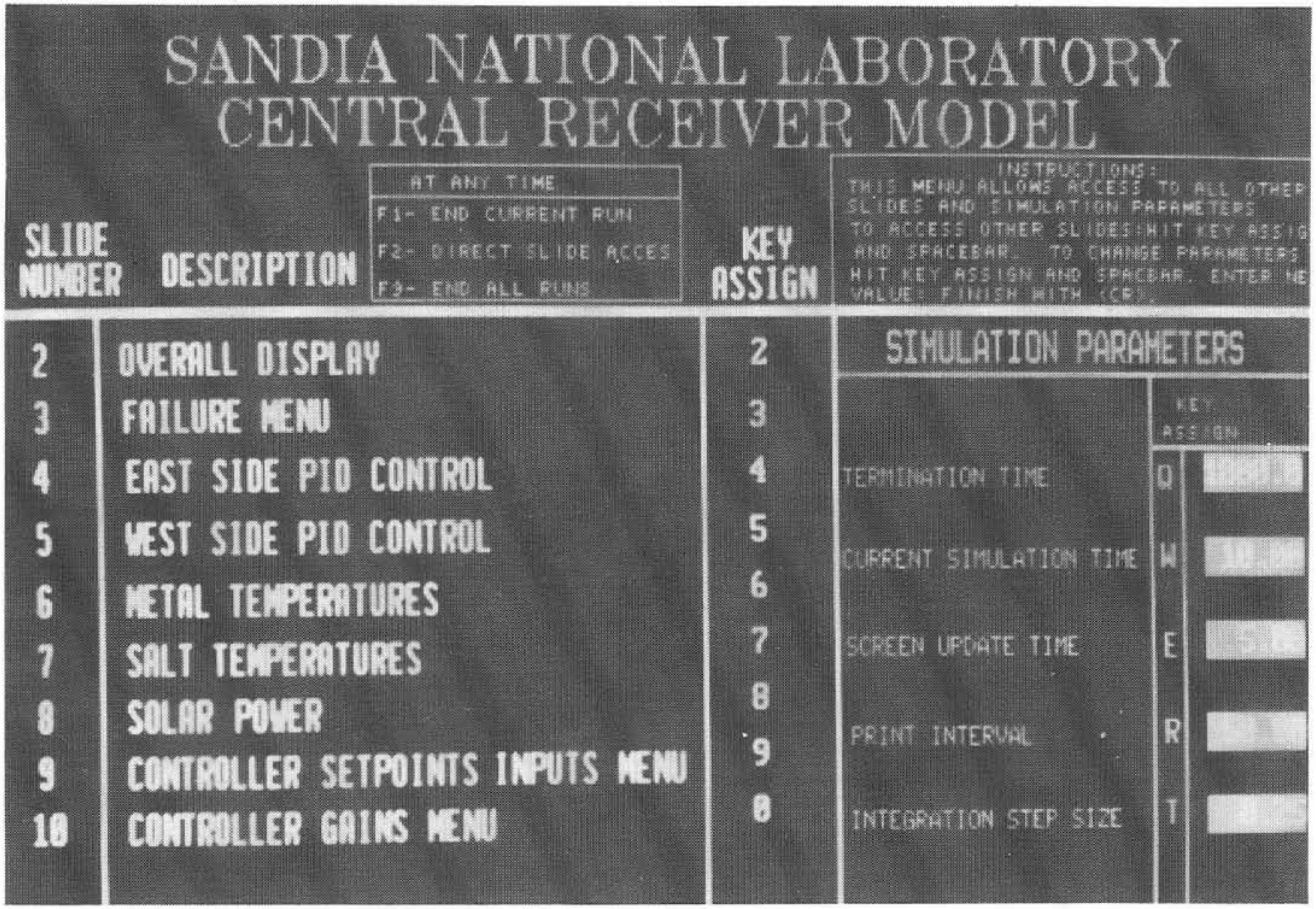

SANDIA NATIONAL LABORATORY
CENTRAL RECEIVER MODEL

AT ANY TIME
F1- END CURRENT RUN
F2- DIRECT SLIDE ACCES
F3- END ALL RUNS

INSTRUCTIONS:
THIS MENU ALLOWS ACCESS TO ALL OTHER SLIDES AND SIMULATION PARAMETERS
TO ACCESS OTHER SLIDES:HIT KEY ASSIG AND SPACEBAR. TO CHANGE PARAMETERS HIT KEY ASSIGN AND SPACEBAR. ENTER NE VALUE: FINISH WITH (CR).

SLIDE NUMBER	DESCRIPTION	KEY ASSIGN
2	OVERALL DISPLAY	2
3	FAILURE MENU	3
4	EAST SIDE PID CONTROL	4
5	WEST SIDE PID CONTROL	5
6	METAL TEMPERATURES	6
7	SALT TEMPERATURES	7
8	SOLAR POWER	8
9	CONTROLLER SETPOINTS INPUTS MENU	9
10	CONTROLLER GAINS MENU	0

SIMULATION PARAMETERS

	KEY ASSIGN	
TERMINATION TIME	Q	[illegible]
CURRENT SIMULATION TIME	W	[illegible]
SCREEN UPDATE TIME	E	[illegible]
PRINT INTERVAL	R	[illegible]
INTEGRATION STEP SIZE	T	[illegible]

Figure 1-2 Main Menu

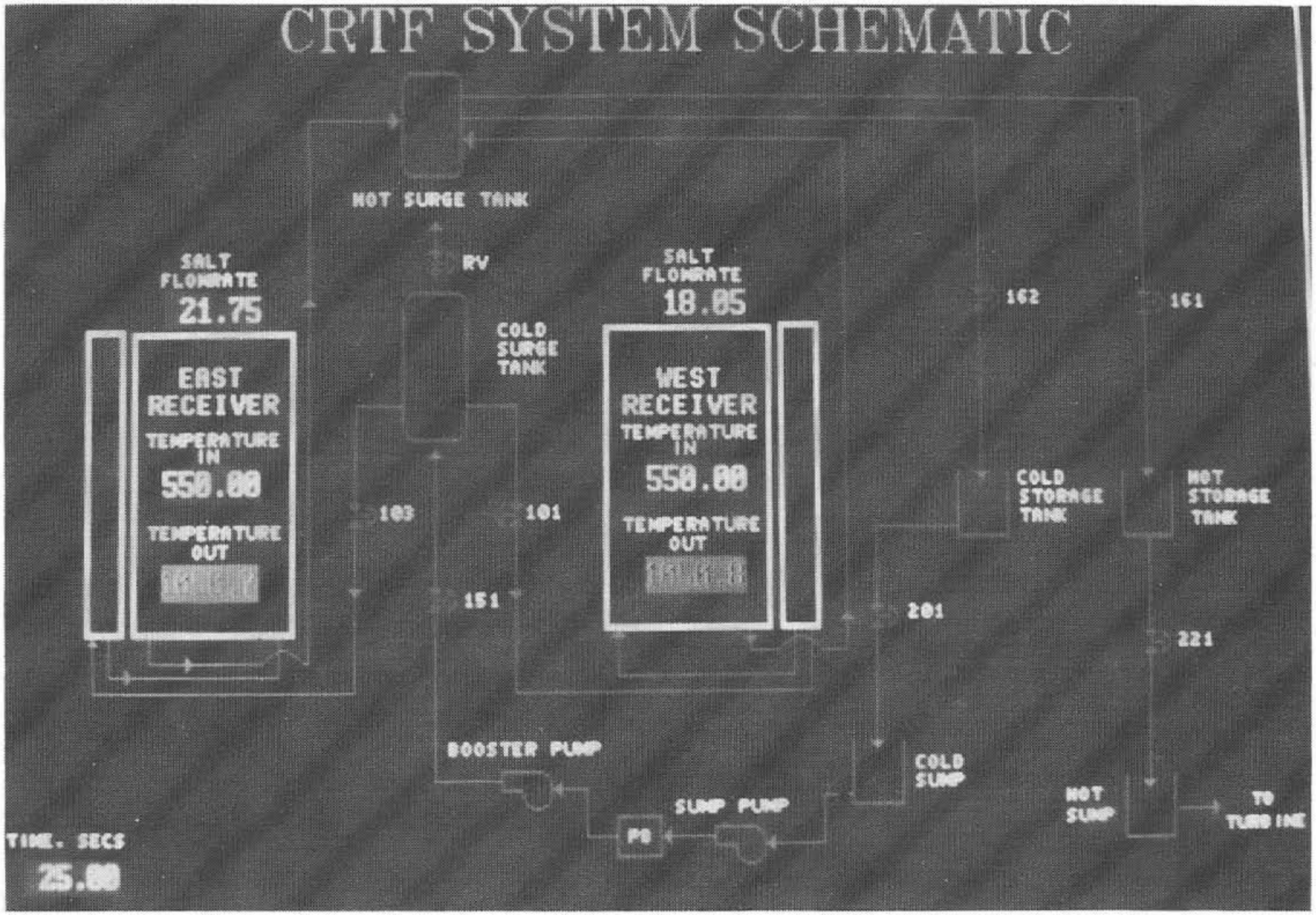

Figure 1-3 System Schematic

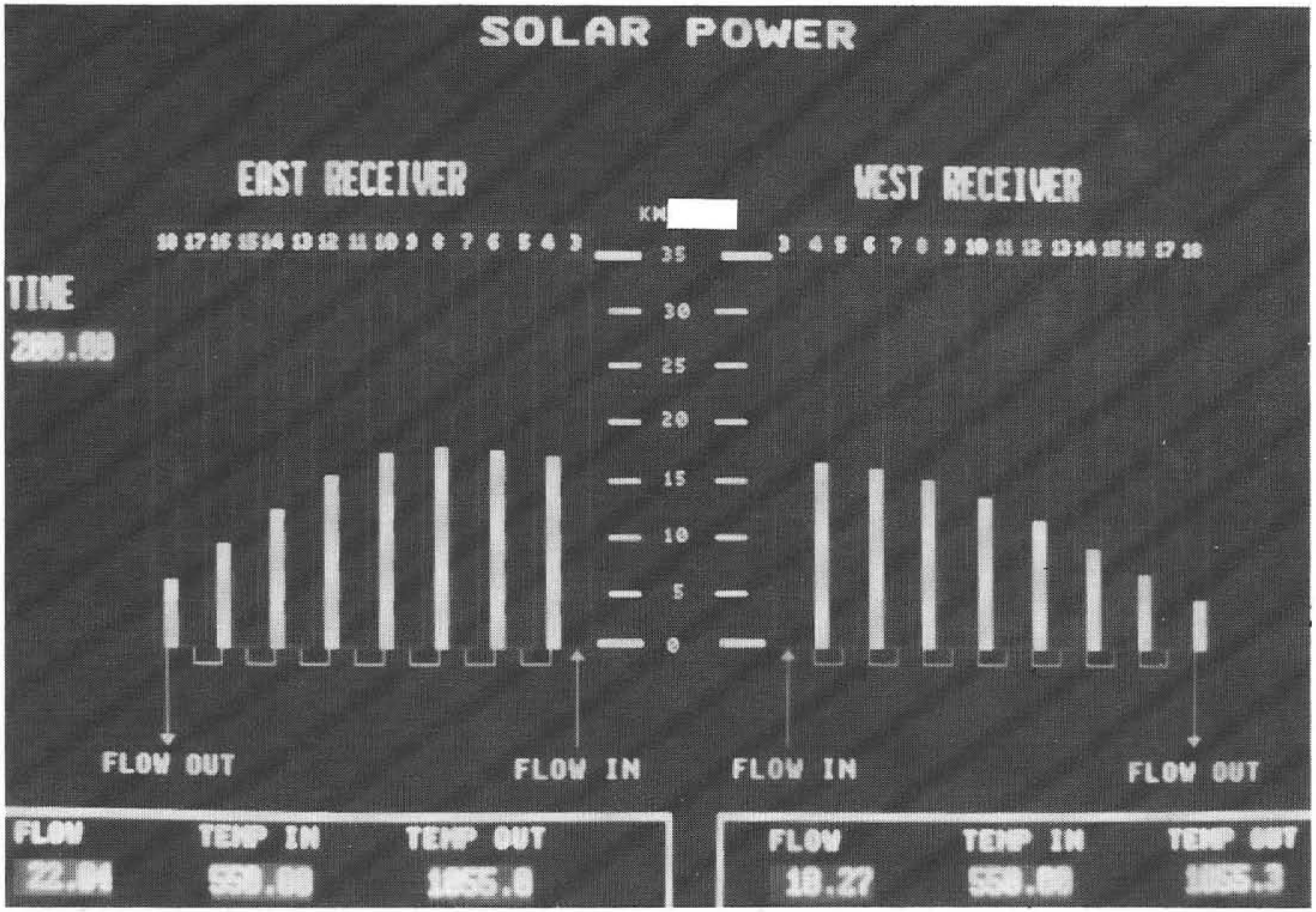

Figure 1-4 Solar Power Incident on the Receiver

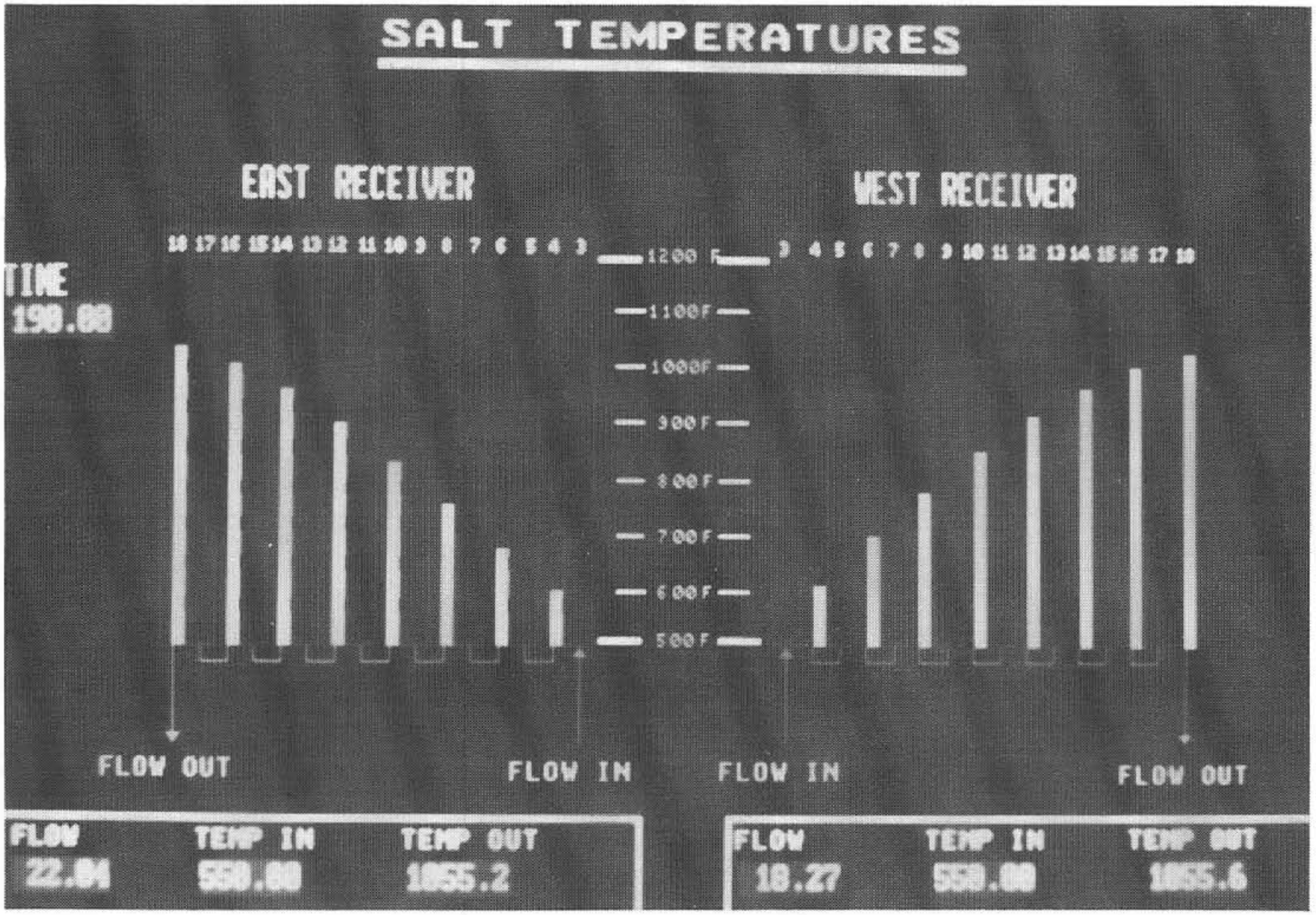

Figure 1-5 Receiver Salt Temperatures

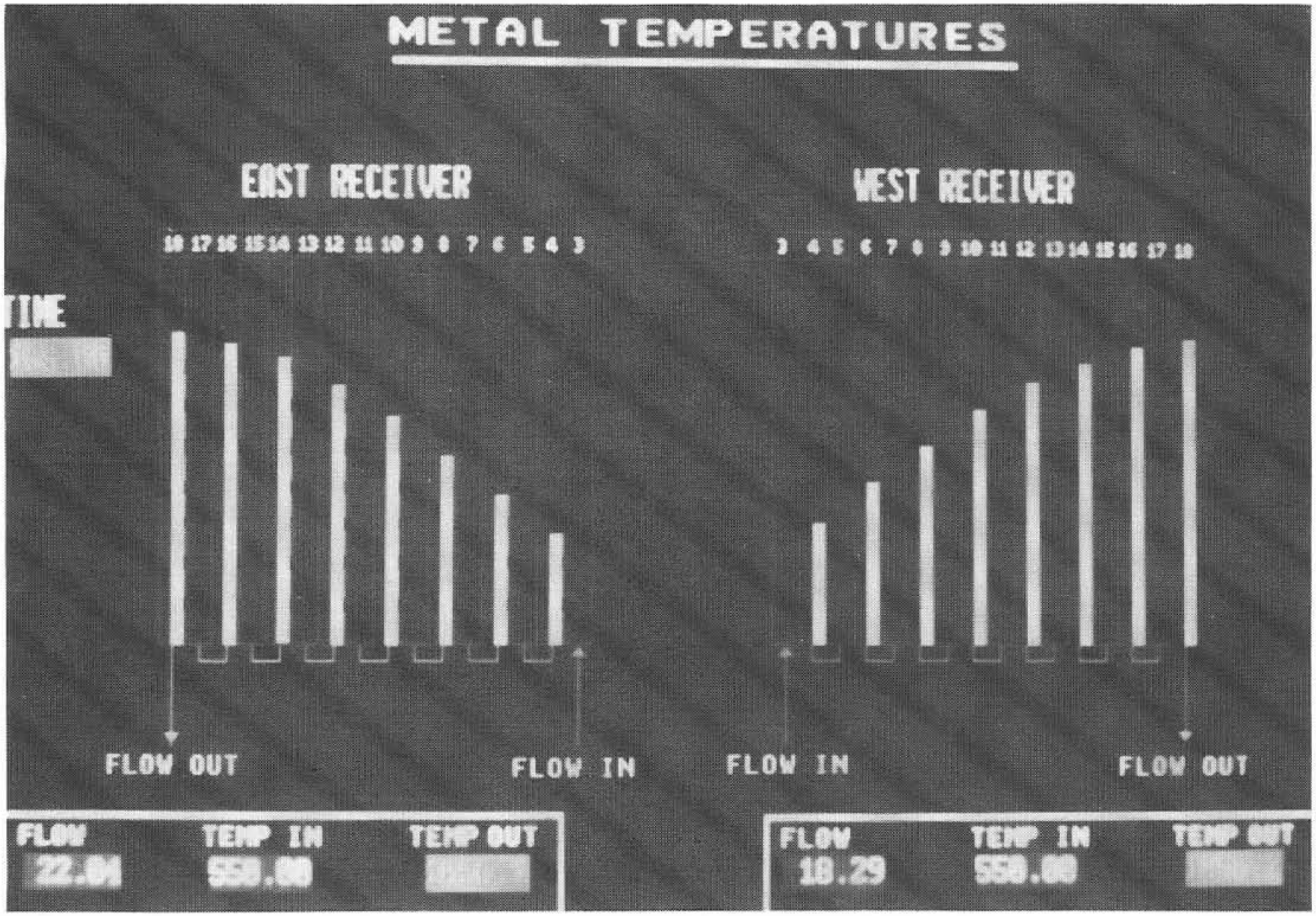

Figure 1-6 Receiver Metal Temperatures

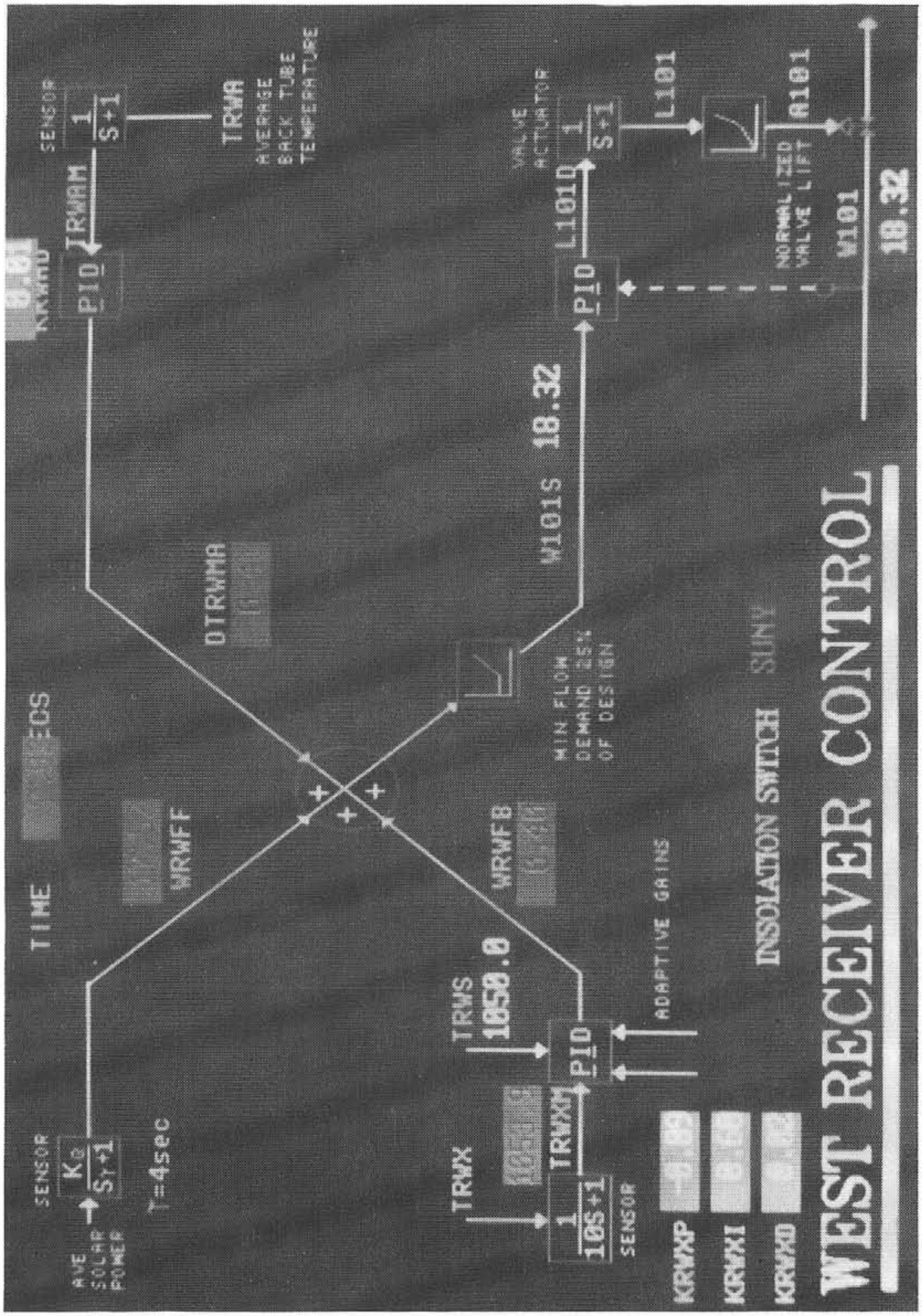

Figure 1-7 Schematic of West Receiver Control

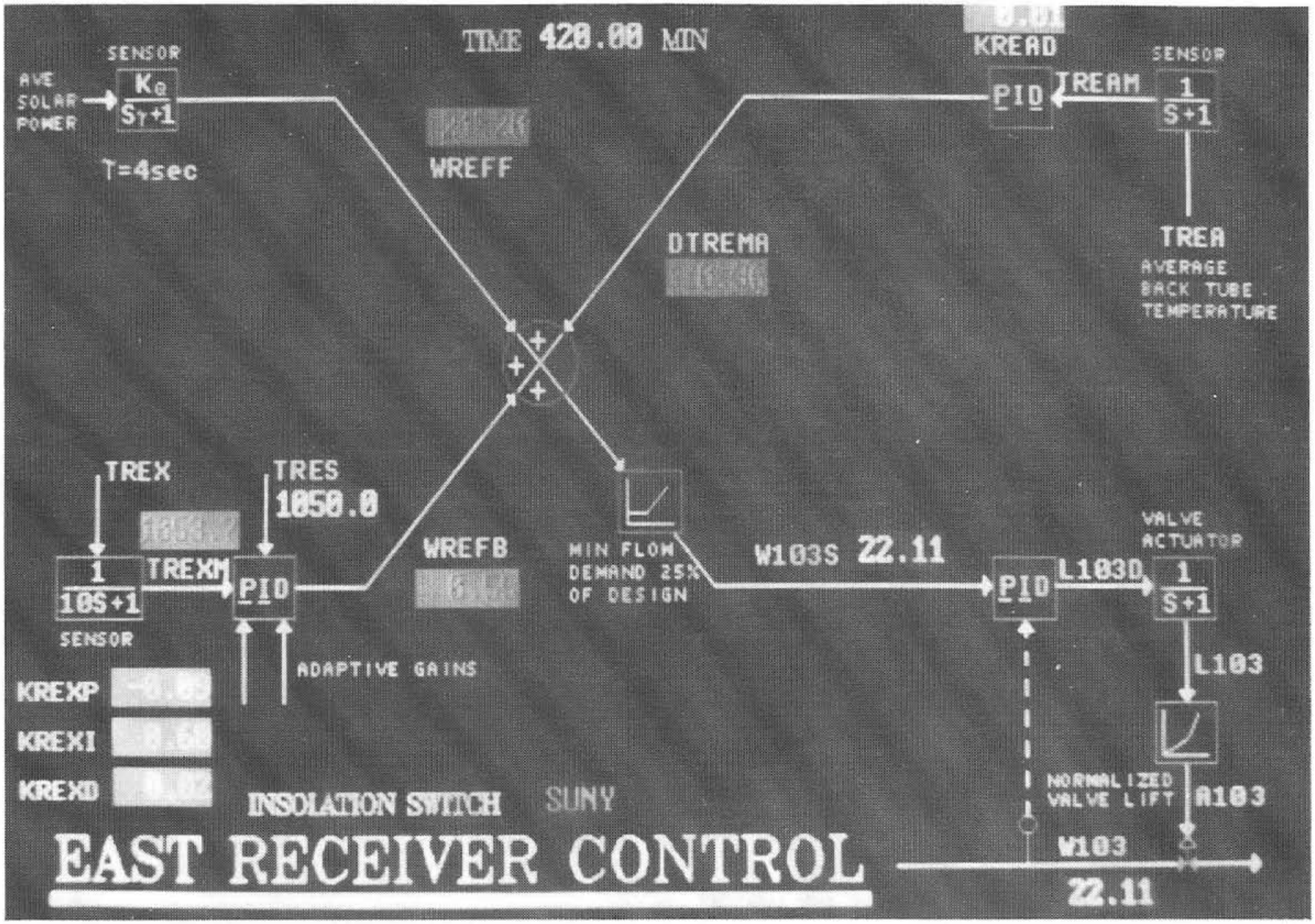

Figure 1-8 Schematic of East Receiver Control

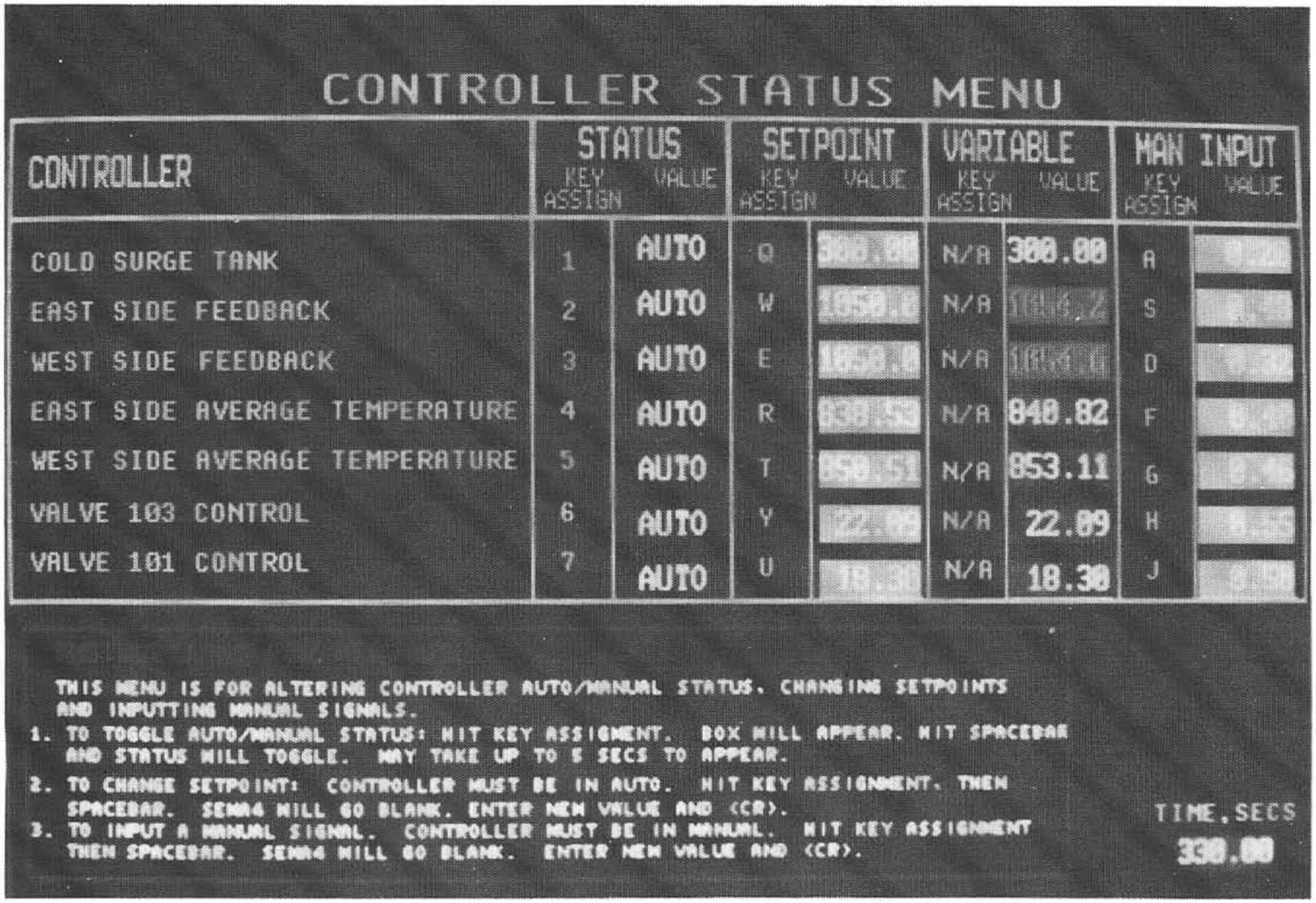

CONTROLLER STATUS MENU

CONTROLLER	STATUS		SETPOINT		VARIABLE		MAN INPUT	
	KEY ASSIGN	VALUE	KEY ASSIGN	VALUE	KEY ASSIGN	VALUE	KEY ASSIGN	VALUE
COLD SURGE TANK	1	AUTO	Q	300.00	N/A	300.00	A	[illegible]
EAST SIDE FEEDBACK	2	AUTO	W	1050.0	N/A	[illegible]	S	[illegible]
WEST SIDE FEEDBACK	3	AUTO	E	1050.0	N/A	[illegible]	D	[illegible]
EAST SIDE AVERAGE TEMPERATURE	4	AUTO	R	838.53	N/A	840.82	F	[illegible]
WEST SIDE AVERAGE TEMPERATURE	5	AUTO	T	850.51	N/A	853.11	G	[illegible]
VALVE 103 CONTROL	6	AUTO	Y	22.09	N/A	22.09	H	[illegible]
VALVE 101 CONTROL	7	AUTO	U	18.30	N/A	18.30	J	[illegible]

THIS MENU IS FOR ALTERING CONTROLLER AUTO/MANUAL STATUS. CHANGING SETPOINTS AND INPUTTING MANUAL SIGNALS.

1. TO TOGGLE AUTO/MANUAL STATUS: HIT KEY ASSIGMENT. BOX WILL APPEAR. HIT SPACEBAR AND STATUS WILL TOGGLE. MAY TAKE UP TO 5 SECS TO APPEAR.
2. TO CHANGE SETPOINT: CONTROLLER MUST BE IN AUTO. HIT KEY ASSIGNMENT. THEN SPACEBAR. SEMA4 WILL GO BLANK. ENTER NEW VALUE AND <CR>.
3. TO INPUT A MANUAL SIGNAL. CONTROLLER MUST BE IN MANUAL. HIT KEY ASSIGNMENT THEN SPACEBAR. SEMA4 WILL GO BLANK. ENTER NEW VALUE AND <CR>.

TIME, SECS
330.00

Figure 1-9 Controller Status Menu

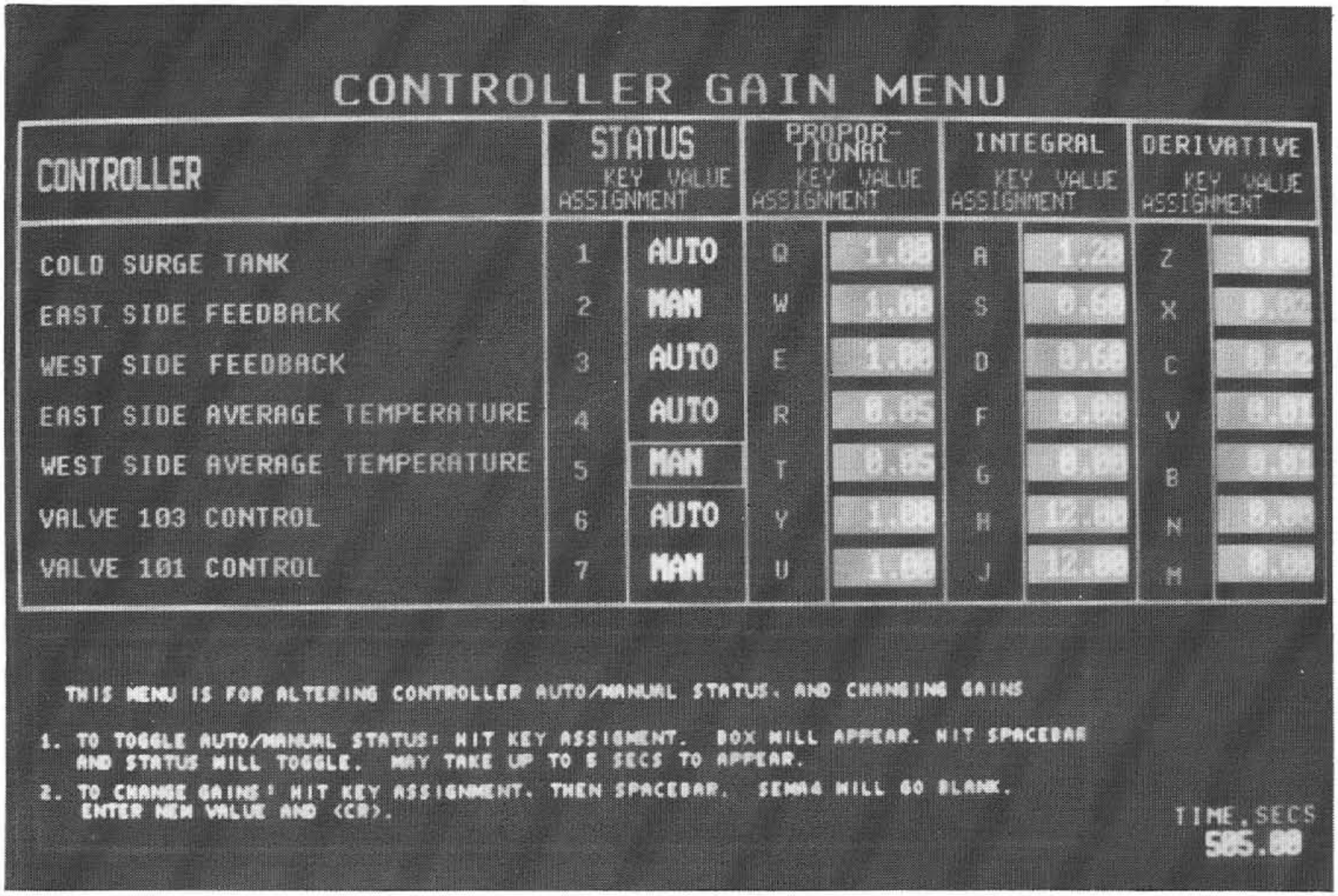

CONTROLLER GAIN MENU

CONTROLLER	STATUS KEY ASSIGNMENT	STATUS VALUE	PROPOR-TIONAL KEY ASSIGNMENT	PROPOR-TIONAL VALUE	INTEGRAL KEY ASSIGNMENT	INTEGRAL VALUE	DERIVATIVE KEY ASSIGNMENT	DERIVATIVE VALUE
COLD SURGE TANK	1	AUTO	Q	1.00	A	1.20	Z	0.00
EAST SIDE FEEDBACK	2	MAN	W	1.00	S	0.60	X	0.02
WEST SIDE FEEDBACK	3	AUTO	E	1.00	D	0.60	C	0.02
EAST SIDE AVERAGE TEMPERATURE	4	AUTO	R	0.05	F	0.00	V	0.01
WEST SIDE AVERAGE TEMPERATURE	5	MAN	T	0.05	G	0.00	B	0.01
VALVE 103 CONTROL	6	AUTO	Y	1.00	H	12.00	N	0.00
VALVE 101 CONTROL	7	MAN	U	1.00	J	12.00	M	0.00

THIS MENU IS FOR ALTERING CONTROLLER AUTO/MANUAL STATUS. AND CHANGING GAINS

1. TO TOGGLE AUTO/MANUAL STATUS: HIT KEY ASSIGMENT. BOX WILL APPEAR. HIT SPACEBAR AND STATUS WILL TOGGLE. MAY TAKE UP TO 5 SECS TO APPEAR.
2. TO CHANGE GAINS' HIT KEY ASSIGNMENT. THEN SPACEBAR. SEMA4 WILL GO BLANK. ENTER NEW VALUE AND <CR>.

TIME.SECS
505.00

Figure 1-10 Menu for adjusting Controller Gains

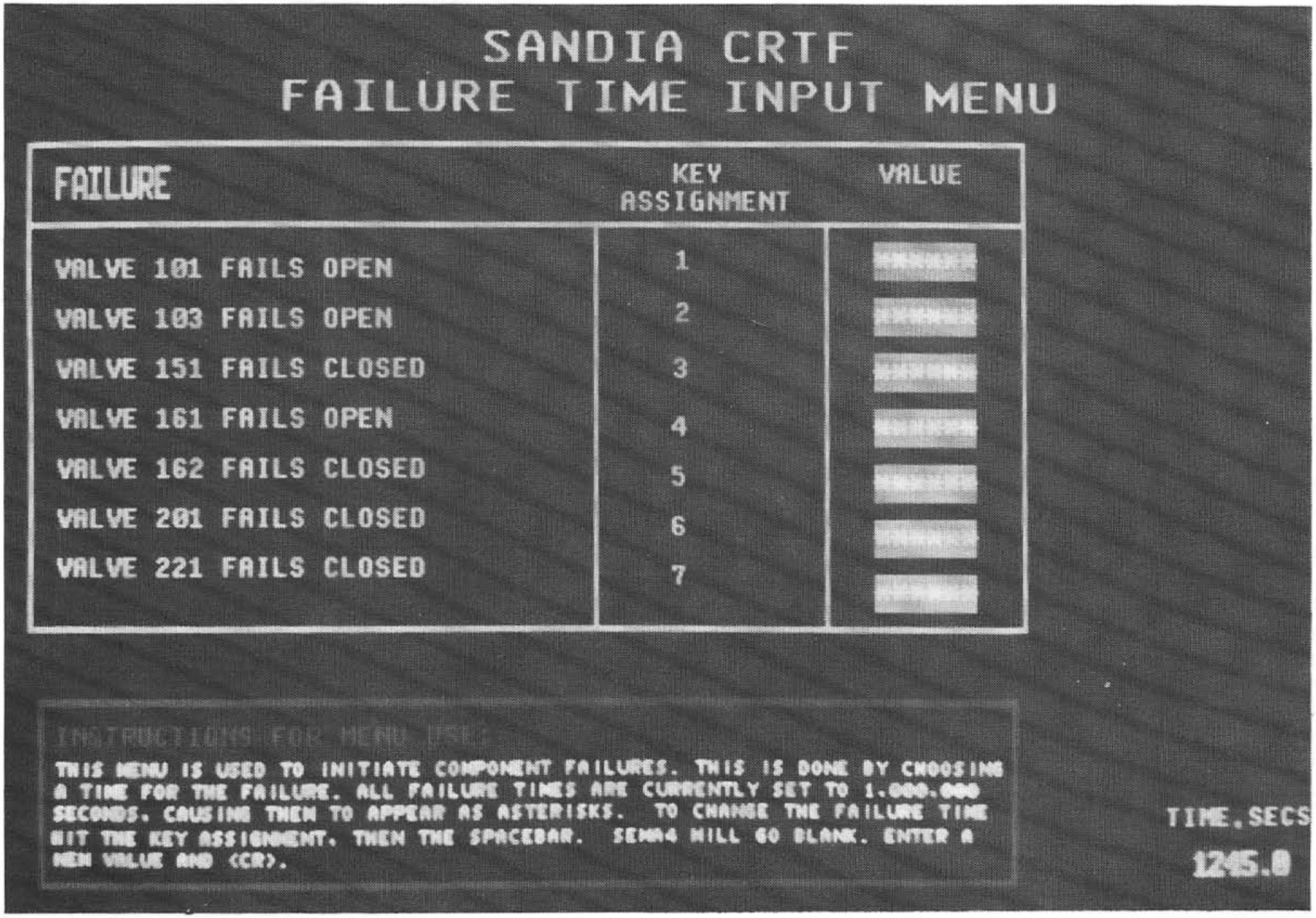

SANDIA CRTF
FAILURE TIME INPUT MENU

FAILURE	KEY ASSIGNMENT	VALUE
VALVE 101 FAILS OPEN	1	
VALVE 103 FAILS OPEN	2	
VALVE 151 FAILS CLOSED	3	
VALVE 161 FAILS OPEN	4	
VALVE 162 FAILS CLOSED	5	
VALVE 201 FAILS CLOSED	6	
VALVE 221 FAILS CLOSED	7	

INSTRUCTIONS FOR MENU USE:

THIS MENU IS USED TO INITIATE COMPONENT FAILURES. THIS IS DONE BY CHOOSING A TIME FOR THE FAILURE. ALL FAILURE TIMES ARE CURRENTLY SET TO 1,000,000 SECONDS, CAUSING THEM TO APPEAR AS ASTERISKS. TO CHANGE THE FAILURE TIME HIT THE KEY ASSIGNMENT, THEN THE SPACEBAR. SEMA4 WILL GO BLANK. ENTER A NEW VALUE AND <CR>.

Figure 1-11 Menu for Inputting Failure Times

Chapter 2

Model Development

In this chapter we discuss the development of the simulation model. We begin Section 2.1 with a brief description of the actual system hardware installed at the CRTF. In Section 2.2 we describe, in general terms, how a dynamic simulation model is developed and how the computer solves the system of equations. This is followed, in Section 2.3, by a discussion of the models constructed for the cavity-receiver system at the CRTF. Section 2.4 concludes with a demonstration of the simulator's capabilities.

2.1 Description of the Molten-Salt Receiver System

The 5-MW_t molten-salt receiver system was designed to demonstrate key features of the proposed commercial-scale Saguaro and Solar 100 systems [Arizona Public Service Company (1983) and Southern California Edison Company (1982)]. The proposed systems were rated at 190 MW_t and 312 MW_t, respectively and would convert solar energy to thermal energy using molten salt as the working medium. The 5 MW_t receiver, located at the top of the CRTF tower, receives concentrated solar energy from the collector field. Molten salt from the "cold" (550 °F) storage tank, located at ground level, is pumped up the tower piping and through the receiver, where it is heated to 1050 °F. The salt then flows through the downcomer into the hot salt storage tank. The test receiver was incorporated into the existing system at the CRTF. Heat collected in the salt is used to generate steam. This steam is condensed in a heat rejection system using a water/glycol mixture as the cooling fluid. This mixture is pumped to air-cooled heat exchangers, where the heat is rejected to the atmosphere.

A brief description of the 5-MW_t receiver and test facility is contained in the following subsections.

2.1.1 Receiver Subsystem

The receiver is located at the top of the CRTF tower, as shown in Figure 2-1. The concentrated insolation redirected from the heliostat field impinges on the absorber panels, through which molten-salt flow absorbs thermal energy. The receiver subsystem consists of the receiver absorber panels, cavity enclosure, cold surge tank, hot surge tank, instrumentation, and valves. The general configuration of the receiver is illustrated in the artist's concept shown in Figure 2-2.

The receiver employs a C-shaped cavity configuration, as shown in Figure 2-3. The back wall of the cavity is composed of heat-absorption panels, and the side walls, floor and ceiling are composed of insulation. At either side of the aperture are "wing panels," which collect the portion of the reflected solar beam that is too wide to enter the aperture. They also preheat the molten salt before it enters the main absorption panel. The frame above and below the aperture and to either side of the wing panels is constructed of passively cooled insulation board.

The heat-absorption panel is divided symmetrically into an east and a west zone. Each zone is composed of 18 passes connected in a series arrangement. Each pass consists of six tubes through which the total flow for the zone passes, either up or down. Passes 1 and 2 are in the wing panels, and the remaining panels are in the back wall, as shown in Figure 2-3. To facilitate manufacture and assembly, the absorption surface was arranged in eight individual panels consisting of a number of passes. These panels are designated 1 through 4 east and 1 through 4 west. Panel 1-east and panel 1-west are the wing panels; panels 2 through 4 (east and west) are back panels. Panels 2 and 3 (east and west) have six passes each, and panels 4-east and 4-west have four passes each. The surface of all panels exposed to solar radiation is painted with black Pyromark 2500 paint, which has demonstrated an absorptance of 97 percent for the solar spectrum.

The cold and hot surge tanks are located in the inlet and outlet lines of the receiver, respectively. Salt is piped up the tower into the cold surge tank. In the cold surge tank a salt level is maintained with a cover gas of pressurized air above it. The tank serves to buffer the receiver flow control from the salt pump supply by allowing level fluctuations to accommodate flow surges. In addition, the tank serves as a reservoir of salt to maintain flow for a short time in the event of a pump trip. Salt exiting the receiver panels is piped into the hot surge tank. This tank mixes the streams from the two receiver control zones and is vented to atmosphere to provide a free level from which to control flow in the downcomer. The tank also provides a space where salt can accumulate for a brief period in the event of a flow blockage in the downcomer.

Piping is provided in the receiver to connect the passes of the panels together (called "headers") and to provide lines for filling, draining, and venting the receiver.

Two types of valves are employed in the receiver: 1) the main control valves, and 2) the smaller drain and vent valves. The control valves are 1-inch offset-globe-type valves, allowing for draining of the salt. Drain/fill valves are located at the bottom of each pair of connected passes. Vent valves are located at alternate locations where passes connect at the top. Three-quarter inch valves were used for this purpose.

Salt is pumped to the receiver by two vertical cantilever pumps operating in series; a cold salt pump and a boost pump.

The receiver was instrumented extensively. Figure 2-4 shows locations of the instrumentation, which included thermocouples, heat flux gages, displacement gages, strain gages, level gages, pressure gages, and flow meters.

Supporting the receiver is an existing test facility, which was used on previous experiments and was modified specifically to support the receiver tests. It consists of a collector subsystem, a salt loop thermal storage subsystem, and support systems to generate steam and reject heat.

2.1.2 Collector Subsystem

The existing collector subsystem at the CRTF consists of 221 tracking heliostats (192 were used in the experiment) and their control system. Under optimum insolation and heliostat conditions, the heliostats can concentrate approximately 5.5 MW_t onto the receiver.

Each heliostat has 400 ft^2 of reflective surface, with a reflectivity of approximately 80 percent. Each structure has motor-driven azimuth and elevation gimbals, which allow it to track the sun during the day. The heliostats are operated remotely by the CRTF collector control system.

2.1.3 Thermal Storage Subsystem

The thermal storage subsystem supplies 550 °F salt to the receiver and 1050 °F salt for the steam generator. The subsystem includes the hot-salt and cold-salt storage tanks, propane-fired salt heater, two cold-salt pumps and one hot-salt pump, and cold- and hot-salt pumps. The storage system is sized to hold approximately 6 MW_t of thermal energy. The hot-salt tank employs internal insulation and an Incoloy liner. This insulates the tank shell from the hot salt and allows the use of carbon steel for the shell. The tank is also insulated from the outside. The cold-salt tank is made of carbon steel and is similar in design to the hot tank except that it does not require the internal insulation and liner because of its lower operating temperature. The salt pumps are of a vertical cantilever design. The impeller and casing are suspended below the liquid level in a sump; however, the bearings are located above the salt level.

2.1.4 Steam Generation and Feedwater Systems

The steam generator system is a forced circulation unit that uses an evaporator, superheater, and steam drum. During the experiment, the function of the system was to cool the salt leaving the hot storage tank to 550 °F and return the salt to the cold tank. We did not model this system and will therefore not describe it further.

2.1.5 Bailey Network 90 Control System

The Bailey Network 90 control system (NET-90) is a state-of-the-art process control system used in many different industrial applications. As applied to the molten-salt receiver and test facility, the NET-90 performs three major functions for process control of the thermal systems (receiver, thermal storage, and support):

1. Automatic process control (relative to set points),
2. Automatic plant trip when safety limits are exceeded, and
3. Operator control and monitoring.

The NET-90 is a distributed digital control system consisting of various operator and computer interface units, a plant communication loop, and process control units (PCUs). The PCUs contain the control algorithms modeled in the simulation and will therefore be described further.

There are three PCUs located in the field and each controls a different system: receiver, thermal storage, and heat rejection/feedwater. Each PCU is connected to the process equipment it controls for distributed digital control. A PCU consists of three main elements: power system, control and process I/O modules, and termination units. Consequently, a PCU is fully self-contained so that a failure outside the PCU does not cause a loss of process control. A PCU provides for instrument scanning (temperatures, flow rates, limit switches, etc.), data communication, control algorithm execution, and actuation or regulation of field equipment (pumps, valves, motors, etc.) in order to achieve control over the subsystem processes, as well as relay data back to the operator interface units via the plant communication loop.

2.2 Simulation Approach

The computer simulation of the CRTF was developed based on a set of model equations that describes the time-varying behavior of plant components such as the solar receiver, pumps, etc. The model provides for the computation of temperatures, pressures, and flows when there are disturbances such as cloud transients or component failures. The simulation was developed using the lumped-parameter-state-variable method. This section describes the application of this method using a mathematical presentation and an example.

The most detailed and accurate simulation of a solar facility would be based on spatially dependent mass, energy and momentum conservation relations written for the processes occurring in its system and components. These representations are characterized mathematically by partial differential equations (PDEs). Unfortunately, a facility simulation consisting of coded PDEs is costly to run and is typically much more detailed than necessary for adequate engineering analysis.

A simulation having a reasonable as well as adjustable level of detail is required for engineering analysis. It must be based on the application of engineering judgment (appreciation of intended model usage, significant physical effects, and required solution time) and formal manipulation of the spatially dependent conservation relations.

The spatially dependent conservation relationships can be approximated by considering spatial regions within a component where process properties, temperatures, pressures, etc., are homogenous. Such regions are called "lumps" or "control volumes." Mass, energy, and momentum conservation relations can be developed for the average values of process properties, temperatures, pressures in these "control volumes." These relations produce the lumped parameter state variable representations that are appropriate for producing a realistic system-wide plant simulation.

These representations are mathematically characterized by systems of first-order, nonlinear, ordinary differential equations (ODEs). The ODEs can be developed by volume-averaging the PDEs over "control volumes" that are defined by considering (1) regions of the facility with significant mass, energy, and momentum storage, (2) anticipated model usage, and (3) validity of assumptions required in the averaging process.

The volume averaging of one PDE produces one or several ODEs for each control volume considered. The number of control volumes (and hence the total number of ODEs) is determined as the model developer trades off the level of model detail required for the application with the desired solution time. Faster solution times may be obtained by reducing the detail in the model.

The resulting system of ODEs is characterized by the vector forms

$$\frac{dx}{dt} = f\ (x,\ u,\ p)\ , \qquad y = g\ (x,\ u,\ p)$$

where

x = a vector of state variables (usually analogs of mass, energy, or momentum such as density as the analog of mass storage in a gas, enthalpy as the analog of energy storage in a fluid, or temperature as the analog of energy storage in metal, and flow as the analog of momentum storage in a pipeline; other choices of state variables are made as required).

u = a vector of process control inputs such as valve position or gas flow rates.

p = a vector of parameters such as volumes, flow resistances, heat transfer coefficients, or chemical properties.

y = a vector of process outputs variables such as gas pressure, process flow rates, etc.

Values of the state vector (x) vary with time, as indicated by the differential equation. At any instant of time, this vector is the minimal set of data (when taken together with the input vector (u) that uniquely determines the future solutions of the system of equations). The state variables reflect the history or memory of the system, and as such represent a starting point for solution of the system of equations. When the input and parameter vectors are known, all other process variables are determined from the state variables.

To solve the system of ODEs for x(t) and y(t), one can use custom FORTRAN programs or simulation language programs. Common simulation language programs are CSMP, CSSL, ACSL, DSL and SYSL (E^2 Consulting 1987). These programs allow the user to code sets of FORTRAN-like expressions in a simulation language source code without regard for the correct solution order. The simulation language source file is processed to produce a sorted set of FORTRAN statements. After this operation is performed, the simulation language approach to code development is equivalent to the custom FORTRAN approach. The simulation language also provides several options for equation solution (numerical integration) and solution display (i.e., printouts and plots).

The following discussion demonstrates (1) equation development (2) FORTRAN programming and (3) equation solution via numerical integration for a gas storage tank. A schematic of the storage tank is depicted below. The flow into the tank is WIN. Its temperature is TIN. The flow out of the tank is WOUT, and its temperature is TOUT. The average temperature of gas stored in the tank is TSTOR, and its density is RSTOR. The tank was chosen as the site for a state variable equation because it has a large capacity defined by its volume, VSTOR. The pressure downstream of the tank is POUT, and flow to the downstream point is through an orifice characterized by the parameter KORF. The flowing gas is assumed to satisfy an ideal gas equation of state given by:

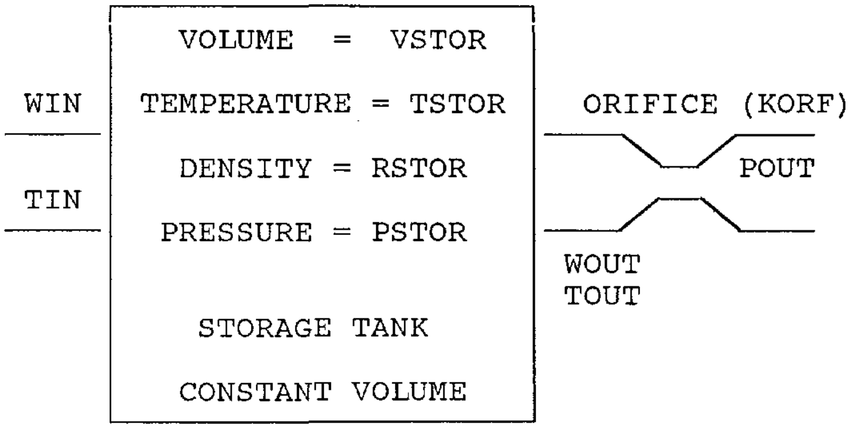

Schematic of a Gas Storage Tank

$$\text{PSTOR} = \text{RSTOR} * \text{R} * \text{TSTOR}$$

where R is the ideal gas constant. The tank is insulated so TIN = TSTOR = TOUT.

A model specification review has focused attention on the tank, since it represents a component of the facility where there is significant mass storage. To describe this storage, the model developer writes a differential mass conservation equation in the form:

$$\begin{bmatrix}\text{CHANGE IN}\\ \text{MASS OF GAS}\\ \text{STORED}\end{bmatrix} = \begin{bmatrix}\text{GAS FLOW}\\ \text{INTO VOLUME}\\ \end{bmatrix} - \begin{bmatrix}\text{GAS FLOW}\\ \text{OUT OF}\\ \text{VOLUME}\end{bmatrix}$$

In terms of the definitions this becomes

$$\frac{d}{dt}\left[\text{RSTOR} * \text{VSTOR}\right] = \text{WIN} - \text{WOUT} \quad .$$

Expanding the left-hand side and noting the volume of gas is constant, we have

$$\text{VSTOR} * \frac{d\ \text{RSTOR}}{dt} + \text{RSTOR} * \frac{d\ \text{VSTOR}}{dt} = \text{WIN} - \text{WOUT} \quad ,$$

so

$$\frac{d\ \text{RSTOR}}{dt} = \frac{\text{WIN} - \text{WOUT}}{\text{VSTOR}} \quad .$$

The flow into the tank is assumed to be independent of tank pressure. The flow out of the tank is given by the expression

$$\text{WOUT} = \text{KORF} * \sqrt{\text{RSTOR} * (\text{PSTOR} - \text{POUT})} \quad .$$

Suppose we wish to examine the behavior of tank pressure for a variation in inlet flow. To compute the transient characteristics of the pressure we need a FORTRAN or simulation program.

The flow chart required for solution of a general set of ordinary differential equations of the form

$$\frac{dx}{dt} = f\ (x,\ u)$$

is given in Figure 2-5. The output variables are assumed to be related to the states and inputs by the expression

$$y = g\ (x,\ u) \quad .$$

The first step in the program is to assign initial values to the state variables (x). The next step requires knowledge of the input variables (j) at time $t = t_n$. The input is considered constant over the small time interval (Dt) used in the integration algorithm. The outputs $y(t_n)$ are from equations that depend on the current state $x(t_n)$ and the current input $u(t_n)$. The rates of change for the state variables are computed from the same information. The state variables are integrated using the Euler or rectangular integration algorithm. Several other integration algorithms can be used in this step. The fourth-order Runga-Kutta algorithm is common. After integration, the time variable is incremented by the time step (delta t) used in the integration algorithm. The last block in the flow chart causes the program to jump back to the top and begin the sequence of calculations over again. By cycling through this loop, the solutions for x and y are obtained as u varies.

Figure 2-6 shows the flow chart for the storage tank equations. Note we have defined

u = WIN = INLET FLOW

x = RSTOR = TANK DENSITY

$$y = \begin{cases} \text{PSTOR} = \text{TANK PRESSURE} \\ \text{WOUT} = \text{OUTLET FLOW} \end{cases}$$

The FORTRAN program corresponding to this flow chart is given in Figure 2-7.

The FORTRAN program is set up to run until TIME is greater than or equal to FINTIM (the simulation termination time). The flow chart does not show this termination.

The Central Receiver Test Facility model in the simulator/analyzer is structured like the program in Table 2-1. It, however, contains several equations in the output, state rate, and integration segments. The equations in each segment are set up as the SYSL program sorts through the simulation language source statements. This type of model captures the essence of the dynamic behavior of the plant and can execute at greater than real time on a personal computer.

2.3 Description of Component Models for the Simulator

In this section, the equations used in developing the CRTF simulation are presented. Model equations are developed on a subroutine by subroutine basis.

A simulation schematic for the Sandia CRTF model is shown in Figure 2-8. The model is divided into the following subsystems:

- Receivers
- Thermal storage systems (tanks) and pumps
- Controllers and valves
- Plant trip system
- Solar flux processing routines

Two receivers operate at the CRTF, designated east and west. Both are 18-pass, 6-tube-per-pass units with molten salt circulating as coolant. Flow is serpentine. The first two passes of each receiver are separate from the main portion of the receiver and make up a wing panel. Flow from the wing panel is to the center (hottest) portion of the receiver. Design temperature rise across the receiver is 500 °F (from 550 to 1050 °F).

Subroutine RECVR models the dynamics of the heat absorption for the receiver. The model provides for 18 passes, 9 top headers and 8 bottom headers. The same subroutine is called with appropriate flux patterns for both east and west sides. Temperatures in the tubes, top, and bottom headers are all states and are available for inspection in the main routine. Thermal expansion is modeled as the salt traverses the receiver.

The thermal storage system consists of a series of tanks to hold salt before or after the receiver. All of the tanks except the cold surge tank are modeled with a generic tank model. Also included in the thermal storage system is a pump model for the cold sump and booster pumps.

An elaborate control algorithm has been developed to control the outlet salt temperature in the face of varying solar input. Briefly, it consists of three independent signals being summed to form a demanded flow signal, which is driving a valve lift. The simulation of the control system focuses around the digital proportional-integral-derivative (PID) controllers that are contained within a process control unit. This algorithm and the PID controllers were previously displayed in Figures 1-7 and 1-8.

The function of the plant's trip system is to protect the receiver in the event of equipment failures. The simulation model for this system continuously monitors flows, temperatures and pressures against pre-set limits. If an out-of-range condition is detected, an alarm buzzer is sounded, and the solar insolation is removed to simulate a heliostat defocusing.

Several solar processing routines have been developed to allow the use of insolation data by the simulator. Subroutines CLOUDE and CLOUDW read in flux data for each pass on the receiver.

2.3.1 Receiver Model

Figure 2-9 is a schematic of the receiver. Subroutine RECVR models the dynamics of heat absorption at the CRTF. The same subroutine, called with different arguments, models both the east and west side receivers. The model provides for 18 passes, 6 tubes per pass, 9 top headers, and 8 bottom headers. Flow in the receiver is serpentine, first through the wing panel (consisting of two passes) and then into the main body of the receiver.

At each time step, the calculation procedure is to find the convective heat transfer coefficient between the tube wall and salt by calling subroutine CONVEC (discussed later) with the current node temperature. After adjusting the heat transfer coefficient for flow rate, the heat transferred from the metal to salt is calculated by

$$Q_{mc} = \frac{T_{mi} - T_i}{R_{mc} + R_n} \quad , \tag{2-1}$$

where T_{mi} is the metal temperature, T_i is the salt temperature, R_{mc} is the thermal resistance of the salt/metal interface and R_m is the metal thermal resistance. The subscript I refers to the current control volume and is dependent on the number of control volumes per tube or header.

Next the metal's temperature derivative is computed from a metal energy balance

$$\rho_m \, C_{pm} \, V_m \, \frac{dT_{mi}}{dt} = EFF * Q_i - Q_{loss} - Q_{mc} \quad , \tag{2-2}$$

where ρ_m is the metal density, C_{pm} is the metal heat capacity, V_m is the current node volume, V_m is the current node volume, EFF is the absorptance of the receiver tubes, and Q_i is the total incident solar radiation on this node.

Thermal losses from the cavity receiver to the environment (Q_{loss} in the above equation) through the aperture were estimated with a finite-element-heat-transfer model. (Losses not passing through the aperture were neglected.) The geometry of the cavity was represented by 291 heat transfer elements. The mesh was developed with the PATRAN computer code (PDA Engineering 1984) and is depicted in Figure 2-10. The mesh and other parameters were input to the CAVITY code (Sayers) to obtain an estimate of the thermal losses. Given an incident flux distribution (see Figure 2-15), the CAVITY code calculates the radiative heat transfer between the various elements and predicts the temperature distribution throughout the cavity. Based on this temperature distribution, the code then estimates the radiative losses through the aperture to the environment. The code finally calculates convective losses using the Siebers and Kraabel (1984) heat transfer correlations. Estimates of various heat transfer areas are required by the correlations. These areas are defined in Siebers and are listed in Table 2-1 with other code input parameters. Given these inputs, the CAVITY code predicted the total thermal losses are approximately 379 Btu/s (400 KW); 227 Btu/s (240 KW) are radiative and 152 Btu/s (162 KW) are convective. These values are consistent with measurements taken during the experiment when solar flux was incident on the receiver (Chavez and Smith 1988).

During a cloud passage, flux is not incident upon the receiver and the cavity temperature will approach the salt inlet temperature (550 °F) within a few minutes. Since this temperature is significantly less than the "flux-on" temperature, thermal loss is less. We estimated radiative losses with the following simple calculation:

$$Q_{rad} = \sigma * A * \epsilon * (T^4_{cav} - T^4_{amb}), \tag{2-3}$$

where,

σ = Stefan-Boltzmann constant (0.17×10^{-8} Btu/hr-ft^2-°R^4)
A = aperture area of cavity (84 ft^2),
ϵ = emissivity of interior of cavity, assumed to be equal to the emissivity of the absorber tubes (0.948),
T_{cav} = cavity temperature (550 °F, 1010 °R), and
T_{amb} = ambient temperature (70 °F, 530 °R).

Radiative losses are estimated to be 36 Btu/sec (38 KW). We estimated convective losses with the Siebers and Kraabel correlation for natural convection,

$$h_{nc} = [0.81*(T_{cav}-T_{amb})^{0.426}] * (A1/A2) * (A3/A1)^{0.63},$$

and Newton's law of cooling,

$$Q_{nc} = h_{nc} * A_{cav} * (T_{cav} - T_{amb}), \tag{2-4}$$

where,

$A1, A2, A3$ = heat transfer areas listed in Table 2-1,
A_{cav} = area of inner surface of the cavity (379 ft^2),
T_{cav}, T_{amb} = defined above.

Convective losses are estimated to be 57.8 Btu/s (61 KW). Total losses during flux-off conditions are therefore approximately 94 Btu/s (99 KW).

The thermal losses estimated above were incorporated into the receiver simulation model. Whenever greater than 20 percent of full flux was incident upon the receiver, Q_{loss} was set to 379

Btu/s (400 KW). Twenty percent was chosen because the receiver control algorithm is designed to maintain the outlet salt temperature at rated conditions for flux levels greater than 20 percent. Since the average cavity temperature remains roughly the same, the average thermal losses should also be roughly the same. When flux was less than 20 percent (i.e., flux-off condition), Q_{loss} was set to 94 Btu/s (99 KW). This approach was taken in order to avoid the calculation of time-dependent temperature distributions within the cavity during cloud transients. Considering the uncertainties associated with the convective loss calculation, this simplistic approach appears justified.

Equation (2-2) was then modified to reflect the fact that only half of the metal is exposed to the sun. This implies the back sides of the tubes more closely track the salt's temperature. This is accounted for by reducing the metal's thermal inertia to half its calculated value and adding the other half to the thermal inertia of the salt. The modified energy balance is

$$\frac{dT_{mi}}{dt} = \frac{EFF * Q_i - Q_{mc} - Q_{loss}}{\rho_m\ C_{pm}\ V_m * 0.5} , \qquad (2\text{-}5)$$

or defining C_{tm} as $\rho_m\ C_{pm}\ V_m$ the final equation is

$$\frac{dT_{mi}}{dt} = \frac{EFF * Q_i - Q_{mc} - Q_{loss}}{0.5 * C_{tm}} . \qquad (2\text{-}6)$$

Next the salt temperature derivative is calculated from combined salt mass and energy balances. A salt mass balance yields

$$\frac{dM_{si}}{dt} = W_{i-1} - W_i , \qquad (2\text{-}7)$$

where M_{si} is the mass of salt in tube i, W_{i-1} is the flow into tube i, and W_i is the flow out of tube i. An energy balance yields

$$C_p * \frac{d(M_{si} * T_i)}{dt} = Q_{mci} + C_p * (W_{i-1} * T_{i-1} - W_i * T_i) , \qquad (2\text{-}8)$$

expanding

$$C_p * \left[\frac{T_i\ dM_{si}}{dt} + M_{si} \frac{dT_i}{dt} \right] = Q_{mci} + C_p * (W_{i-1} * T_{i-1} - W_i * T_i) . \qquad (2\text{-}9)$$

Multiplying T_i times the mass balance and subtracting yields

$$C_p * M_{si} * \frac{dT_i}{dt} = Q_{mci} + C_p * W_{i-1} * (T_{i-1} - T_i) \ , \qquad (2-10)$$

or finally

$$\frac{dT_i}{dt} = \frac{Q_{mci} + C_p * W_{i-1} * (T_{i-1} - T_i)}{C_p * \rho_i * V_i} \ . \qquad (2-11)$$

As per the above discussion, one half of the metal's thermal inertia is added to the salt's thermal inertia, which results in

$$\frac{dT_i}{dt} = \frac{Q_{mci} + C_p * W_{i-1} * (T_{i-1} - T_i)}{C_p * \rho_i * V_i + 0.5 * C_{pm}} \ . \qquad (2-12)$$

Next the outlet flow from this node is calculated. Utilizing the above mass balance,

$$\frac{d(M_{si})}{dt} = W_{i-1} - W_i, \qquad (2-13)$$

or

$$\frac{d(\rho_i V_i)}{dt} = W_{i-1} - W_i \ . \qquad (2-14)$$

The control volume at a node is constant, so expanding the left-hand side yields

$$V_i \frac{d\rho_i}{dt} = W_{i-1} - W_i \ , \qquad (2-15)$$

or rewriting the density term,

$$V_i \frac{d\rho}{dT} \frac{dT_i}{dt} = W_{i-1} - W_i \ . \qquad (2-16)$$

Finally,

$$W_i = W_{i-1} - V_i \frac{d\rho}{dT} \frac{dT_i}{dt} \ . \qquad (2-17)$$

The top and bottom headers' temperature equations are identical in form to the salt's temperature equations, except the headers are adiabatic, and conduction occurs from salt to header. Removing the Q_{mci} term from the salt's energy balance and adding the thermal capacity of the header yields

$$\frac{dT_i}{dt} = \frac{C_p * W_{i-1} * (T_{i-1} - T_i)}{C_p * \rho_i * V_i + C_{pm} * \rho_m * V_{mi}} , \qquad (2\text{-}18)$$

where ρ_m and C_{pm} and V_{mi} refer to the header's metal density, specific heat and volume, respectively.

All salt and metal temperatures are stored in vectors. The equations are integrated with the SYSL vector integration routine.

Subroutine CONVEC computes the heat transfer coefficient used to calculate the metal-to-salt heat transfer in the receiver. The salt is Partherm 430, a mixture of sodium and potassium nitrates. The calculational procedure is based on the Chilton-Colburn analogy for heat transfer for a liquid flowing in a tube.

Recalling the definition of the Nusselt number,

$$Nu = \frac{h*d}{K} , \qquad (2\text{-}19)$$

where Nu is the Nusselt number, h is the convective heat transfer coefficient, D is the tube diameter and K is the thermal conductivity. The Chilton-Colburn analogy states that

$$Nu = 0.023 * Re^{0.8} * Pr^{0.33} , \qquad (2\text{-}20)$$

where Re is the Reynolds number and Pr is the Prandtl number. Rearranging the above equation for the convective heat transfer coefficient yields

$$h = \frac{K}{D} (0.023 * Re^{0.8} * Pr^{0.33}) . \qquad (2\text{-}21)$$

The rest of this discussion centers on optimizing the above expression for maximum execution speed, because this routine is called many times each calculation pass. The Reynolds number, expressed in terms of mass flow rate is

$$Re = \frac{W}{\frac{\pi}{4} * D * \mu * 32.174} . \qquad (2\text{-}22)$$

Recalling the definition of the Prandtl number,

$$\mathrm{Pr} = \frac{\mu * C_p}{K * 32.174} , \qquad (2\text{-}23)$$

where C_p is the specific heat and K is the thermal conductivity of the salt.

For Partherm 430, the specific heat is 0.3654 BTU/lb*°F and constant. The tube diameter is input to this routine. Thermal conductivity and viscosity are known as functions of temperature. When all constants are substituted and evaluated, the result is

$$h = 1.8374 * 10^{-6} * D^{-1.8} * \mu^{-.147} * T^{.2184} . \qquad (2\text{-}24)$$

This coefficient is then passed back to subroutine RECVR and utilized in the heat transfer calculations inside the receiver tube passes.

2.3.2 Thermal Storage Tanks

There are several tanks at the CRTF. They are listed below with the system in which they are located and a simulation designator:

Tank Name	System	Designator
Hot Surge Tank	Receiver	HS
Cold Surge Tank	Receiver	CS
Sump for the Hot Pump	Thermal Storage	HM
Sumps for the Cold and Boost Pumps	Thermal Storage	CM
Hot Storage Tank	Thermal Storage	HT
Cold Storage Tank	Thermal Storage	CT

The flow path through the various tanks can be seen in the overall modeling schematic, shown in Figure 2-8.

All of the tanks with the exception of the cold surge tank are modeled with a generic tank model. A schematic of the generic tank is shown in Figure 2-11.

The model begins with a check to ensure the tank has not flooded or run dry. If the tank levels are within tolerance, the tank level and temperature derivatives are computed from salt mass and energy balances, respectively. In the following discussion, the subscript i refers to any one of the tanks listed above. The i can be replaced with the column labeled "designator" for exact nomenclature.

The level derivative is computed from a mass balance.

$$\frac{dM_i}{dt} = W_i - W_x \qquad\qquad \frac{d(\rho_i\ A_i\ l_i)}{dt} = W_i - W_x\ , \qquad (2\text{-}25)$$

where ρ_i is the density of salt in the tank, A_i is the tank cross-sectional area, and l_i is the salt level in the tank.

Expanding the left-hand side of Equation (2-25),

$$A_i\left(\rho_i\ \frac{dl_i}{dt} + l_i\ \frac{d\rho_i}{dt}\right) = W_i - W_x, \qquad (2\text{-}26)$$

or rearranging for the level derivative,

$$\frac{dl_i}{dt} = \frac{W_i - W_x}{A_i\ \rho_i} - \frac{l_i}{\rho_i}\ \frac{d\rho_i}{dT}\ \frac{dT_i}{dt}\ . \qquad (2\text{-}27)$$

Next, the temperature derivative is computed from a salt energy balance.

$$C_p\ \frac{d(M_i\ T_i)}{dt} = C_p\,(W_i\ T_{in} - W_x\ T_x)\ , \qquad (2\text{-}28)$$

where M_i is the salt mass in the tank, W_i is the flow into the tank, T_{in} is the temperature inlet to the tank, and T_x is the temperature exiting the tank. The tank is assumed to be well mixed so the exit temperature is equal to the bulk tank temperature. Expanding the left-hand side of the equation and substitution of the Equation (2-25) for the dM_i/dt term results in

$$\frac{dT_i}{dt} = \frac{W_i\ (T_{in} - T_i)}{M_i}\ . \qquad (2\text{-}29)$$

Cold Surge Tank

The cold surge tank is modeled as a cylinder 2.5 ft in diameter by 9 ft high with a level set point typically 75 to 80 inches. The cold surge tank is a pressurizer designed to provide flow to the receiver for at least 90 seconds in the event of loss of pump flow to avoid damage to the receiver. Energy losses to atmosphere are assumed to be negligible. The cold surge tank model assumes that salt is incompressible and the air is an ideal gas. Air heat capacity is assumed to be negligible, and air temperature is assumed instantaneously, to be in equilibrium with the salt.

The model begins with a check to ensure the tank has not dried out. Assuming the level is satisfactory, the salt temperature derivative is calculated from a combination of salt mass and energy balances. A mass balance yields

$$\frac{dM_{cs}}{dt} = W_{csi} - W_{csx} , \tag{2-30}$$

where M_{cs} is the mass of salt in the cold surge tank, W_{csi} is the salt flow rate into the cold surge tank, and W_{csx} is the salt flow rate out of the cold surge tank. A salt energy balance yields

$$C_p \frac{d}{dt} (M_{cs} * T_{cs}) = C_p * (W_{csi} * T_{csi} - W_{csx} * T_{cs}) , \tag{2-31}$$

where T_{cs} is the temperature of the cold surge tank salt, C_p is the salt's specific heat, T_{csi} is the salt temperature inlet to the cold surge tank, W_{csx} is the exit salt's flow rate, and T_{cs} is the cold surge tank salt's temperature. Expanding the left-hand side of the above equation yields

$$M_{cs} * \frac{dT_{cs}}{dt} + T_{cs} * \frac{dM_{cs}}{dt} = W_{csi} \, T_{csi} - W_{csx} \, T_{cs} . \tag{2-32}$$

Multiplying the mass balance by T_{cs} and subtracting yields

$$M_{cs} \frac{dT_{cs}}{dt} = W_{csi} * (T_{csi} - T_{cs}) . \tag{2-33}$$

Finally,

$$\frac{dT_{cs}}{dt} = \frac{W_{csi} * (T_{csi} - T_{cs})}{\rho_{cs} V_{cs}} . \tag{2-34}$$

Next the level derivative is computed. Rewriting the salt mass balance,

$$\frac{d(\rho_{cs} * V_{cs})}{dt} = W_{csi} - W_{csx} . \tag{2-35}$$

Expanding the left-hand side and rearranging terms yields

$$\frac{dV_{cs}}{dt} = \frac{* \; W_{csi} - W_{csx} - V_{cs} \; (d\rho_{cs}/dt)}{\rho_{cs}} \; . \qquad (2\text{-}36)$$

Substituting L_{cs} A_{cs} = V_{cs} and rewriting the density derivative yields

$$\frac{dL_{cs}}{dt} = \frac{W_{csi} - W_{csx} - L_{cs}A_{cs}(d\rho_{cs}/dT_{cs})*(dT_{cs}/dt)}{A_{cs}\rho_{cs}} \; . \qquad (2\text{-}37)$$

Finally, a pressure derivative is computed by an air mass balance,

$$\frac{dM_{csg}}{dt} = G_{csi} - G_{csx} \; , \qquad (2\text{-}38)$$

where M_{csg} is the mass of air in the surge tank, G_{csi} is the inlet air flow rate and G_{csx} is the exit air flow rate. Substituting for M_{csg} and noting K_{csv} - V_{cs} is the air volume in the above equation yields

$$\frac{d[\rho_{csg} * (K_{csv} - V_{cs})]}{dt} = G_{csi} - G_{csx} \; , \qquad (2\text{-}39)$$

where ρ_{csg} is the density of air and K_{csv} is the total surge tank volume. From the ideal gas law,

$$\rho_{csg} = \frac{P_{cs}}{\text{KUNGR} * (T_{csg} + 460)} \; , \qquad (2\text{-}40)$$

where KUNGR is the ideal gas constant, and the 460 converts the temperature to absolute. Assuming temperature varies slowly in comparison to pressure and substituting into the mass balance,

$$\frac{d}{dt} \quad \frac{P_{cs} * (K_{csv} - V_{cs})}{\text{KUNGR} * (T_{cs} + 460)} = G_{csi} - G_{csx} \; . \qquad (2\text{-}41)$$

Rearranging for $\frac{dP_{cs}}{dt}$ yields

$$\frac{dP_{cs}}{dt} = \frac{[G_{csi} - G_{csx}] * KUNGR * (T_{cs} + 460) + P_{cs} * \frac{dV_{cs}}{dt}}{K_{csv} - V_{cs}} . \quad (2\text{-}42)$$

2.3.3 Cold Pumps

Subroutine PUMP models the cold sump and surge pumps as a single lumped pump with equivalent total head. Pump head is expressed as a quadratic in pump flow.

The subroutine begins with a check to see if valve 151 is open. If not, the pump flow is set to zero, and a return executed to avoid the numerical problems associated with deadheading a pump. Assuming the pump is operational, the flow through the pump is calculated.

Total head is the sum of static and frictional losses. Static head is given by the drop that is approximately 213 feet from the pump outlet, plus the level in the cold surge tank. Friction losses are flow squared losses associated with the piping and with valve 151.

The pump curve is represented by

$$P_x - P_i = J_o + J_1 * W + J_2 * W^2 , \quad (2\text{-}43)$$

where P_x is the pump exit pressure, P_i is the pump suction pressure, and W is the salt mass flow rate. J_o, J_1, and J_2 are found by a least squares fit of pump head versus flow of pump manufacturer data.

$$\text{Total head} = \left(\frac{213 + l_{cst}}{12}\right) \frac{\rho_s}{144} + \frac{W^2}{(K_v * A_v)^2 * \rho_i} + \frac{K_f * W^2}{\rho_i} , \quad (2\text{-}44)$$

where l_{cst} is the cold surge tank level in inches, ρ_s is the salt density, W is the salt flow rate, K_v is the valve 151 pressure loss coefficient, A_v is the normalized (0 to 1) valve area, and K_f is the piping friction loss coefficient. The first term in the above equation represents static head, the second is the valve pressure drop, and the last term represents piping friction losses.

The equation above may be rewritten

$$0 = A * W^2 + B * W + C \ , \qquad (2\text{-}45)$$

a standard quadratic where

$$A = J_2 - \frac{1}{(K_v * A_v)^2 * \rho_i} - \frac{K_f}{\rho_i}$$

$$B = J_1$$

$$C = J_o - \frac{213 - l_{est}}{12} * \frac{\rho_s}{144} - (P_{cst} - P_i) \ .$$

The solution to the above is standard,

$$W = - B + \frac{\sqrt{B^2 - 4 * A * C}}{2 * A} \ ,$$

where the negative root has been discarded for physical reasons.

2.3.4 Control System

An elaborate control algorithm has been developed to control the outlet salt temperature on the east and west sides of the receiver in the face of varying solar input. The algorithm was developed by Mr. Gene Riley of McDonnel Douglas Corporation (Chavez and Smith 1988). Three independent control signals are used on each side. They are

1. a feedback signal from the salt-exit temperature,
2. a feedback signal from the average-back-tube temperature,
3. a feed forward signal from the average solar flux on the receiver.

These signals are summed to provide a total flow signal to the flow control valve.

Adaptive gains are utilized to modify overall and integral gains as a function of flow rates in the salt-exit temperature controller. The exit temperature set point is also ramped between 850 °F and 1050 °F during cloud transients. The set point is the measured temperature +50 °F within predetermined rate limits. The algorithm for the east side is displayed in Figure 2-12. The algorithm for the west side is similar.

Function PIDN90 simulates a Bailey Network 90 Digital Proportional-Integral-Derivative (PID) controller used at the CRTF. Seven such controllers are used in the CRTF simulation; three for east-side exit temperature control, three for west temperature control and one for cold surge tank pressure control. (The PIDs for the east side can be seen in Figure 2-12). The digital PID calculates updated control signals at 0.25-second intervals. This model was provided by McDonnell Douglas, but the company was unable to obtain the actual Bailey programming. Tests against the actual controller show similar responses to step and ramp inputs but differing responses to a sinusoidal input. This may cause problems when comparing simulation results with actual data.

The function begins by setting up vectors that will hold data based on the sequential identification number assigned to the controller. Next is a check to see if it is time to update. If not, an immediate return is executed.

Updating the controller requires the following algorithm. If AM = 0 (AM is the auto/manual switch), then the controller is in manual and the output of the controller is set according to

OUT(N) = AMAX1 [LO, AMIN1 (MSET, Hi)] ,   (2-46)

where OUT(N) is the controller output for controller number N, LO is the low limit on the controller output, MSCT is the manual signal demanded, and Hi is the high limit on the controller output.

The AMAX1 and AMIN1 are intrinsic FORTRAN 77 functions returning the maximum and minimum of the arguments input, respectively. This assures the controller output is bounded.

If the controller is not in manual, two choices are possible: the controller is transitioning from manual to automatic or the controller is in automatic. If the controller is transitioning to automatic, the past value of its auto/manual switch will be 0 (manual). The test is

IF[AM1(N) .EQ. 0] IC(N) = 1 ,   (2-47)

where AM1(N) is the value of the controller auto/manual switch during the last controller update. If there is indeed a transition, the controllers are initialized for automatic operation, which includes setting IC(N) = 0 to avoid constant reinitializing.

Next the derivative signals are formulated. A check for saturation of the controller is performed, and an internal flag is set if it has occurred.

The proportional, integral and derivative terms are then formed and summed, and the present values are set equal to the past values for the next update pass initialization. The algorithm for the velocity form PID is represented below:

$$\frac{d\ OUT(N)}{dt} = K_{sc} * [Ki * E + K_p * dE/dt + K_d * d(dE/dt)/dt]$$

$$OUT(N)_i = OUT(N)_{i-1} + \frac{d\ OUT(N)}{dt} * DT_{up} \quad . \qquad (2\text{-}48)$$

In these equations the proportional, integral, derivative, and overall gains are K_p, K_i, K_d, and K_{sc}, respectively. The error signal is designated E, and DT_{up} is the update interval (0.25 seconds). As stated previously, adaptive gains are utilized to modify the overall and integral gains as a function of flow rates in the exit-temperature-feedback controller. Adaptive gains were utilized to help compensate for the non-linearites in the process dynamics (i.e., the process time constants are longer at low power and low flow conditions than they are at high power and high flow). The gain functions are displayed in Figure 2-13.

2.3.5 Plant Trip System

The simulated plant trip system for the CRTF simulator/analyzer system continuously monitors flows, temperatures and pressures against pre-set limits. Its function is to protect the receiver in the event of equipment failures. If an out-of-range condition is detected, an alarm buzzer is sounded, and the solar insolation is removed to simulate a heliostat defocusing.

The table below lists the conditions being monitored.

PROCESS VARIABLE	CONDITION	DURATION
WEST EXIT TEMPERATURE	>1080 °F	N/A
EAST EXIT TEMPERATURE	>1080 °F	N/A
WEST PASS 17 TEMPERATURE	>1070 °F	30 SECS
EAST PASS 17 TEMPERATURE	>1070 °F	30 SECS
WEST PASS 16 TEMPERATURE	>1050 °F	30 SECS
EAST PASS 16 TEMPERATURE	>1050 °F	30 SECS
WEST PASS 15 TEMPERATURE	>1030 °F	30 SECS
EAST PASS 15 TEMPERATURE	>1030 °F	30 SECS
WEST PASS 14 TEMPERATURE	>1010 °F	30 SECS
EAST PASS 14 TEMPERATURE	>1010 °F	30 SECS
EAST SALT FLOW	<8 KLB/HR	10 SECS
WEST SALT FLOW	<8 KLB/HR	10 SECS
SALT BOOST PUMP PRESSURE	<400 PSI	N/A
COLD SUMP LEVEL	<12 IN.	N/A

2.3.6 Solar Flux Processing

The solar fluxes employed in the simulator are shown in Figure 2-14. Each figure presents the average flux (KW/m^2) per tube as a function of position on the receiver while a flat-edged cloud progresses across the heliostat field in equally spaced increments. Curves were developed for three separate times on day #300: 8 a.m., noon, and 4 p.m. These average curves were developed from two-dimensional flux maps produced by the DELSOL computer code (Kistler 1986). The DELSOL flux maps for the noon case are presented in Figure 2-15. The map in the upper left corner is the flux on the receiver when the westernmost heliostats are exposed to the sun. As the cloud clears the field from west to east, the flux progressively increases until full sun conditions are achieved. Full sun is displayed in the lower right corner. (The centerline of the receiver is located at 180 degrees. The east side ranges form 120 to 180 degrees and west side from 180 to 240 degrees.)

Subroutines CLOUDE.FOR and CLOUDW.FOR read and store the transient flux data presented above. Data are read from disk files and stored in a two-dimensional array. This array is five rows by 18 columns. Each column corresponds to the flux incident on a pass through the receiver. The first row in the array represents flux at full-sun conditions, and the last row represents flux under full cloud cover.

We did not develop flux distributions for the wing panels. The temperature rise across a wing panel is approximately 20 °F. During a cloud transient, it is assumed the variation of flux in these two passes is proportional to that of pass 18, which is closest in physical proximity.

2.4 Demonstration of Simulator

We will demonstrate the simulator with a failure transient. Valve 101 is failed open at a simulation time of 120 seconds. This valve is used to control the flow to the western receiver and is depicted in Figure 2-8.

The simulation conditions for the failure were:

- the plant trip's system was fully active
- the failure was programmed for 120 seconds simulated time
- the flux pattern used was for day 300 at solar noon
- the control system was fully active
- the simulation was terminated at 1800 seconds simulated time

Figures 2-16 through 2-18 present the simulated results for the valve 101 failure. Process parameters for the receiver are presented in Figure 2-16, control system signals are presented in Figure 2-17, and tank parameters are depicted in Figure 2-18.

Referring to Figure 2-16, failure open of valve 101 has the consequence of increasing flow (W101) through this valve. Since flux stays constant, the west-side salt exit temperature (TRWXM) decreases. The east-side flow rates (W103) and temperatures (TREXM) are unaffected. The cold surge tank pressure (PCST) initially drops about 4 psi in response to the increased flow and is then restored to the 300 psi setpoint by the tank level controller. The east (PREX) and west (PRWX) receiver exit pressures are relatively unaffected.

Figure 2-17 shows the salt flow setpoints (W101S and W103S) and the three independent signals that sum to form these demanded flow rates. WRWFF is the feed-forward signal, DTRWMA is the average temperature signal, and WRWFB is the feedback signal for the west side. Nomenclature is similar for the east side. The behavior on the west side is predictable. When the valve becomes stuck open, all temperature control is impossible. The flow set point falls to minimum in an attempt to control the exit temperature. The average temperature controller also winds down, until eventually the error signal changes sign and then winds up, but has no effect on the total flow set point. The feedback signal winds down to its lower limit but also has no effect on the total demanded flow signal. The feedforward signal is unaffected, as the solar insolation is unchanged. The east-side signals are unaffected by the west, as shown in Figure 2-17.

The position signals for the various valves in the system are also shown in Figure 2-17. As can be seen, the east-side flow control valve (103) is unaffected, whereas the west-side valve (101) position is driven to fully open. Valve 151 is driven open to supply the additional flow for valve 101. Valves 161 and 201 both open in response to the additional flow being passed by valve 101. Valve 162 is closed because the salt temperature is above 750 °F. Valve 161 automatically adjusts to maintain control of the hot surge tank level.

The levels and temperatures of the various tanks are presented in Figure 2-18. The hot surge tank level (LHS) reacts quickly to the increased flow through valve 101 and increases rapidly at 120 seconds and then levels off. The rate of decrease of the hot storage tank (LHT) lessens at 120 seconds because the flow rate into the tank is higher as a result of opening valve 101. The hot sump level (LHM) is controlled and therefore changes little. The cold surge tank pressure is controlled at 300 psig, and this keeps the cold surge tank level (LCST) to within .3 inches of 75 inches at all times. The cold tank level (LCT) slows its rate of increase, since the difference between the flows into and out of the tank decreases as the result of opening valve 101. The cold sump level (LCM) is under level control and is relatively unaffected. The temperatures of the hot surge tank (THS), hot storage tank (THT), and hot sump (THM) decrease as a result of the decreasing receiver exit salt temperature. The temperatures of the cold surge tank (TCST) and cold storage tank (TCT) are unaffected by the failure of valve 101.

Table 2-1

Input Parameters for CAVITY Code Analysis

Heat Transfer Areas for Convective Loss Calculation	A1=379 ft^2 * A2=379 ft^2 * A3=258 ft^2 *
Absorber Emissivity	0.948
Adiabatic Surface Emissivity (Cavity Walls)	0.300
Tube Diameter	0.0625 ft
Tube Wall Thickness	0.0054 ft
Inlet Salt Temperature (Exit From Wing Panels)	572 °F
Outlet Salt Temperature	1050 °F

* - A1, A2, and A3 are defined in Siebers and Krabbel, 1984.

Figure 2-1 Aerial View of Central Receiver Test Facility

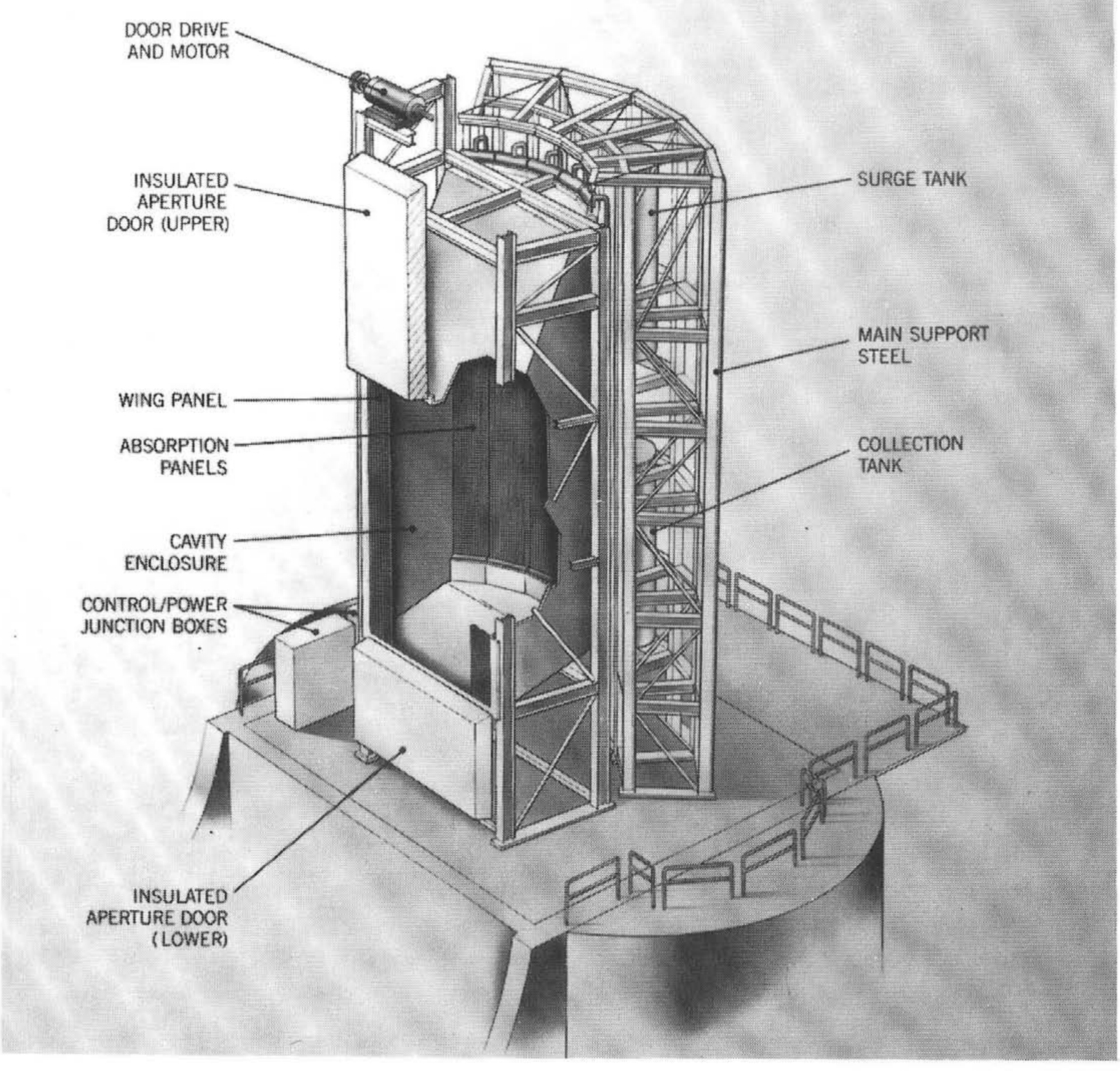

Figure 2-2 5 MW_t Molten Salt Cavity Receiver

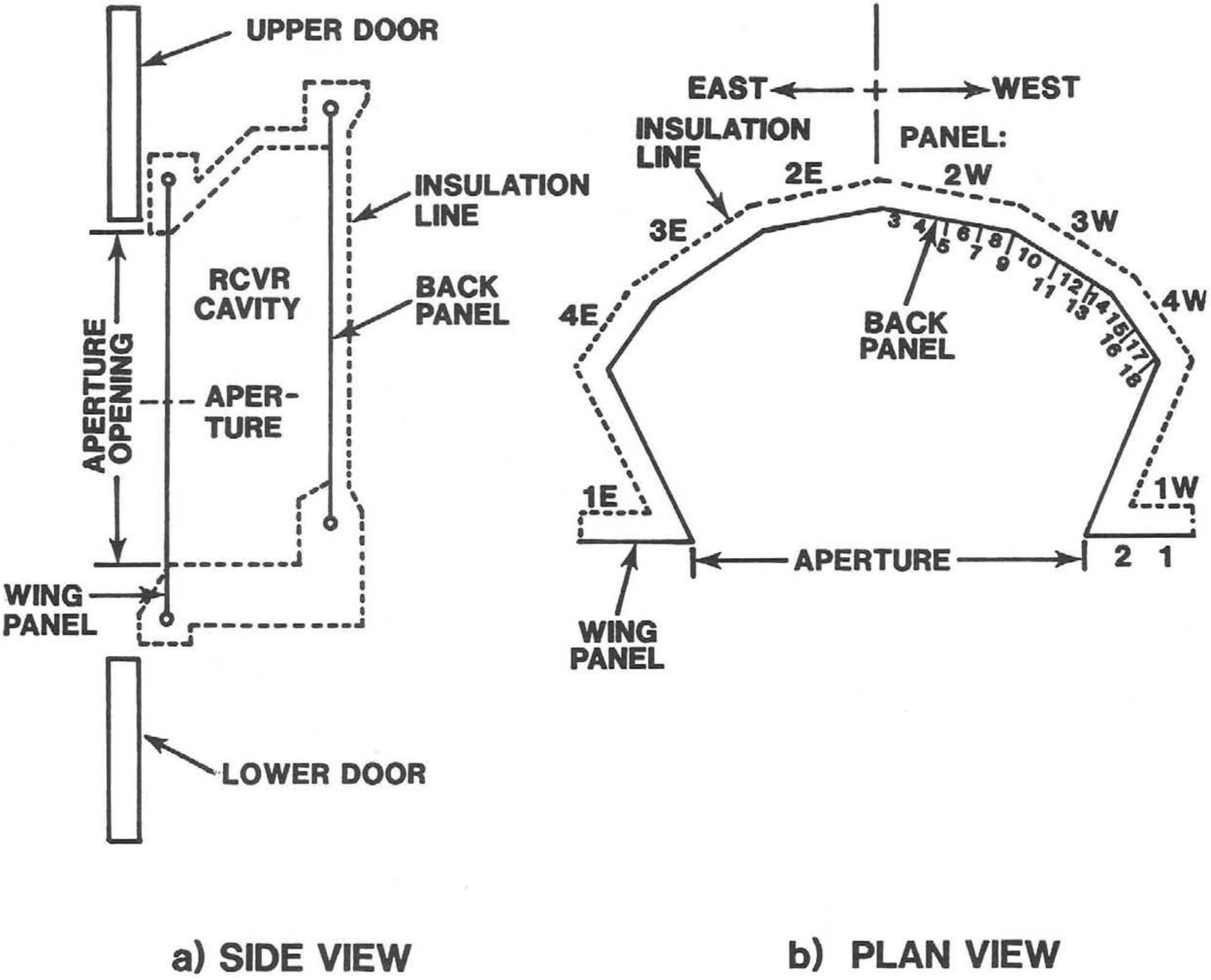

Figure 2-3 Receiver Layout

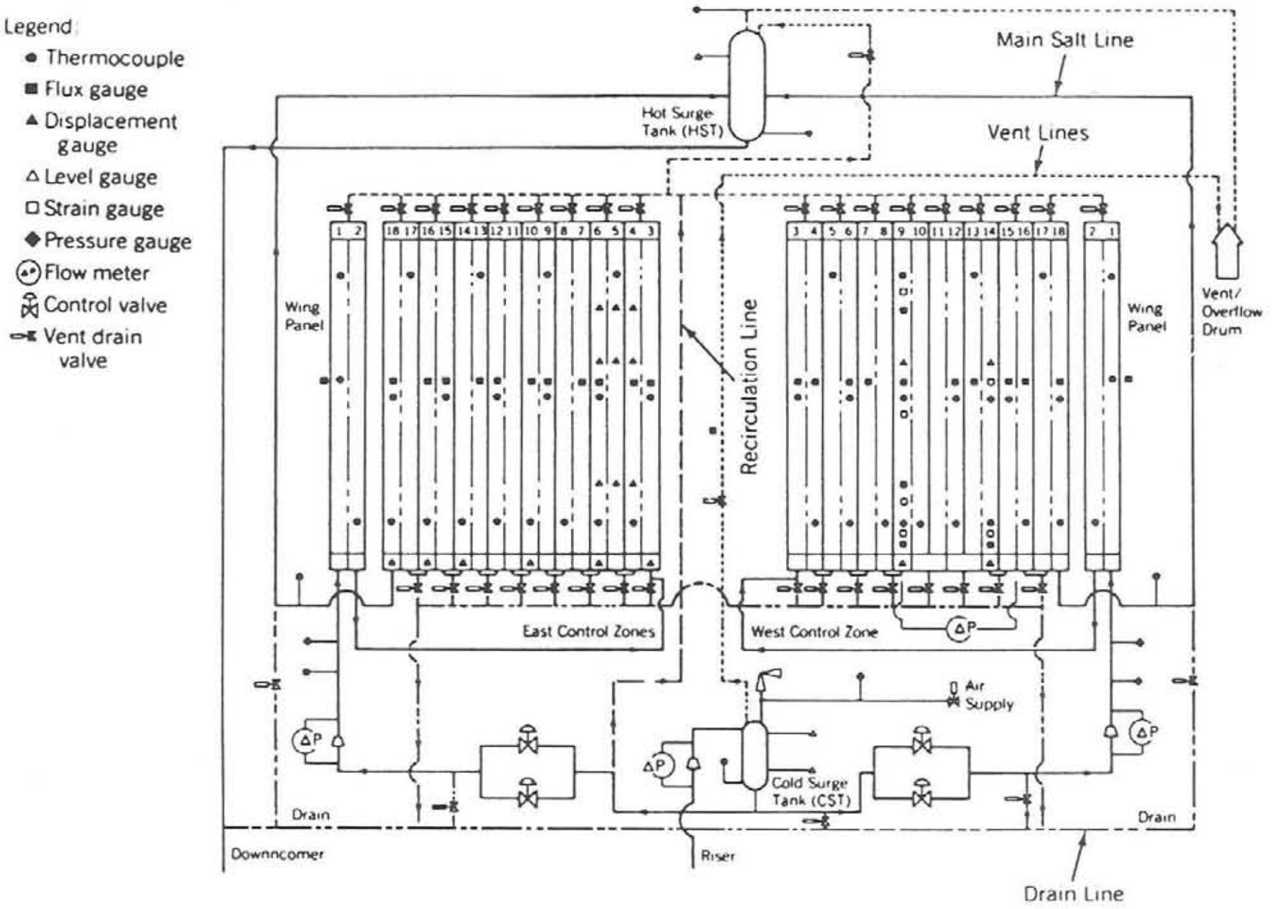

Figure 2-4 Receiver Instrumentation

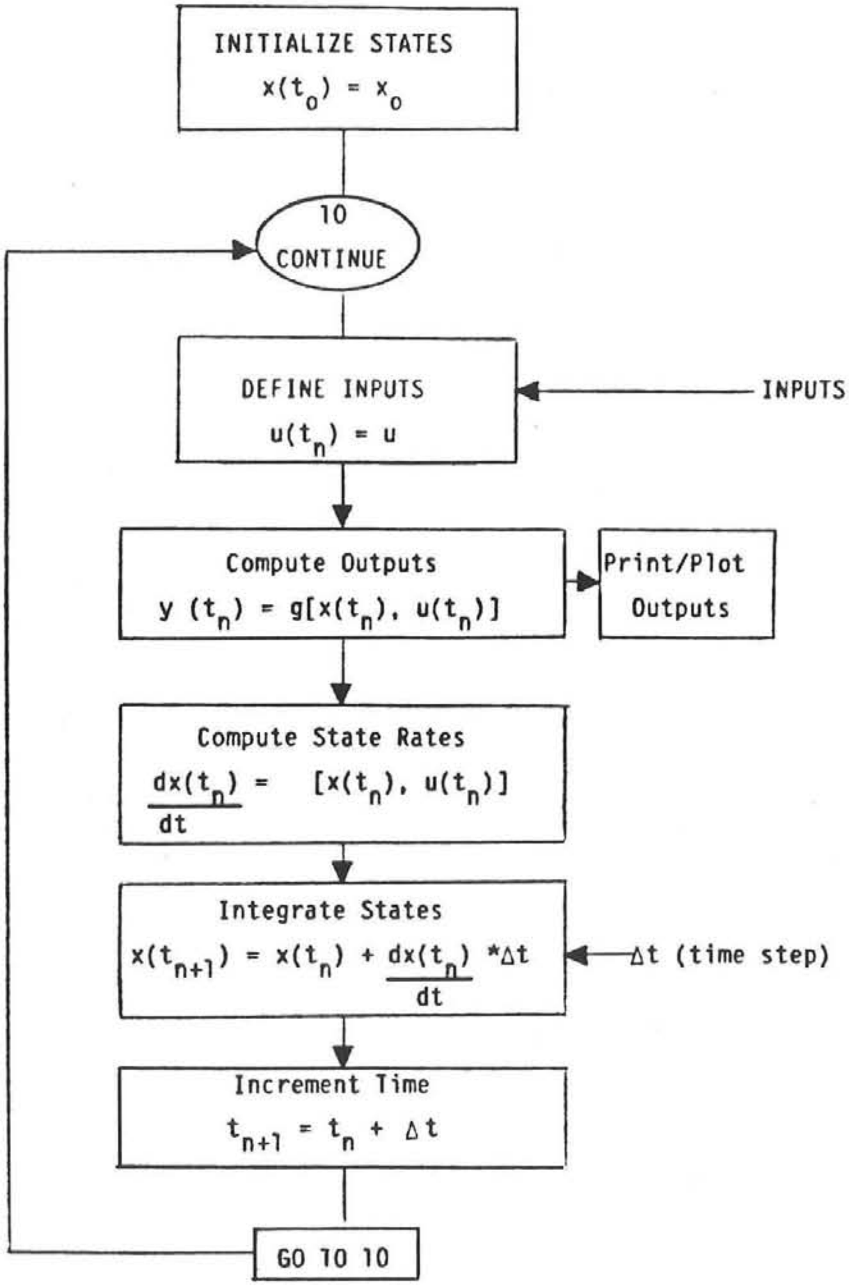

Figure 2-5 Flow Chart for a Program to Solve a Set of Ordinary Differential Equations

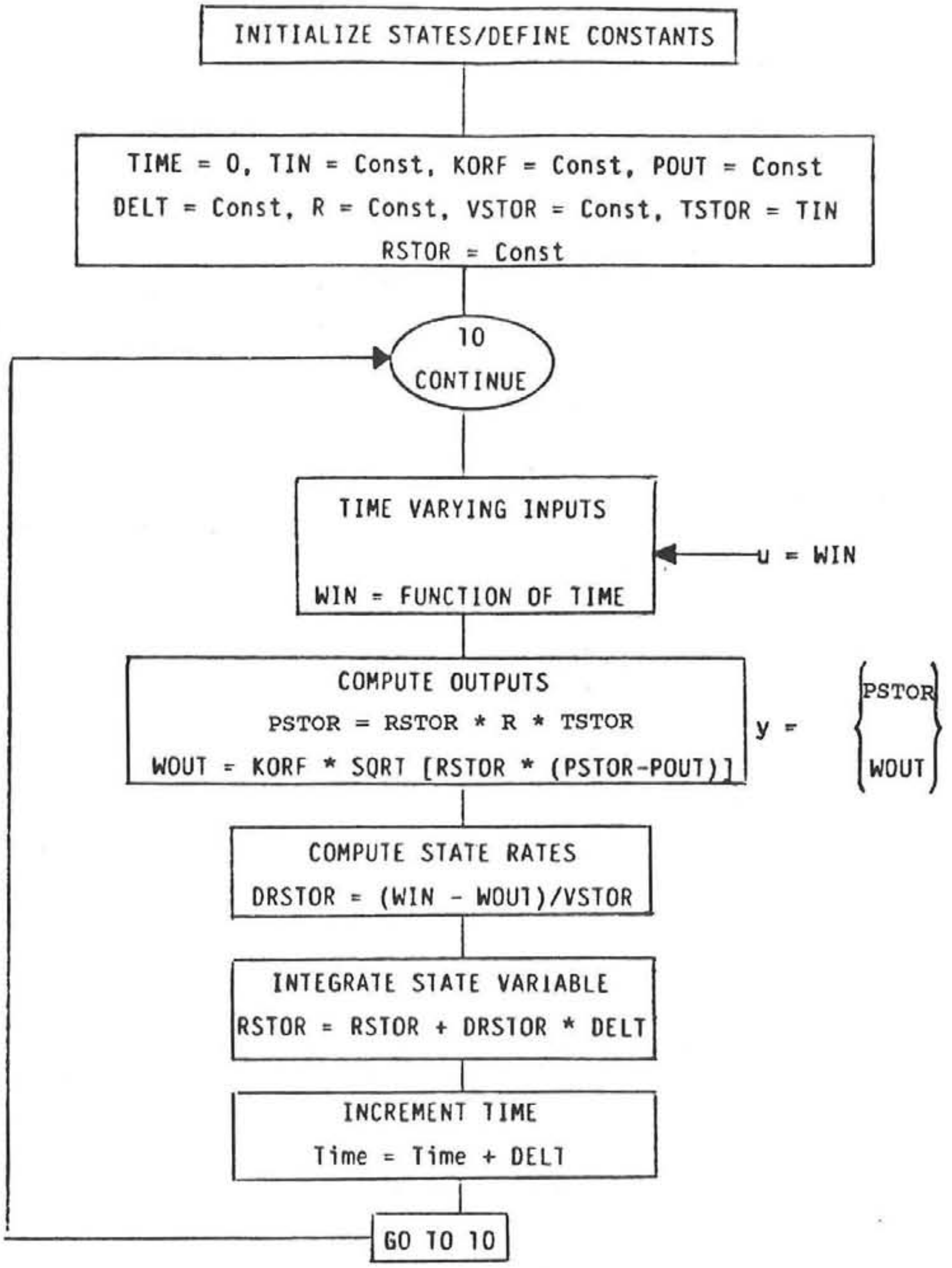

Figure 2-6 Flow Chart for a Fortran Program to Solve Storage Tank Dynamic Problem

```
c   Start of Program

c

    Initialize States/Constants
         FINTIM = Const
         Time = 0
         KORF = Const
         POUT = Const
         DELT = Const
         R = Const
         VSTOR = Const
         TSTOR = TIN
         RSTOR = Const
    10 CONTINUE
         If (Time .GT. FINTIM) GO TO 20
c   Time Varying Input
         WIN = Function of Time
c   Compute Outputs
         POUTS = RSTOR *R*TSTOR
         WOUT = KORF * SQRT [RSTOR*(PSTOR - POUT)]
c   Compute State Rate
         DRSTOR = (WIN - WOUT)/VSTOR
c   Integrate State Variable
         RSTOR = RSTOR + DRSTOR * DELT
c   Increment Time
         Time = Time + DELT
c   Loop to Top of Program
         GO TO 10
    20   CONTINUE
STOP
END
```

Figure 2-7 Fortran Program for Storage Tank

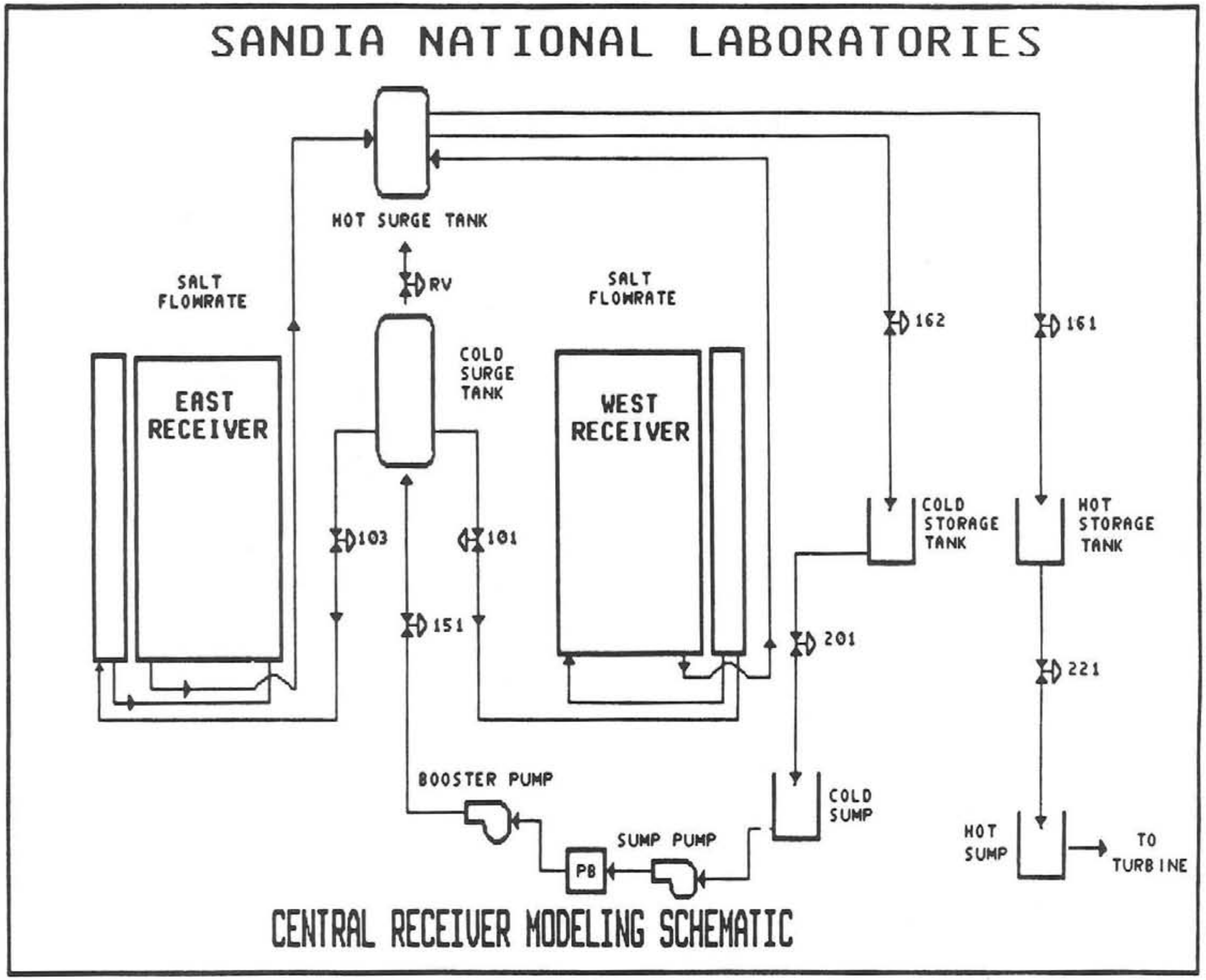

Figure 2-8 Modeling Schematic

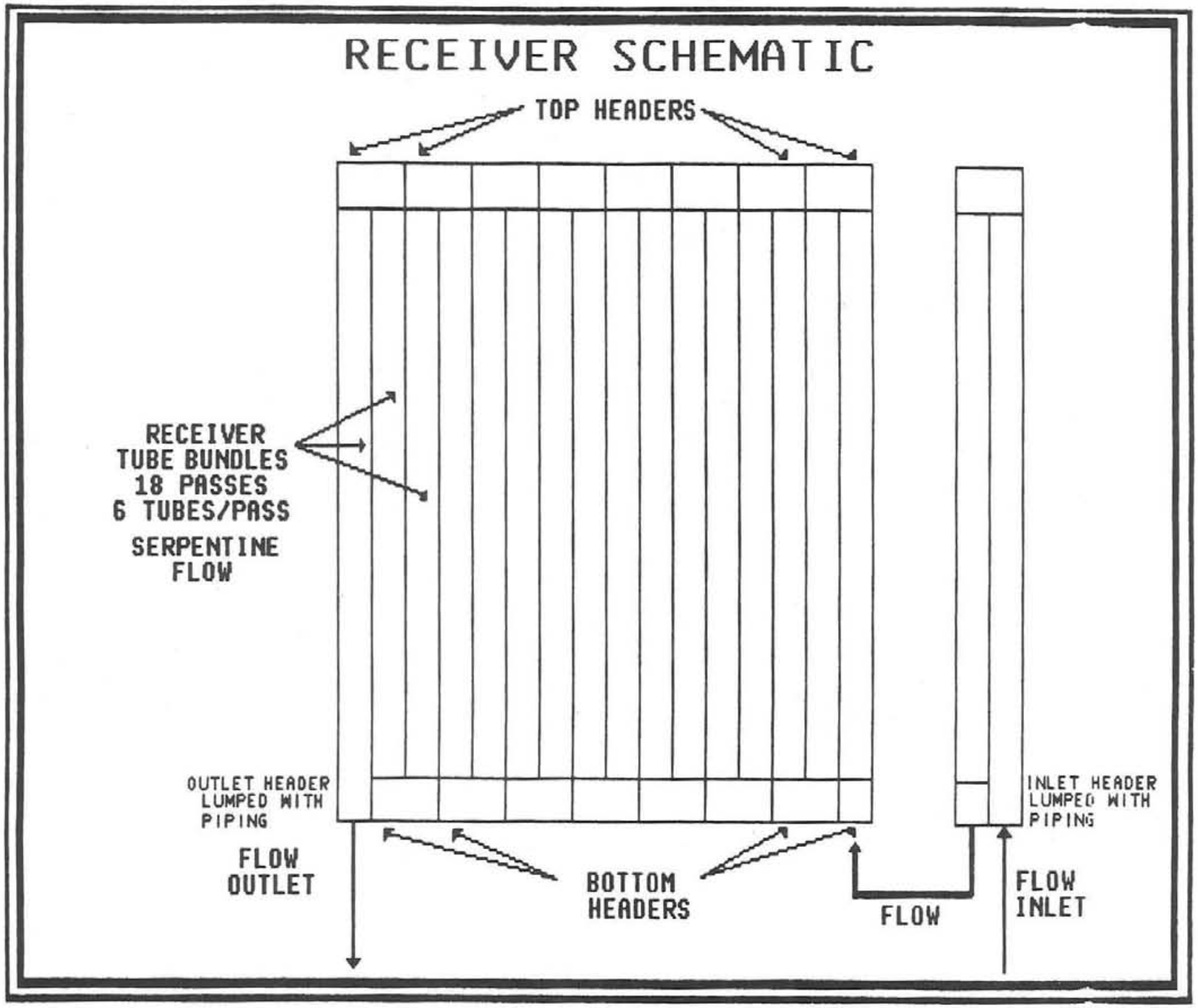

Figure 2-9 Receiver Schematic

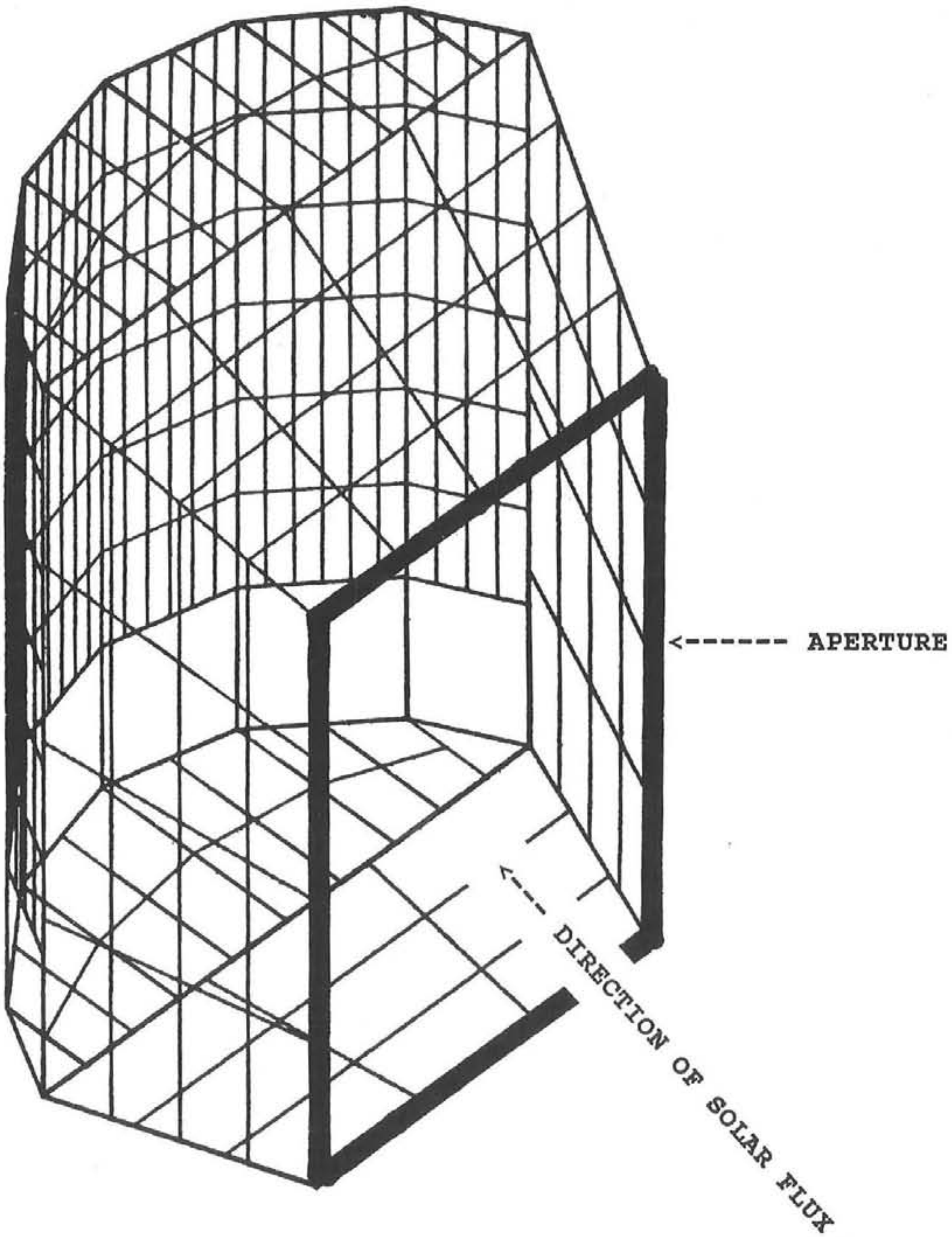

Figure 2-10 Transparent View of Receiver Cavity Showing PATRAN Mesh Elements

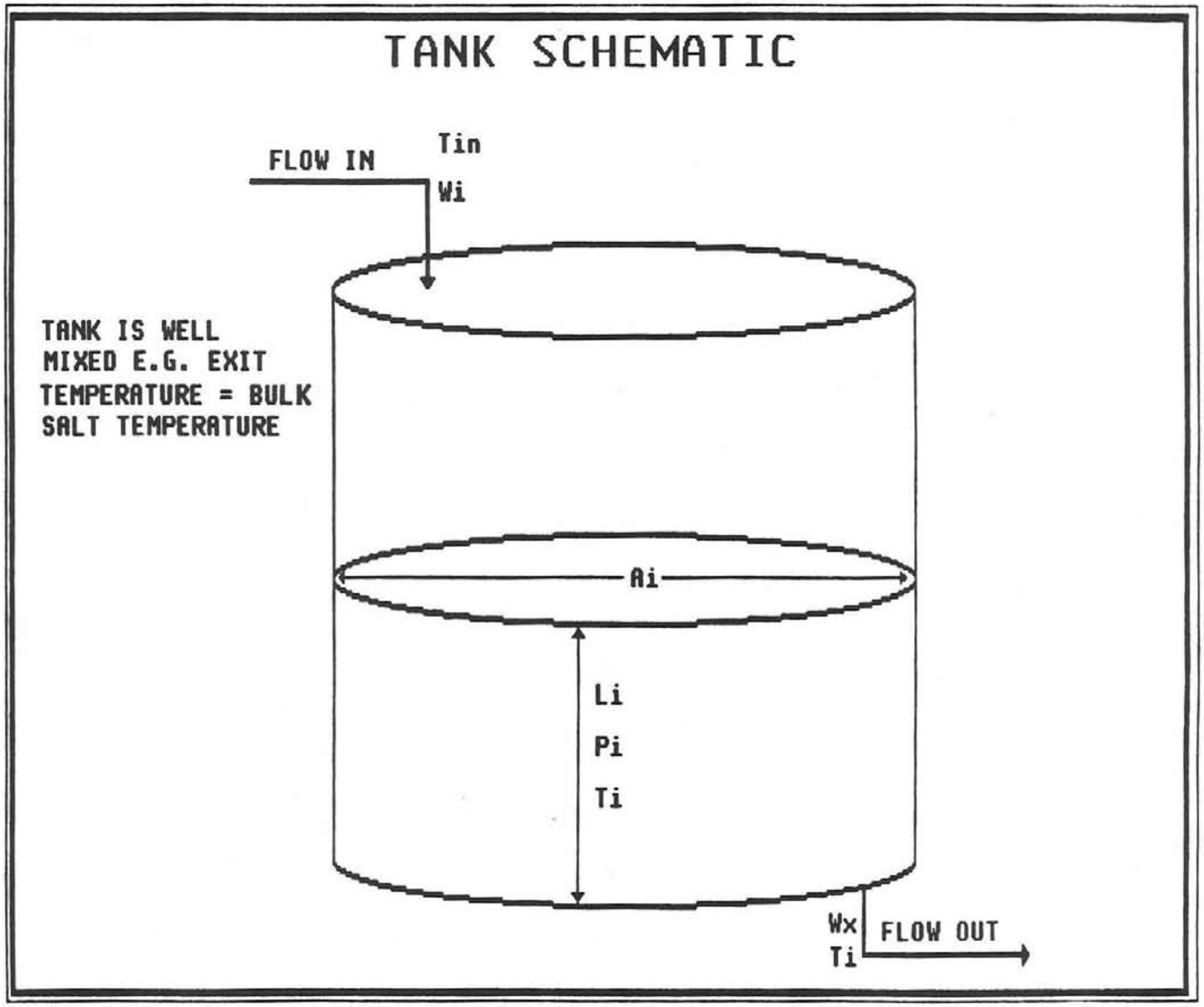

Figure 2-11 Typical Schematic of a Tank

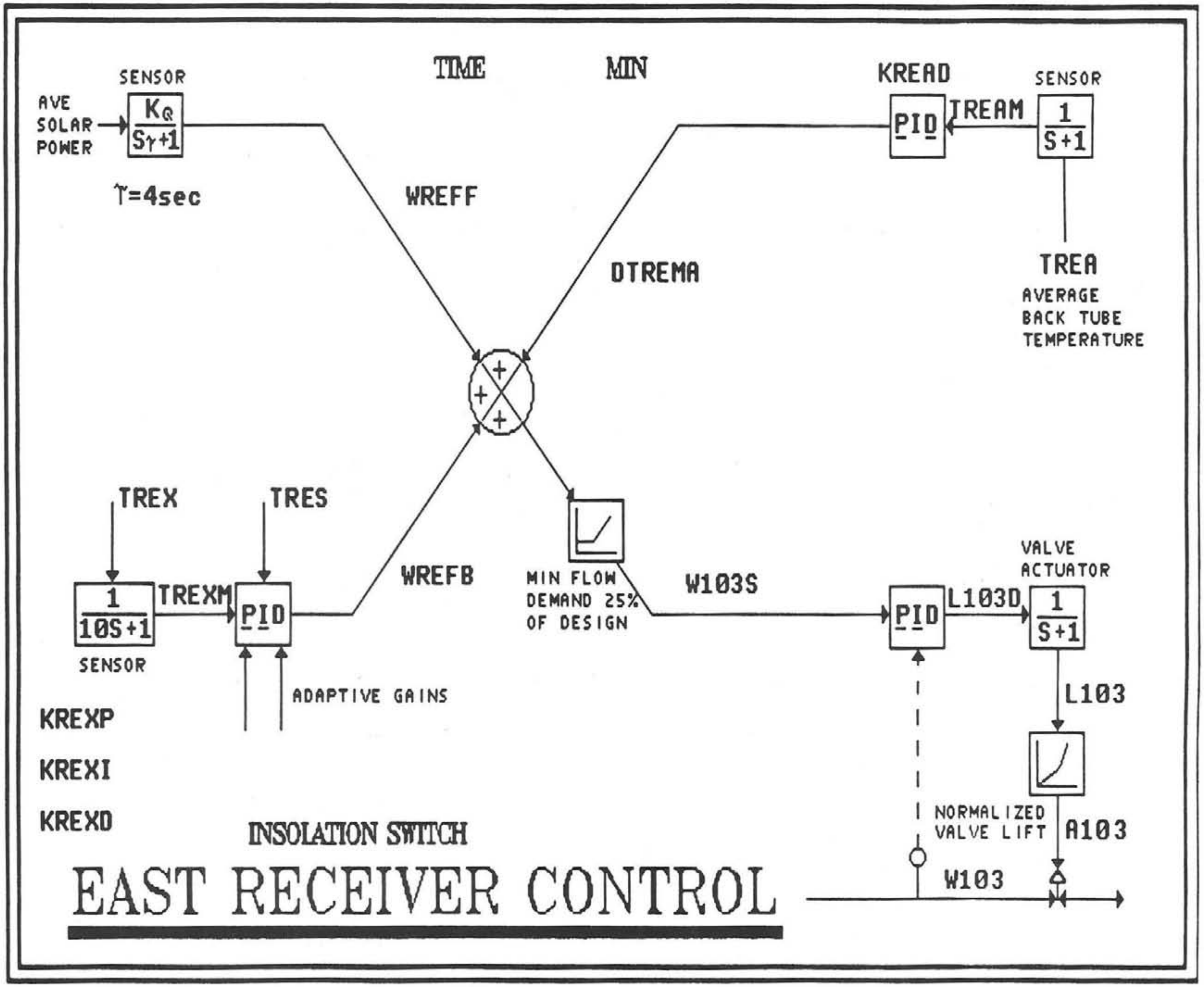

Figure 2-12 East Receiver Control (TREX is the Temperature of Salt Exiting the Receiver and TRES is the Setpoint for Salt Exit Temperature)

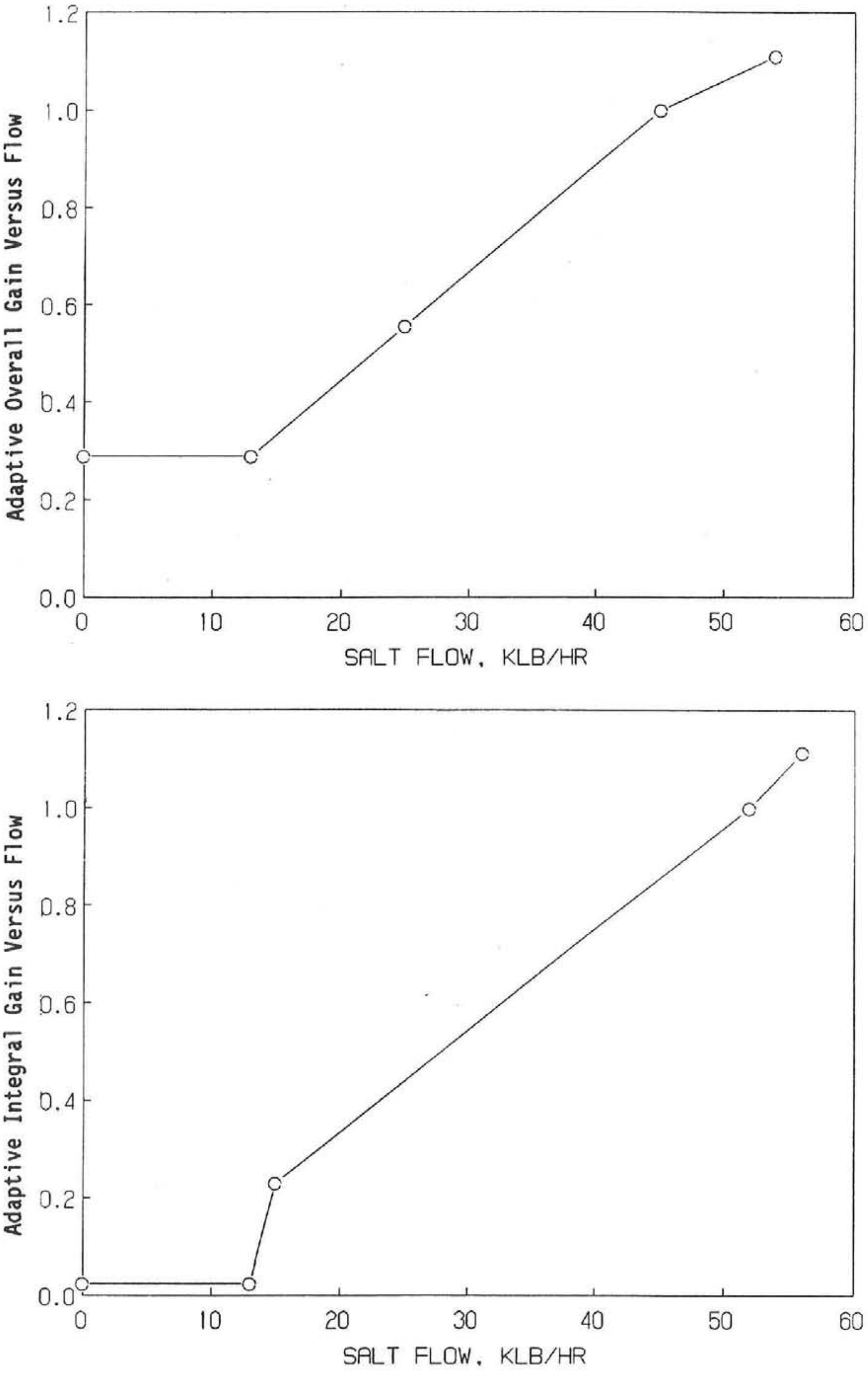

Figure 2-13 Adaptive Gain Functions

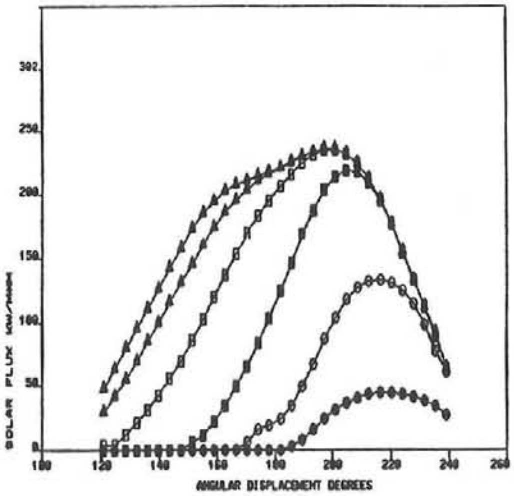

4 PM

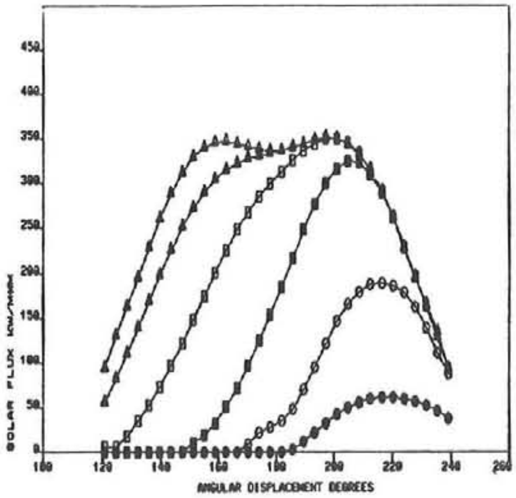

NOON

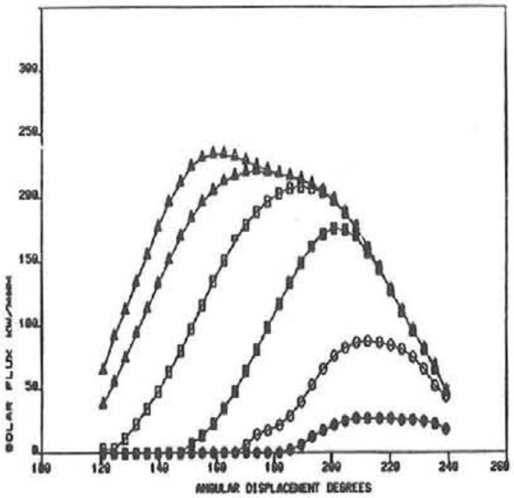

8 AM

Figure 2-14 Solar-Flux-Transient Data for Different Times of the Day (Centerline of the Receiver is 180°).

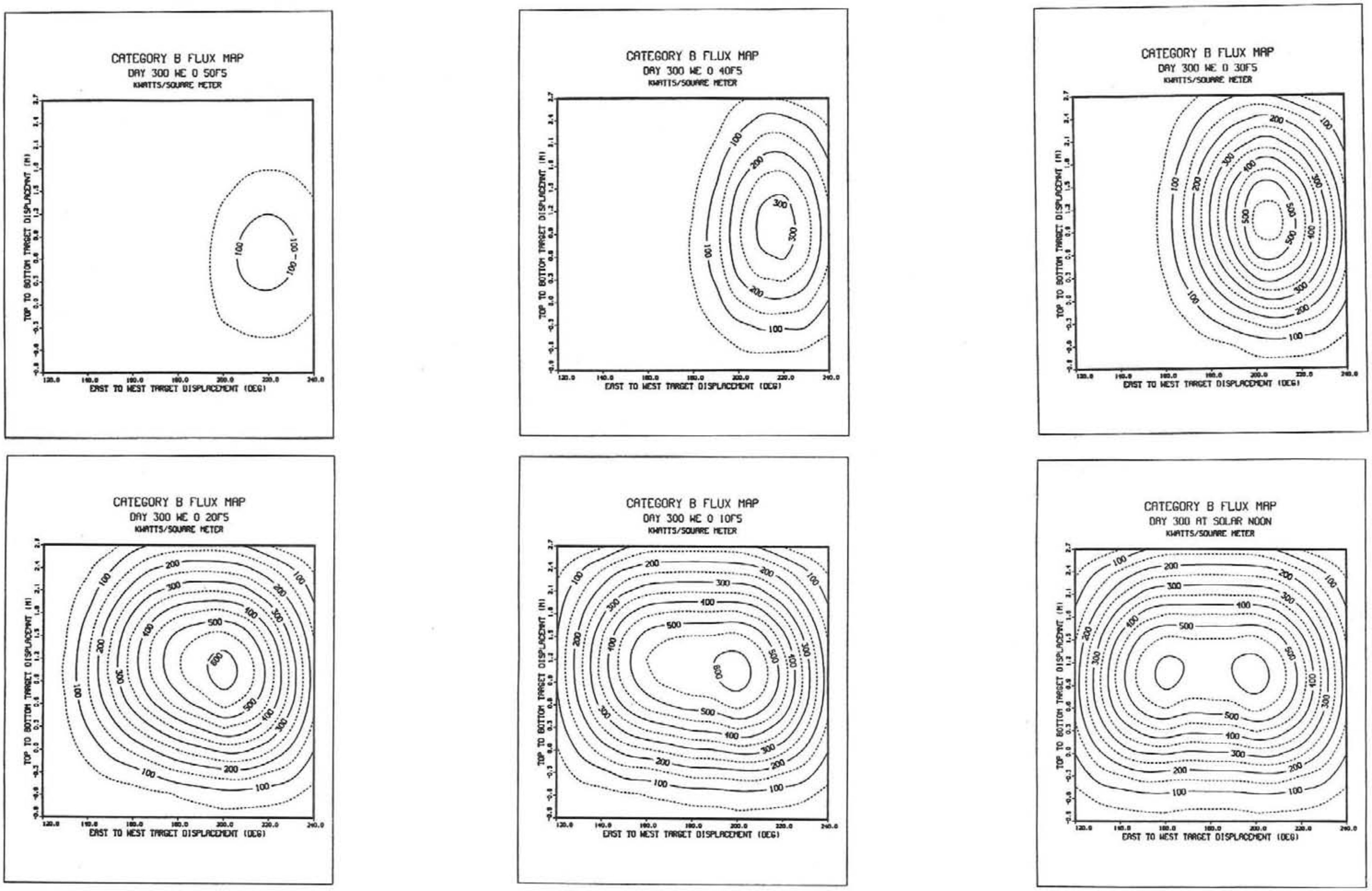

CATEGORY B FLUX MAP
DAY 300 WE 0 50FS
KWATTS/SQUARE METER

CATEGORY B FLUX MAP
DAY 300 WE 0 40FS
KWATTS/SQUARE METER

CATEGORY B FLUX MAP
DAY 300 WE 0 30FS
KWATTS/SQUARE METER

CATEGORY B FLUX MAP
DAY 300 WE 0 20FS
KWATTS/SQUARE METER

CATEGORY B FLUX MAP
DAY 300 WE 0 10FS
KWATTS/SQUARE METER

CATEGORY B FLUX MAP
DAY 300 AT SOLAR NOON
KWATTS/SQUARE METER

Figure 2-15 Two Dimensional Flux Profiles During a Cloud Transient from the DELSOL Computer Code

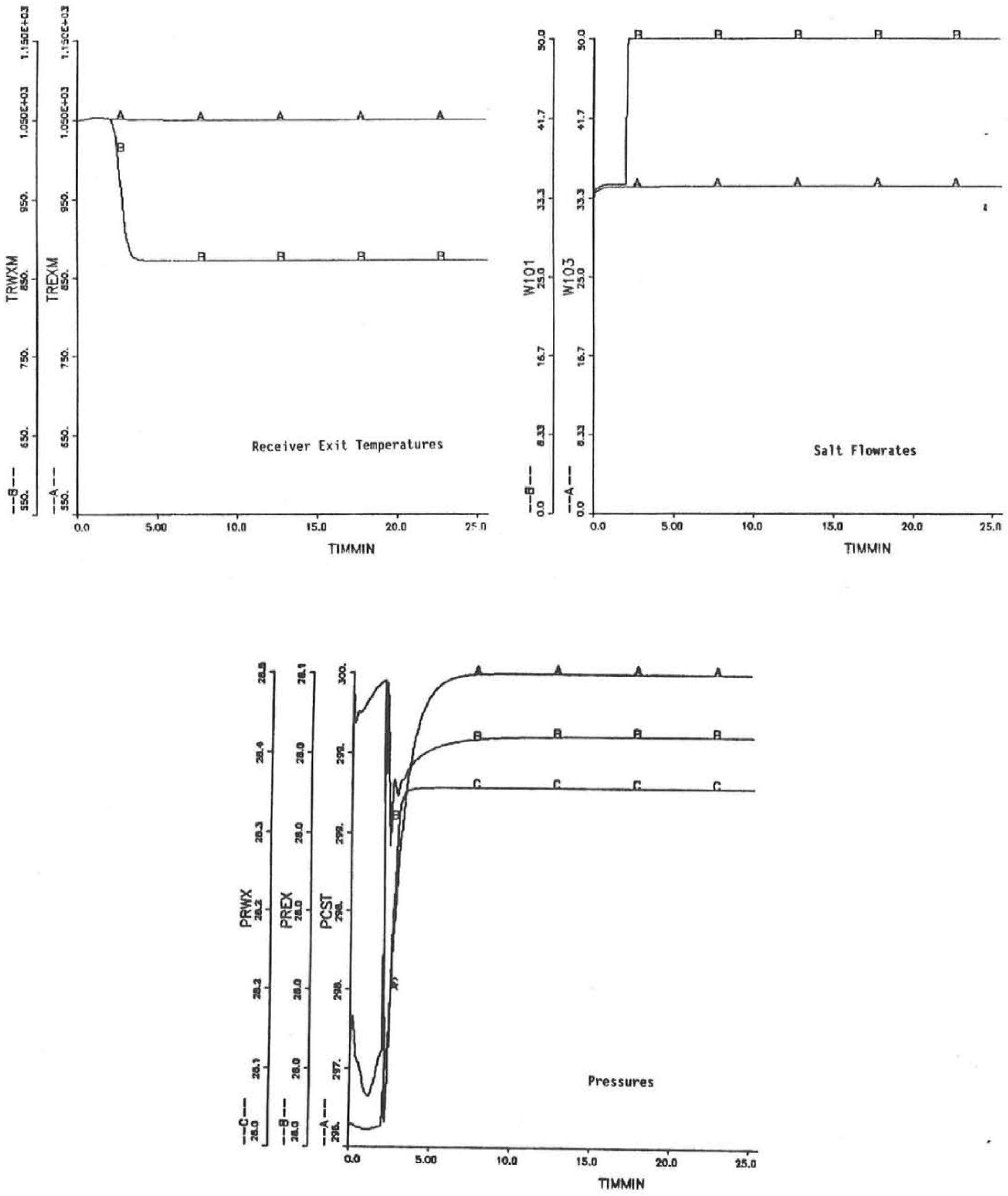

Figure 2-16 Receiver Process Parameters Following a Failure of Valve 101 (Temperatures (F°), Flow Rates (Klb/hr), and Pressure (psi))

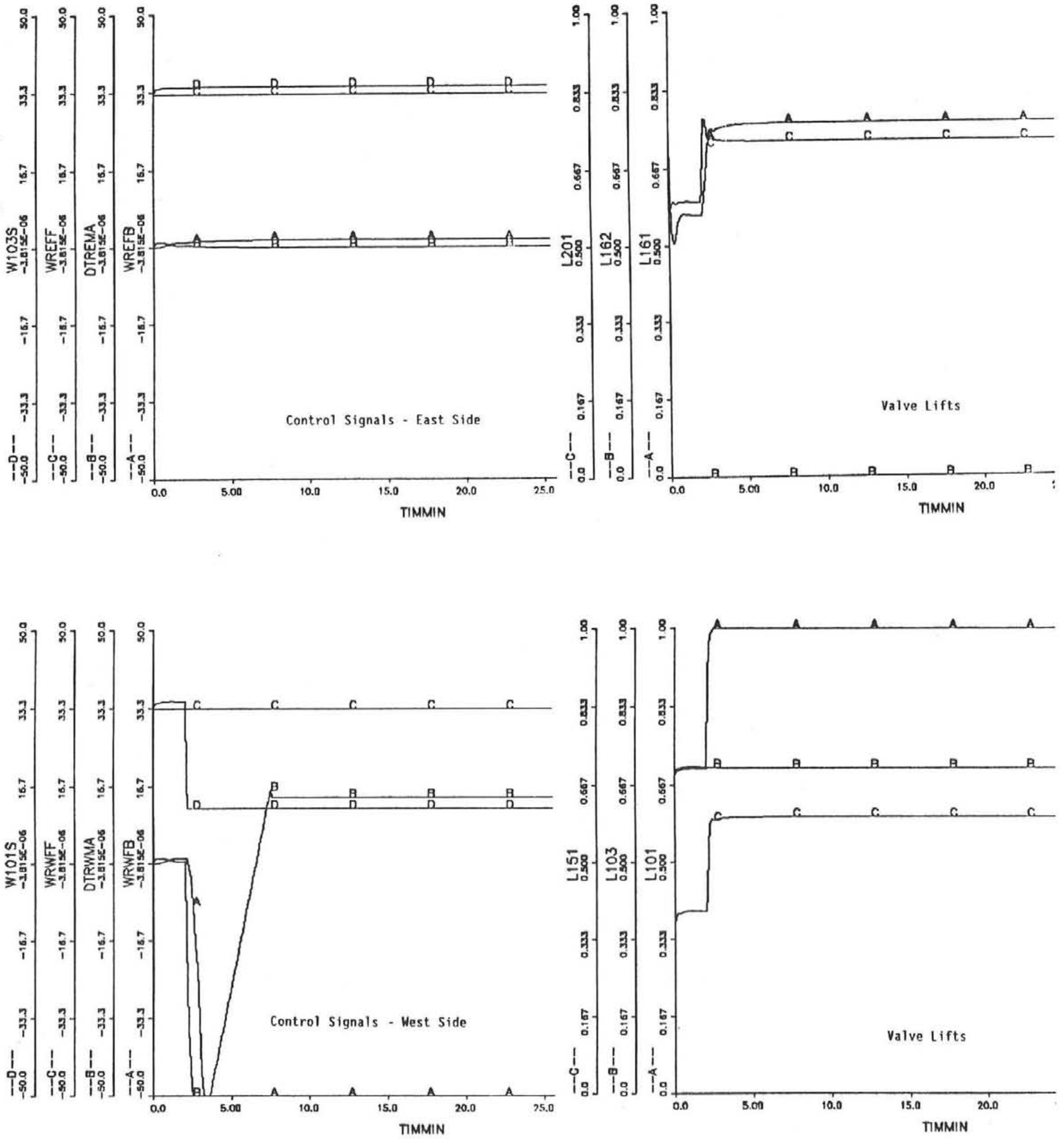

Figure 2-17 Control System Parameters Following a Failure of Valve 101 (Signals (Klb/hr), Lifts (%))

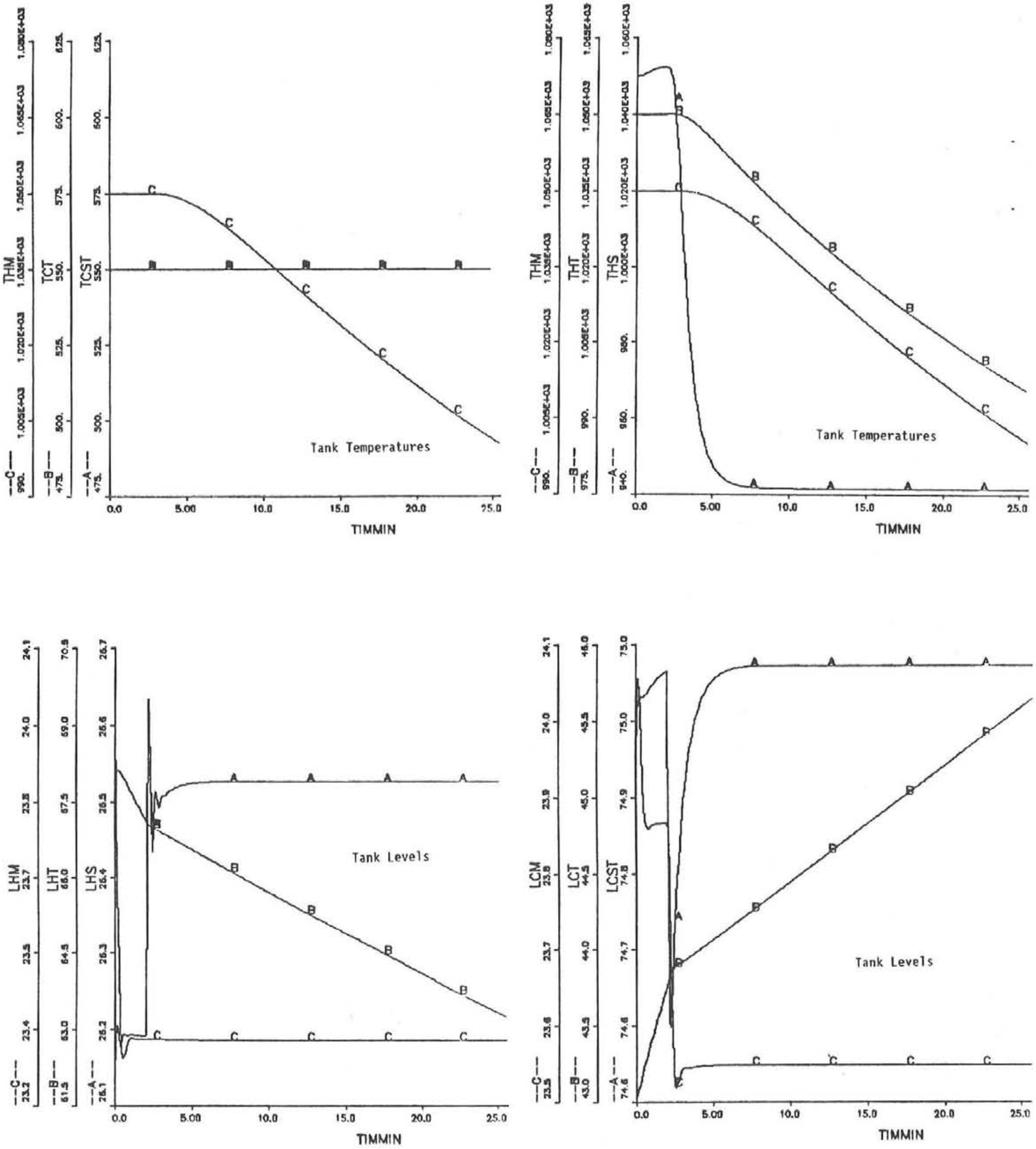

Figure 2-18 Tank Parameters Following a Failure of Valve 101
(Temperatures (F°), Levels (inches))

Chapter 3

Model Validation

Simulation model predictions were validated with data obtained from the actual receiver system. The model can be considered valid if it can predict a reasonable estimate of the actual response of the receiver system given known input disturbances. Though several types of input disturbances are possible, we focused on incident flux perturbations because they routinely occur when clouds pass over the heliostat field. Two sets of experimental data were used: 1) 30 minutes of simulated cloud transients, and 2) 3 hours of natural cloud transients. In both cases the model was validated by comparing receiver parameters such as temperatures, flows, energies, and control signals.

We did not compare hot and cold storage tank parameters because the experimental program focused on the receiver, and data were lacking on the storage system. However, another simulation model of the storage system was previously validated with experimental data developed by another test program (Kolb and Nikolai 1988). The validated storage system model is more complex than that presented in Chapter 2 of this report. This more complex model was shown in Kolb and Nikolai to accurately predict the performance of the storage system.

3.1 Validation of Receiver Model with Simulated Cloud Transients

The data for model validation were obtained from testing on May 4, 1987. The test simulated an 1100-ft cloud moving at 8 ft/s followed by a slightly smaller cloud some 20 minutes later. The cloud was simulated by a programmed removal of heliostats from the receiver in a sequential fashion from west to east and by subsequently placing them back. The tests were conducted between 11 and 11:30 a.m.

For purposes of validation we would have preferred testing at solar noon, so our flux distribution data from day 300 would be more representative, but this was not possible. The problem was that the heat exchanger could not handle the heat load at solar noon, and the salt inventory was too low at the testing time to make up the difference from storage.

A second problem was that the transient-cloud testing was also being used to tune the control system as these tests were being conducted. Although the control system structure was not altered from that presented earlier in this section; ramp rates, gains, and adaptive gain functions were continuously being altered and refined. Refinements continued after the May 4 testing. As a consequence, there are some questions as to the exact status at the time these tests were conducted.

Finally, the model of the Bailey Network 90 was essentially a velocity Form PID provided by McDonnell Douglas. As mentioned in Chapter 2, testing against an actual controller showed identical responses to step and ramp inputs but differing responses to a sinusoidal input. We are not certain whether this difference caused errors in our validation.

The adaptive gain characteristics utilized in the model are presented in Figure 2-13. The adaptive and other gains utilized for the controllers were

Exit Salt Temperature

$K_{sc} = 0.2$ (adaptive)
$K_p = 1.0$
$K_I = 1.5$ (adaptive)
$K_D = 0$

Average Back-Tube Temperature

$K_{sc} = 2.0$ (adaptive)
$K_p = 0.32$
$K_I = 0$
$K_D = 0.046$

where K_{sc} is the overall (adaptive) gain, K_p is the proportional gain, K_I is the (adaptive) integral gain and K_D is the derivative gain.

The exit salt temperature set point was ramped between 850 °F and 1050 °F during the cloud transients. This "sliding" set point T_{setx}, was programmed as follows:

$$T_{setx} = T_{meas} + \text{BIAS}$$

with the following limits

$$850\ °F \le T_{setx} \le 1050\ °F$$

$$-0.75\ °F/s \le \frac{dT_{setx}}{dt} \le 0.5\ °F/s$$

The average back tube temperature set point, T_{setBT}, was varied according to the following equation:

$$T_{setBT} = K(T_{setx} - 550),$$

where K was changed periodically to reflect the changing flux distribution with time of day at the test site. This was not, of course, necessary in simulation. We had only three distributions; one for early morning, solar noon, and late afternoon, and the distribution was not altered during transient cloud runs (except by cloud cover).

The differences in incident receiver flux between plant and model are illustrated in part by the feedforward signals in Figures 3-1a and 3-2a. (Feedforward signals are expressed in flow units of Klb/hr. However, this signal is directly proportional to the flux incident upon the receiver.) Variables preceded by an S are actual plant data. Notice that east and west side signals are equal for the simulation, while east is larger than west for the experimental data. This difference shows approximately a 10 percent higher flux on the east receiver than on the west receiver at the time the test was conducted. The model flux was scaled to approximate the average of the two without altering the flux distribution given earlier at solar noon.

The signals are equal in the simulation because a flux map for solar noon was assumed. The flux was higher on the east for the experimental data because the flux was recorded prior to solar noon; before noon the flux is higher on the east (see Figure 2-14). Some difference in the integrated east and west fluxes is evident, particularly the west fluxes. The main difference is in the slope of the west signals as the cloud clears. It is not known whether this is due to time of day differences or to slower return than withdrawal of the heliostat.

The response of the east receiver is considered first since (a) the flux distributions for the simulation and experimental data are predictably closer and (b) they suggest a probable difference in controller parameters, although we were unable to confirm that such was the case.

The exit measured temperatures for the east receiver are compared in Figure 3-1b. The results are in excellent agreement, as are the comparisons of exit temperature set point of Figure 3-1c. The slopes of the sliding temperature set points confirm that the rate limits were the same for plant and model. Comparison of exit feedback signals in Figure 3-1d produces the first indication that differences exist between the model and the actual receiver. The comparison is quite good until the sun returns from the first transient. The model feedback signal suddenly and sharply drops to twice its previous value. A much smaller and less pronounced reaction occurs in the actual feedback signal about 20-30 seconds later. Recalling that the adaptive gain functions reduce controller gains at low flow, we decided to cross plot both feedback signals, the feedforward signal (WREFF) and the total flow control signal (W103S) together for the model (Figure 3-1g) and then for the actual plant (Figure 3-1e). As seen in Figure 3-1g, the sudden drop in feedback signal coincides with the sudden increase in total flow controller signal (predicted model flow rates cannot be discerned from total flow control signal) and hence the return to full gains through the adaptive signal. This occurs at a time when the measured exit temperature error of the model is near its maximum, hence the large reduction in model feedback error. The timing is similar for the actual plant, as seen in Figure 3-1e, but the exit temperature feedback signal reacts later (if the subsequent small decrease about 20 seconds later is a reaction). The most likely explanation is that the plant's flow rate increase is delayed sufficiently so that by the time it restores controller gains, the measured temperature is close to the setpoint.

The comparison of average back tube feedback signals is shown in Figure 3-1f. The signals are similar in shape but different in amplitude. It is difficult to assess these differences because these signals are quite sensitive to flux distributions. It is interesting to compare signals upon the sun's return for the first transient. Both signals start slowly upward then break more sharply. The break occurs later in the plant signal than in the model. This is consistent with our observations on the feedback signals.

The average back tube offset for the model controller is larger than for the plant controller. The difference is approximately equal to the sudden drop in exit temperature feedback signal. The offset occurs because exit and back tube controllers both have proportional paths. Some offset always occurs.

The west side transient comparisons are predictably worse since the feedforward signals (i.e., flux signals) are not nearly as well aligned as for the east receiver (recall Figure 3-2a). The principal factor in these more pronounced differences is that the flux distribution for the receiver on the sun side is quite similar to that at solar noon, while the opposite side is substantially different (see Figure 2-14, recalling that the left side is east). Another factor is that minor differences in cloud timing and speed are magnified on the west side since the cloud must pass across approximately 40 percent of the field before the west side is impacted at all.

Comparison of measured exit temperatures is shown in Figure 3-2b. Comparison of exit salt temperature set points is given in Figure 3-2c. Exit and back tube feedback signals are shown in Figures 3-2d and 3-2f, respectively. Finally, all controller outputs for the model (Figure 3-2g) and for the plant (3-2e) are given. Plant and model responses differ in both amplitude and phase. Only in shape are they generally similar.

The cold surge tank pressure and level responses to the previously described transients are shown in Figures 3-3. Pressure control is achieved by varying salt flow into the surge tank. This is accomplished by varying throttle valve 151 with a PID controller (this valve is depicted on Figure 2-8). The theory is that the pressure of the gas above the liquid level will increase or decrease due to variations in both the inlet and outlet salt flows of the tank.

As would be expected, the cold surge tank model response and control are affected by the gains employed by the PID controller.

We used

$K_{SC} = 0.05$
$K_p = 1.0$
$K_I = 1.2$
$K_D = 0$,

values obtained from McDonnell Douglas. As stated earlier, it is possible that slightly different controller gains were employed during the experiment; this could account for differences between the model and the actual plant.

In summary, we conclude that the simulator produced a reasonable prediction of receiver performance during simulated clouds. Receiver performance is judged by the amount of power delivered to the salt that is exiting the receiver. This energy is the product of exit salt temperature (TREXM on the east and TRWXM on the west), salt flow rate (W103 on the east and W101 on the west), and specific heat. Comparing the simulation predictions for these variables with the actual data indicates that they are fairly well aligned. Errors in the simulation appear to be attributed to differences in flux distributions on the western half of the receiver. As stated at the beginning of this chapter, a model is considered valid if it can predict actual system performance given a **known** input disturbance. Since the input disturbance (flux distribution) was not exactly known in this case, one cannot conclude that errors in the simulation model caused the differences shown. In the next section we attempt to obtain a better estimate of the input flux disturbances.

3.2 Validation of Receiver Model with Natural Cloud Transients

On May 14, 1987, the receiver was allowed to operate under totally automatic control between 11:13 a.m. and 2:10 p.m. It was a very cloudy day, and during that time intermittent clouds passed over the CRTF heliostat field. A plot of the solar power incident on the east (KPCTE) and west (KCPTW) receiver panels during these three hours is presented in Figure 3-4. These plots are in normalized units and were obtained by averaging the signals from the flux sensors located on the east and west receiver panels.

The flux sensors do not give an accurate measure of the absolute value of incident flux but do give a fairly accurate relative measure. Consequently, we multiplied the flux sensor data by a single calibration constant so that the simulator prediction of flow rate for each panel matched the actual flow rates with the receiver at steady-state at the start of the simulation. This assured that the flux disturbances input to simulation were similar to those experienced by the actual receiver.

A comparison of the simulated and actual receiver response to the flux disturbance depicted in Figure 3-4 is presented in Figures 3-5 through 3-7. In Figure 3-5 we compare panel outlet temperatures. Panel flow rates and total energy exiting the receiver are displayed in Figures 3-6 and 3-7, respectively. It can be seen that the model produces an excellent prediction of the actual receiver performance.

The energies that are compared in Figure 3-7 were calculated with the following equation:

$$E(t) = \int_0^t W * C_p * (T_{out} - T_{ref}) * dt \quad ,$$

where

W = panel flow rate (lbm/s),
C_p = specific heat of molten salt (0.365 Btu/lbm °F),
T_{out} = salt-exit temperature (°F), and
T_{ref} = salt-reference temperature (550 °F).

The energy delivered by the actual receiver was 1.66×10^7 Btu. The simulation model predicted 1.59×10^7. The simulation prediction was 5.4 percent too low.

The differences between the model and the actual receiver are generally random, except the outlet temperature during rapid heating and cooling of the receiver. In these cases a small bias can be noted; during rapid heating, the model outlet temperature rises more quickly than the actual, and during rapid cooling the model outlet temperature drops more quickly than the actual. We believe this bias can be attributed to the fact that we did not model the cavity structure that surrounds the receiver panels. This structure (see Figure 2-2) contains some thermal mass and therefore adds thermal inertia to the cavity receiver. We did not model this structure because 1) the cavity walls are covered with lightweight insulation that possesses a small amount of heat capacity compared with receiver panels, and 2) a complex heat transfer model would have to be developed to include the effect of the cavity structure. Considering the relatively small amount of bias, we believe the approach we took is warranted.

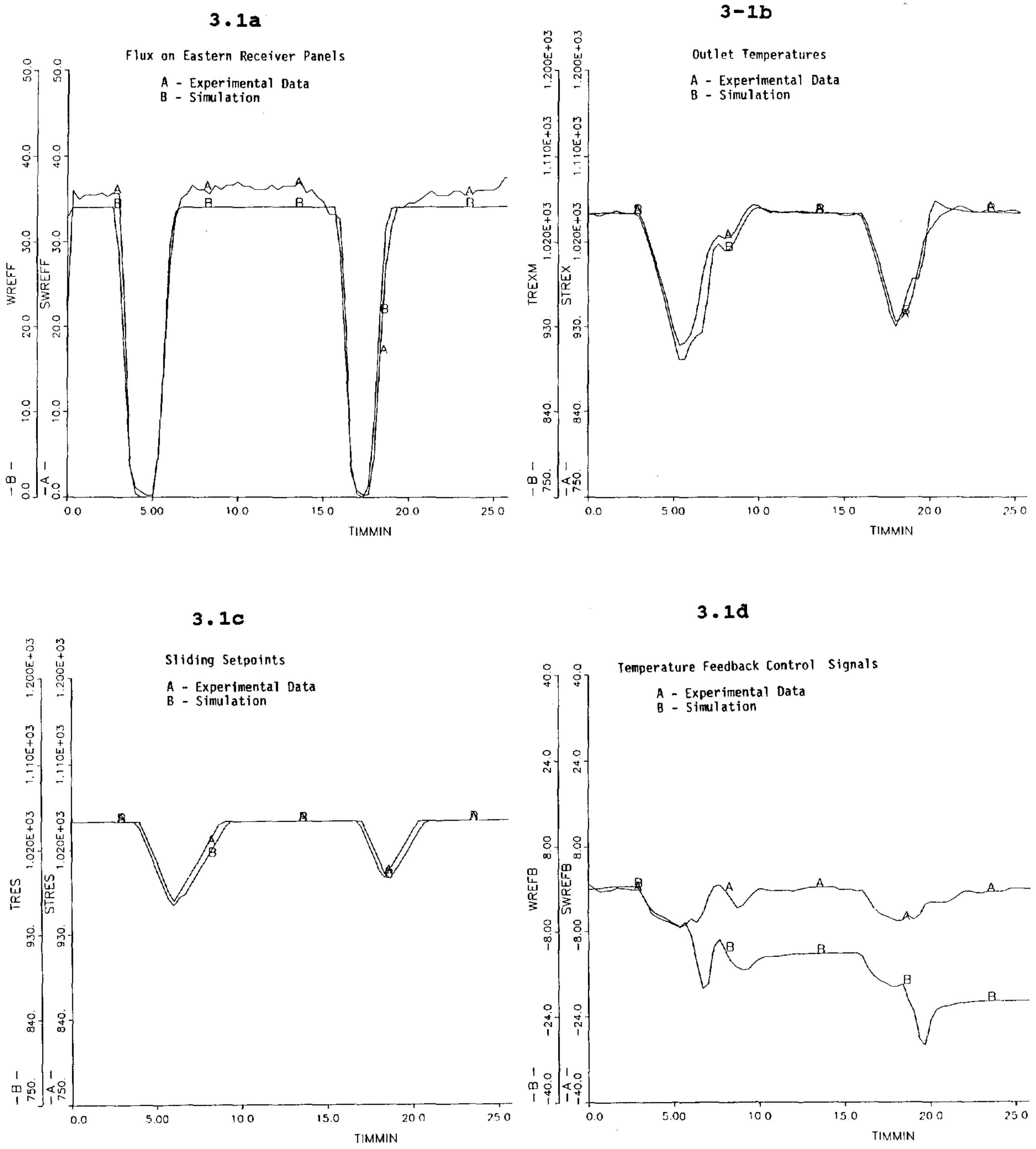

Figure 3-1 Comparison of the Actual and Simulated Response of the East Receiver to a Simulated Cloud Transient (Flux, Control Signals, and Flow Setpoints [Klb/hr], Temperatures and Temperature Setpoints [°F])

3.1e

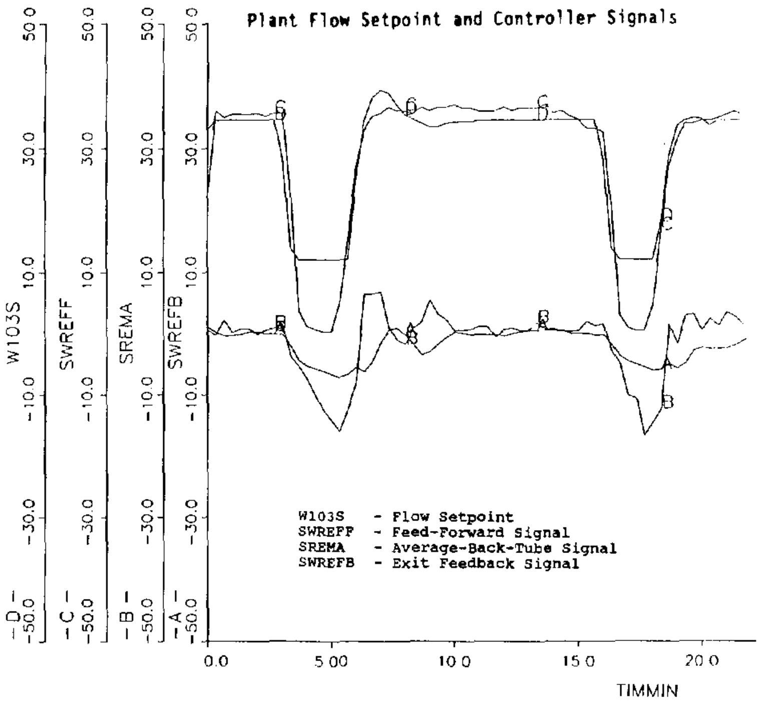
Plant Flow Setpoint and Controller Signals
W103S
SWREFF
SREMA
SWREFB
50.0
30.0
10.0
-10.0
-30.0
-50.0
-D-
-C-
-B-
-A-
W103S - Flow Setpoint
SWREFF - Feed-Forward Signal
SREMA - Average-Back-Tube Signal
SWREFB - Exit Feedback Signal
0.0
5.00
10.0
15.0
20.0
TIMMIN

3.1f

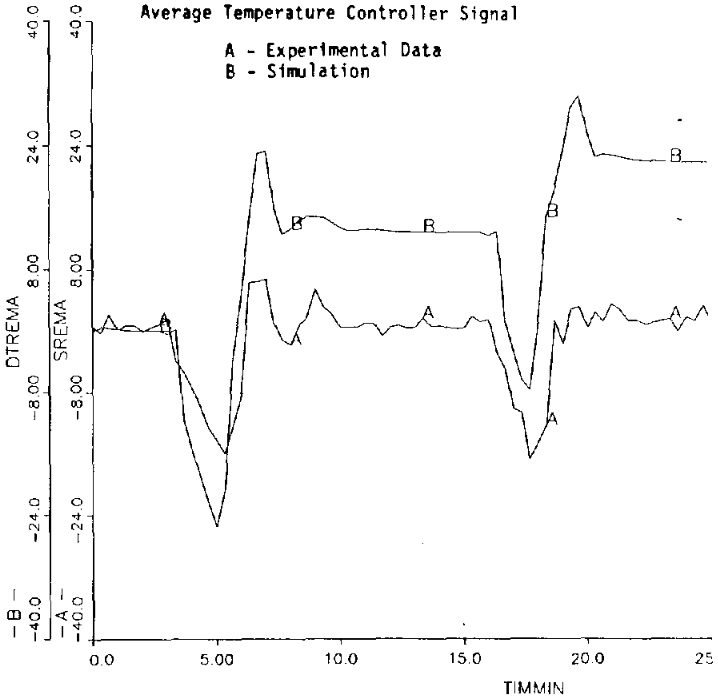
Average Temperature Controller Signal
A - Experimental Data
B - Simulation
DTREMA
SREMA
40.0
24.0
8.00
-8.00
-24.0
-40.0
-B-
-A-
0.0
5.00
10.0
15.0
20.0
25
TIMMIN

3.1g

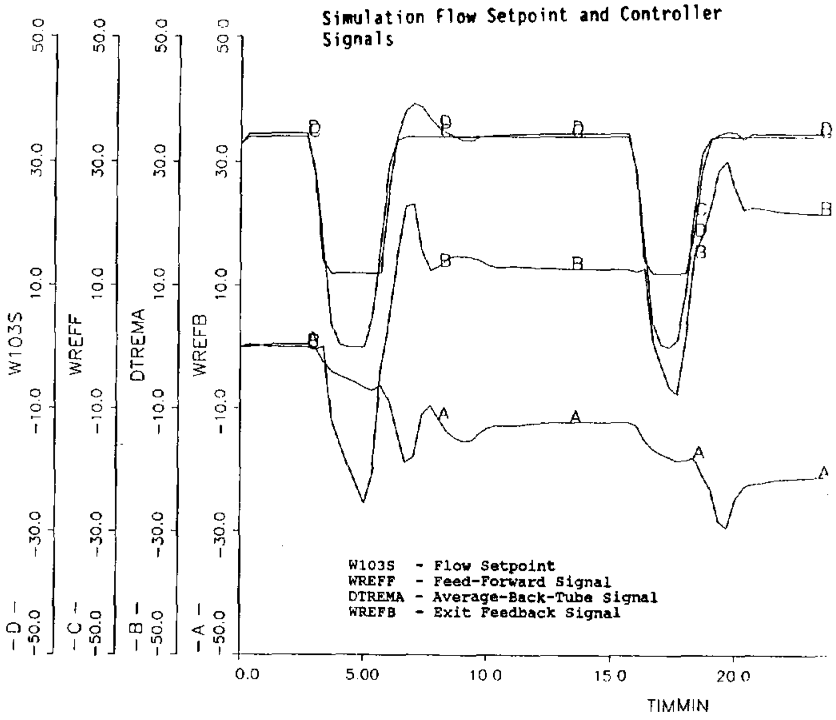
Simulation Flow Setpoint and Controller Signals
W103S
WREFF
DTREMA
WREFB
50.0
30.0
10.0
-10.0
-30.0
-50.0
-D-
-C-
-B-
-A-
W103S - Flow Setpoint
WREFF - Feed-Forward Signal
DTREMA - Average-Back-Tube Signal
WREFB - Exit Feedback Signal
0.0
5.00
10.0
15.0
20.0
TIMMIN

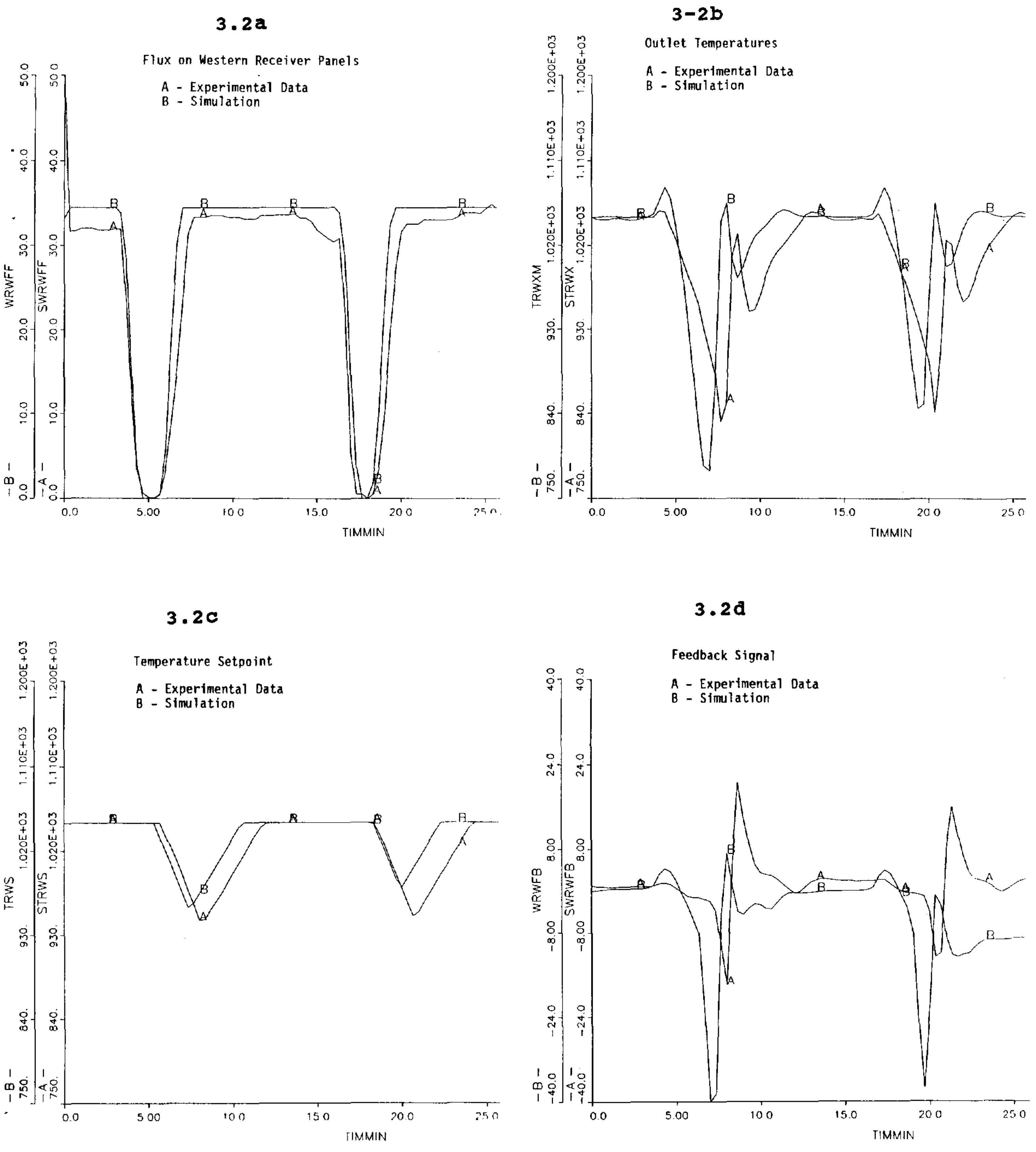

Figure 3-2 Comparison of the Actual and Simulated Response of the West Receiver to a Simulated Cloud Transient (Flux, Control Signals, and Flow Setpoints [Klb/hr], Temperatures and Temperature Setpoints [°F])

3.2e

Plant Flow Setpoint and Controller Signals

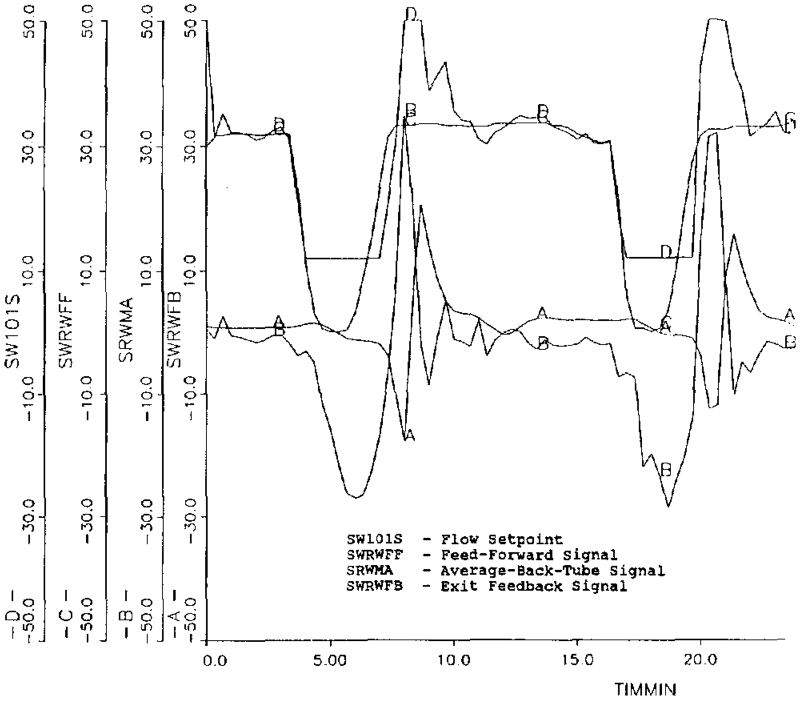

3.2f

Average Temperature Controller Signal

A - Experimental Data
B - Simulation

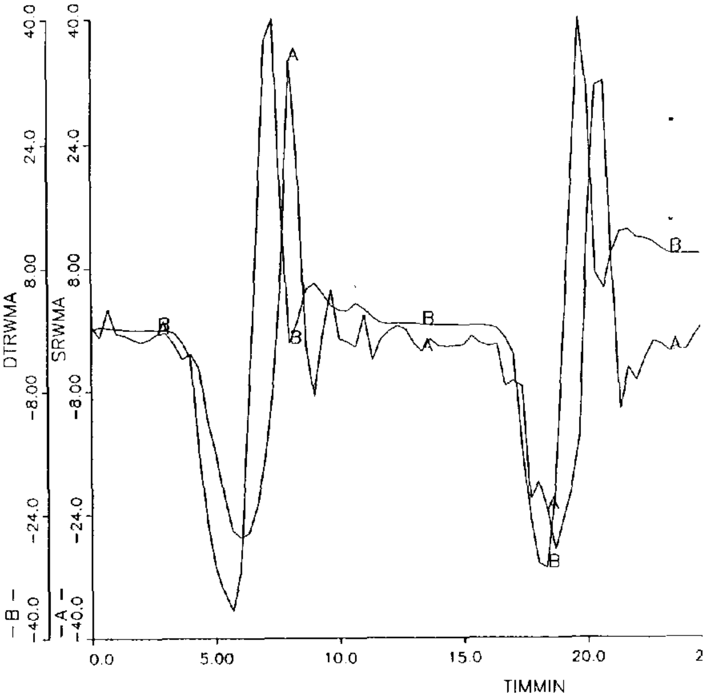

3.2g

Simulation Flow Setpoint and Controller Signals

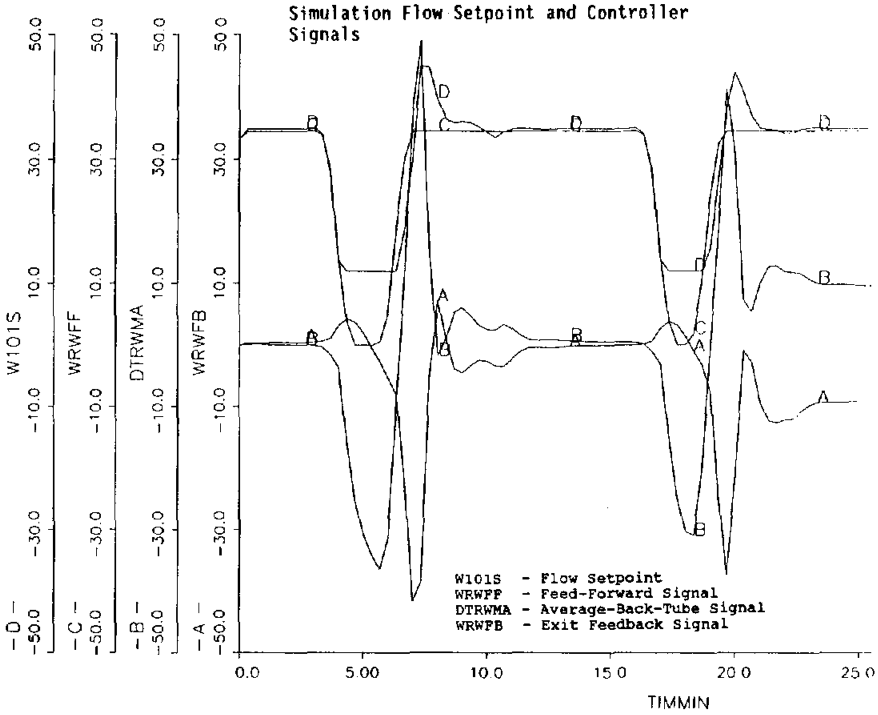

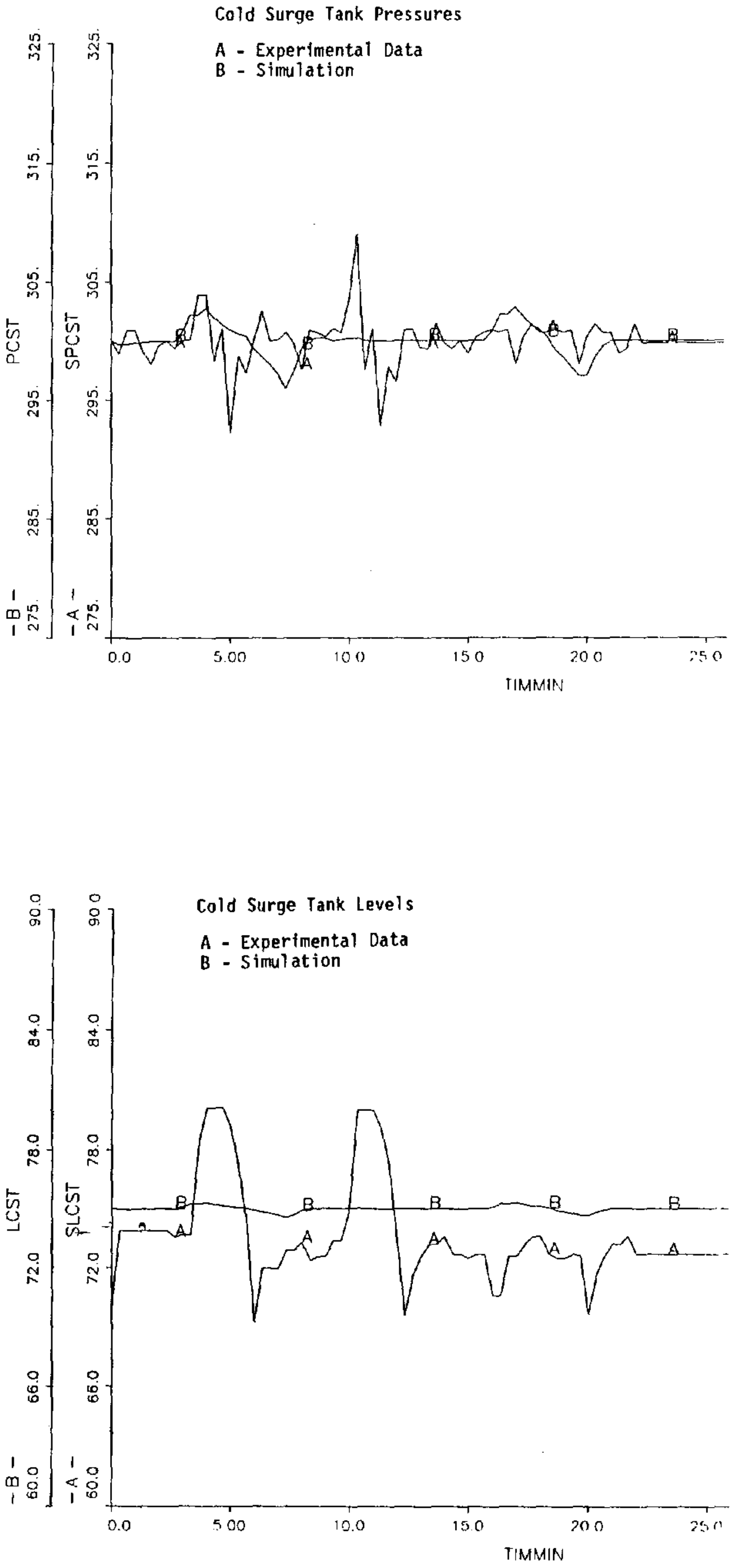

Figure 3-3 Comparison of the Actual and Simulated Response of the Cold Surge Tank to a Simulated Cloud Transient, (Pressures (psi), Levels (inches))

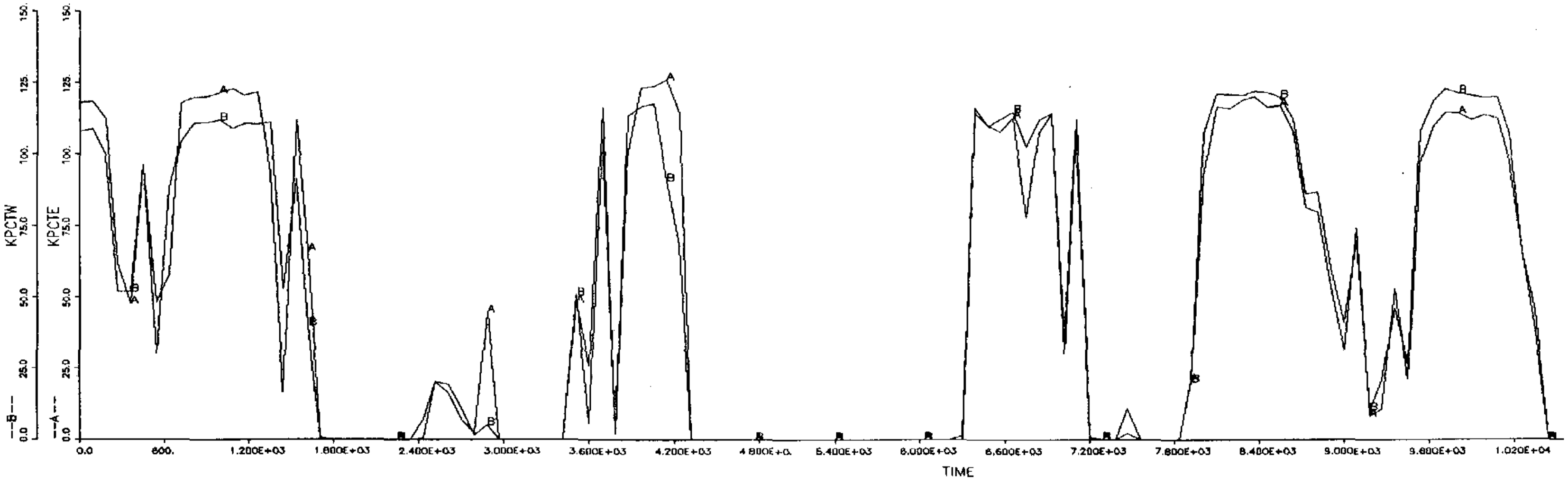

Figure 3-4 Normalized Flux Meter Readings on the East (KPCTE) and West (KPCTW) Receiver Panels During Intermittent Cloudy Weather

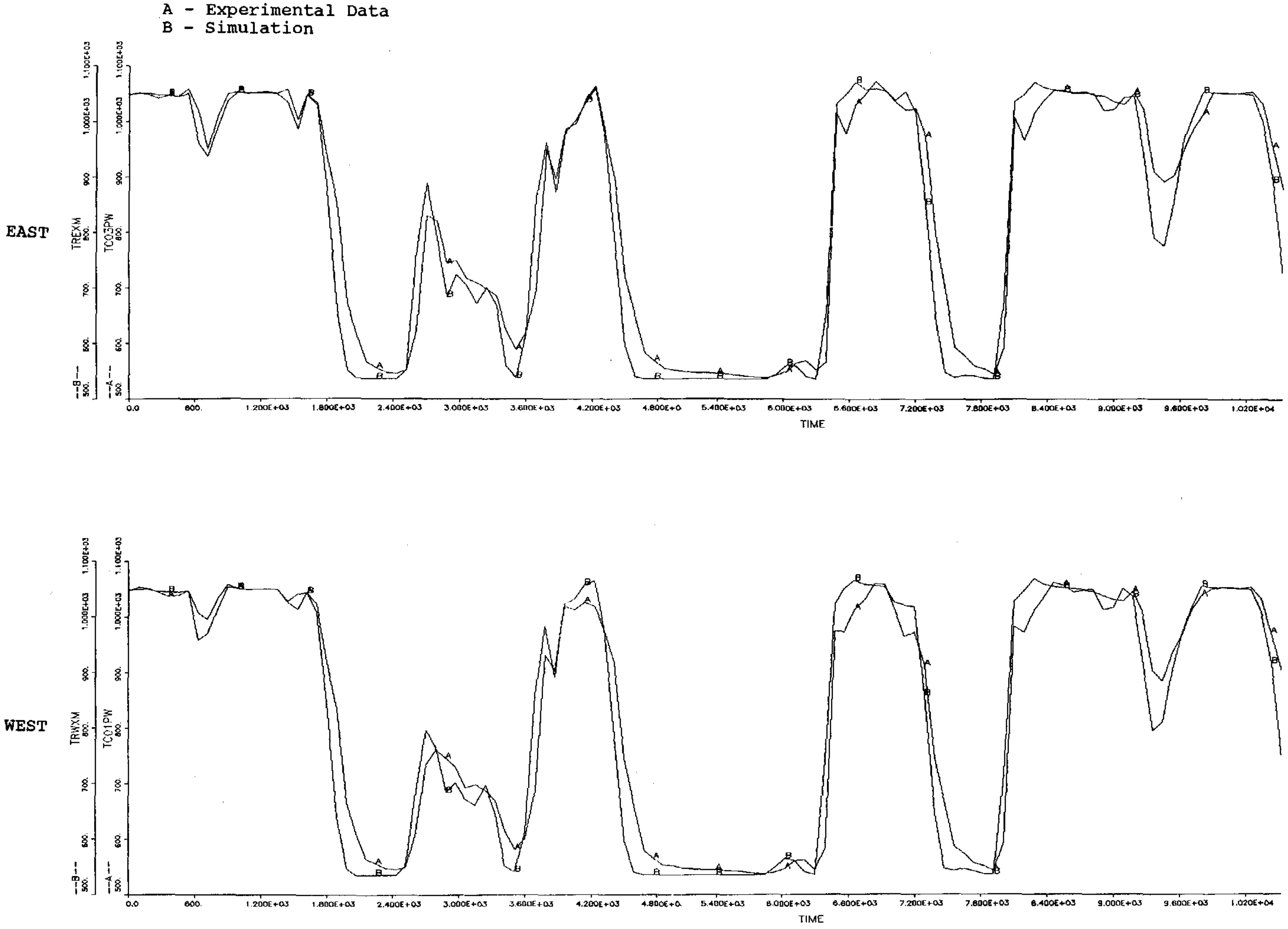

Figure 3-5 Comparison of Actual and Simulated Response of the Receiver Exit Salt Temperatures During Natural Cloud Transients (F°)

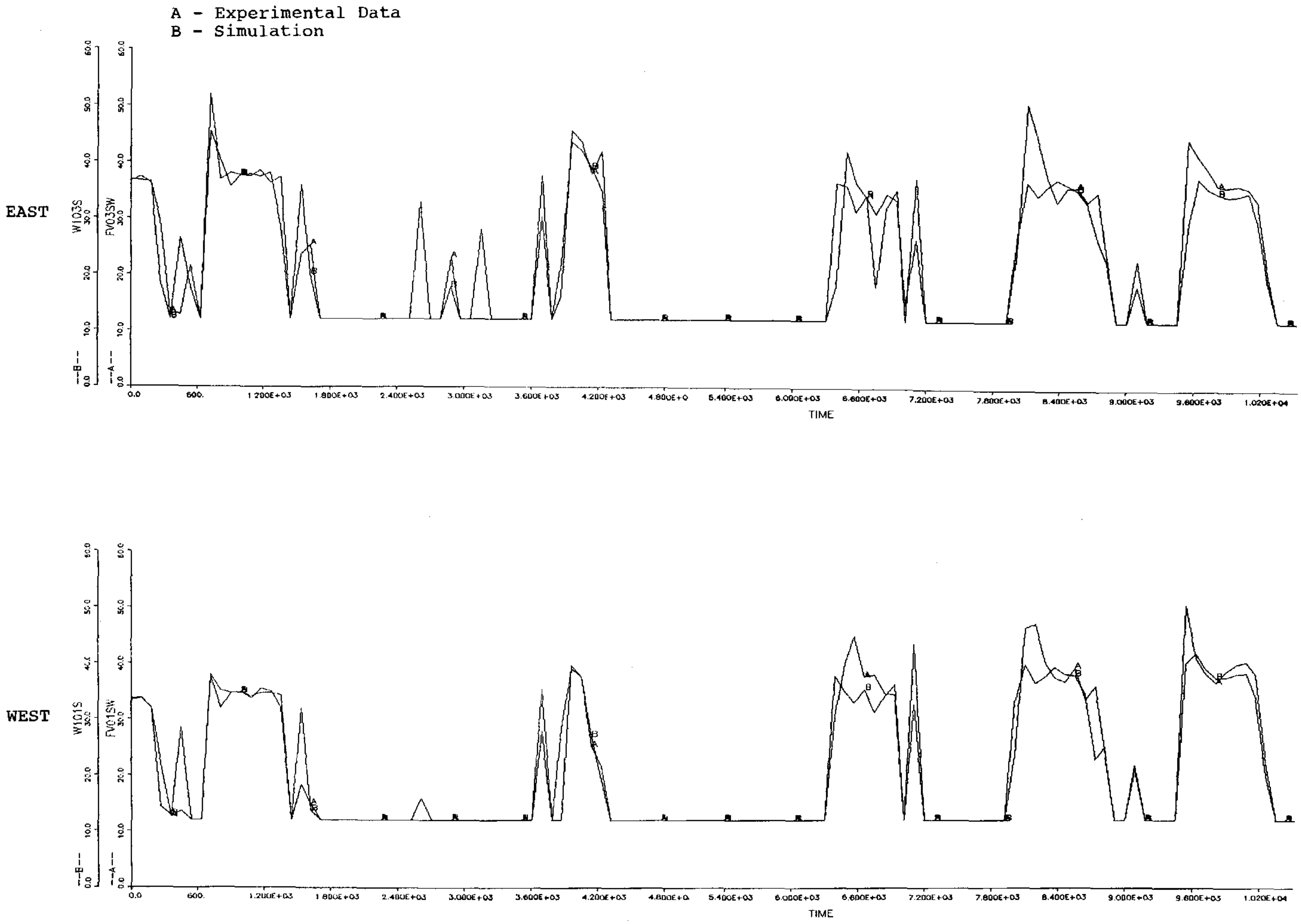

Figure 3-6 Comparison of Actual and Simulated Response of the Receiver Flow Rates During Natural Cloud Transients (Klb/hr)

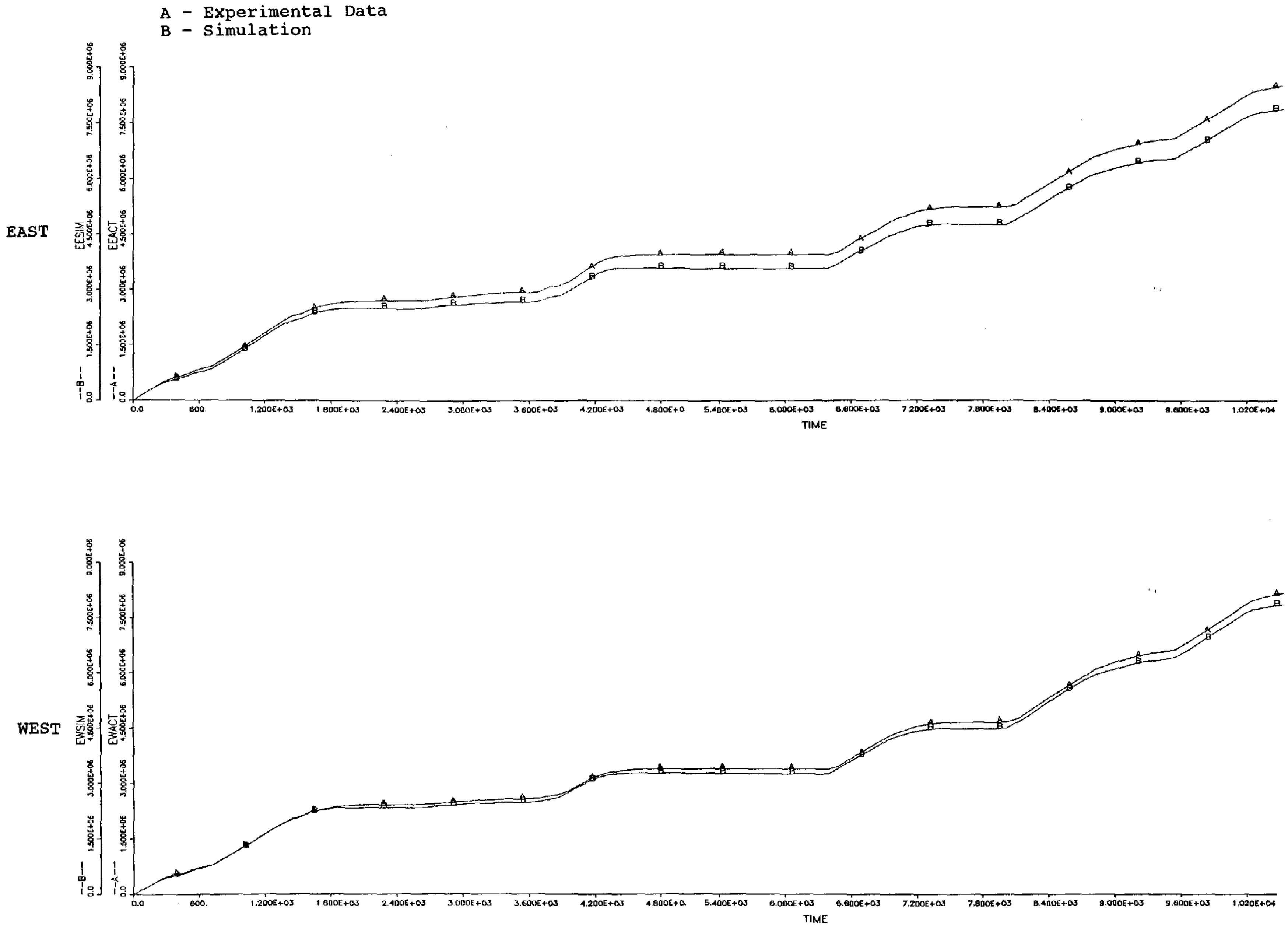

Figure 3-7 Comparison of Actual and Simulated Response of the Energy Exiting the Receiver During Natural Cloud Transients (Btus)

Chapter 4

Summary, Conclusions, and Recommendations

A PC-based simulation of the thermal energy subsystem of the Molten-Salt-Subsystem-Component-Test Experiment (MSSCTE) has been developed. The cavity-type 5-MW_t receiver, the thermal storage systems, accompanying valves and controllers were modeled.

Two user interfaces are provided with the model to enhance user friendliness and to facilitate technology transfer between Sandia Laboratories and the central receiver community. The color graphics interface uses an Enhanced Graphic Display with 10 color slides. These slides depict piping and instrument drawings and have simulation values overlaid. Many variables are available for view. Also included are several menus, which allow the user to configure simulation parameters, induce failures, and change controller gains and set points. The analyzer interface displays information in a tabular format and allows the user to continuously monitor any of the desired simulation variables.

The simulator was validated against actual plant test data. The simulator produced a good prediction of actual receiver performance during 30 minutes of simulated clouds and an excellent prediction during 3 hours of natural clouds. In the latter case, the error in total energy prediction was approximately 5 percent. A small bias was noted in the simulator prediction during rapid heating and cooling of the receiver. This bias was attributed to the fact that we did not model the thermal inertia, which is inherent to the cavity structure that surrounds the receiver.

With the simulator validated and the test program of the 5-MW_t MSSCTE receiver now completed, the next logical step is to modify the simulator to mimic the next-generation salt-in-tube receiver. Two U.S. utility companies have recently proposed retrofitting the Solar One pilot plant with a salt-in-tube receiver rated at 36 MW_t or repowering the Saguaro power plant with a 30-MW_e salt receiver system (L. Stoddard 1988). These projects would be predecessors to commercial-scale plants rated at 100 or 200 MW_e (Arizona Public Service and Pacific Gas and Electric, 1988). The modified simulator could be used to perform the following types of studies for these plants:

1. The simulator could be used in conjunction with the SOLERGY computer code (M. Stoddard et. al. 1987) to obtain annual energy predictions. The SOLERGY code is capable of producing a good estimate of annual energy if the user provides accurate estimates of code input parameters (Alpert and Kolb 1988). Input parameters are typically derived from the results of dynamic simulators and experimental data.

2. An optimal control approach during cloud transients could be identified. This approach would weigh the merits of optimizing energy collection versus optimizing the lifetime of the receiver. The lifetime of the receiver can be extended by minimizing the thermal stresses on the panels caused by rapid changes in incident solar flux. An algorithm that calculates thermal strains and reductions in receiver lifetime caused by cloud transients has recently been developed at Sandia (Grossman 1988). This algorithm could be included in the simulator.

3. The response of the systems to various component failures could also be studied. This would help define margins of safety, requirements of the safe-shutdown systems, and the locations where component redundancy should be placed.

References

Alpert, D. J. and Kolb, G. J., Performance Evaluation of the Solar One Power Plant as Simulated by the SOLERGY Computer Code, SAND88-0321, Sandia National Laboratories, Albuquerque, NM, April 1988.

Arizona Public Service Company, Alternate Utility Team, Utility Solar Central Receiver Study, DOE/AL/38741-2, Phoenix, AZ, September 1988.

Arizona Public Service Company, Preliminary Design of a Solar Central Receiver for a Site-Specific Repowering Application (Saguaro Power Plant), Cooperative Agreement DE-FC03-82SF11675-1, Phoenix, AZ, September 1983.

Chavez, J. M. and Smith, D., A Final Report on the Phase 1 Testing of a Molten-Salt Cavity Receiver, SAND87-2290, Sandia National Laboratories, Albuquerque, NM, 1988.

E^2 Consulting, System Simulation Language User's Guide, SYSL/M Version 2.0, Poway, CA, 1987.

Grossman, J. W., Sandia National Laboratories, Albuquerque, Personal communication, 1988.

Kistler, B. L., A User's Manual for DELSOL3: A Computer Code for Calculating the Optical Performance and Optimal System Design for Solar Thermal Central Receiver Plants, SAND86-8018, Sandia National Laboratories, Livermore, CA, 1986.

Kolb, G. J., Nikolai, U., Performance Evaluation of Molten Salt Thermal Storage Systems, SAND87-3002, Sandia National Laboratories, Albuquerque, NM, 1988.

Pacific Gas and Electric Company, Solar Central Receiver Technology Advancement for Electric Utility Applications, Phase 1 Topical Report, Report 007.2-88.2, September, 1988.

PDA Engineering, PDA/PATRAN-G User's Guide, Santa Ana, CA, 1984.

Sayers, D. D., CAVITY - A Computer Code to Couple Radiative Exchange in a Cavity-Type Receiver with the Conductive-Convective Exchange to the Working Fluid, Internal Memorandum RS8245/20, Sandia National Laboratories, Livermore, CA.

Siebers, D. L. and Kraabel, J. S., Estimating Convective Energy Losses from Solar Central Receivers, SAND84-8717, Sandia National Laboratories, Livermore, CA, 1984.

Southern California Edison Company, Solar 100 Conceptual Study Final Report, Rosemead, CA, August 1982.

Stoddard, L. E., "Letter to John Holmes (Sandia) from Larry Stoddard (Black and Veatch)," October 5, 1988.

Stoddard, M. C., S. E. Faas, C. J. Chiang, J. A. Dirks, SOLERGY-A Computer Code for Calculating the Annual Energy from Central Receiver Plants, SAND86-8060, Sandia National Laboratories, Livermore, CA, 1987.

Appendix A

Hardware and Software Requirements

Minimum hardware requirements for the analyzer are an IBM-PC-AT; Compaq portable II, or equivalent compatible computer equipped with:

- 80287 Coprocessor (options 4, 8, 10 MHz)
- 640K Ram
- Graphic printer
- Enhanced graphics board
- Hard disk

In addition, the simulator requires

- Enhanced Color Display monitor

An advanced user may choose to purchase a mouse and Microsoft Paintbrush which allows creation of new, or modification of existing, color display slides.

Minimum software requirements include:

- DOS operating system (version 3.0 or later)
- SYSL (SYstem Simulation Language)
- Ryan McFarland Fortran Compiler (version 2.0
- or later)
- Microsoft linker (version 2.3 or later)
- Microsoft library manager

The simulator requires:

- IBM Graphics Toolkit Device Drivers

All are easily obtainable, with the possible exception of SYSL. This software can be obtained from

E^2 Consulting
P. O. Box 1182
Poway, CA 92064.

A floppy disk that contains the dynamic simulator of the cavity receiver, as well as a user's manual, can be obtained from

Greg Kolb
Solar Energy Department
Sandia National Laboratories
P. O. Box 5800
Albuquerque, New Mexico 87185.

UNLIMITED RELEASE
INITIAL DISTRIBUTION

U.S. Department of Energy (6)
Forrestal Building
Code CE-314
1000 Independence Avenue, SW
Washington, DC 20585
Attn: H. Coleman
S. Gronich
F. Morse
M. Scheve
R. Shivers
T. Wilkins

U.S. Department of Energy
Forrestal Building
Code CE-33
1000 Independence Avenue, SW
Washington, DC 20585
Attn: C. Carwile

U. S. Department of Energy
CE-1, Forrestal
1000 Independence Avenue, SW
Washington, DC 20585
Attn: D. Fitzpatrick

U.S. Department of Energy (2)
Albuquerque Operations Office
P.O. Box 5400
Albuquerque, NM 87115
Attn: D. Graves
G. Tennyson

U.S. Department of Energy
San Francisco Operations Office
1333 Broadway
Oakland, CA 94612
Attn: R. Hughey

Advanced Thermal Systems
7600 East Arapahoe
Suite 215
Englewood, CO 80112
Attn: D. Gorman

Allegheny Ludlum Steel
Market and Product Development
Alabama and Pacific Avenues
Brackenridge, PA 15014
Attn: Joseph M. Hunt

Allegheny Ludlum Steel
80 Valley St.
Wallingford, CT 06492
Attn: John J. Halpin

Analysis Review & Critique
6503 81st Street
Cabin John, MD 20818
Attn: C. LaPorta

Arizona Public Service Company
P.O. Box 53999
Phoenix, AZ 85072-3999
Attn: J. McGuirk

Arizona Solar Energy Office
Dept. of Commerce
1700 W. Washington, 5th Floor
Phoenix, AZ 85007
Attn: Dr. Frank Mancini

Asinel
Ctra. Villaviciosa
de Odón a Móstoles
Km 1,700
28935 Móstoles
Madrid Spain
Attn: Jesús M. Mateos

Atlantis Energy Ltd.
Thunstrasse 43a
3005 Bern, Switzerland
Attn: Mario Posnansky

Babcock and Wilcox
91 Stirling Avenue
Barberton, OH 44203
Attn: D. Young

Battelle Pacific Northwest
Laboratory
P.O. Box 999
Richland, WA 99352
Attn: T. A. Williams

Bechtel National, Inc. (4)
50 Beale Street
50/15 D8
P. O. Box 3965
San Francisco, CA 94106
Attn: P. DeLaquil
B. Kelly
J. Egan
R. Leslie

Black & Veatch Consulting
Engineers (3)
P.O. Box 8405
Kansas City, MO 64114
Attn: J. C. Grosskreutz
J. E. Harder
L. Stoddard

Bomin Solar
Industriestr. 8
D-7850 Lorrach
Federal Republic of Germany
Attn: Dr. Hans Jurgen
Kleinwachter

Tom Brumleve
1512 Northgate Road
Walnut Creek, CA 94598

California Energy Commission
1516 Ninth Street, M-S 43
Sacramento, CA 95814
Attn: A. Jenkins

California Polytechnic University
Dept. of Mechanical Engineering
3801 West Temple Ave.
Pomona, CA 91768-4062
Attn: W. Stine

California Public Utilities
Comm.
Resource Branch, Room 5198
455 Golden Gate Avenue
San Francisco, CA 94102
Attn: T. Thompson

Center for Energy and
Environmental Research
GPO Box 3682
San Juan, PR 00936
Attn: Director

Centro Investigations
Energetica (2)
Medroansental Technologie
(CIEMAT)
Avda. Complutense, 22
28040 Madrid
SPAIN
Attn: F. Sanchez
M. Romero

DLR EN-TT (2)
Institute for Technical
Thermodynamics
Pfaffenwaldring 38-40
7000 Stuttgart 80
Federal Republic of Germany
Attn: Dr. C. Winter
Dipl. Ing R. Buck

DLR
Linder Hoehe
5000 Cologne 90
Federal Republic of Germany
Attn: Dr. Manfred Becker

El Paso Electric Company
P.O. Box 982
El Paso, TX 79946
Attn: J. E. Brown

Electric Power Research
Institute (2)
P.O. Box 10412
Palo Alto, CA 94303
Attn: J. Bigger
E. DeMeo

Engineering Perspectives
20 19th Avenue
San Francisco, CA 94121
Attn: John Doyle

ESSCOR Corporation (5)
512 Via de la Valle, Suite 311
Solana Beach, CA 92075

Flachglas Solartechnik GmbH
Muhlengasse 7
D-5000 Koln 1
Federal Republic of Germany
Attn: Joachim Benemann

Flachglas Solartechnik GmbH
Sonnesstr. 25
D-8000 Munchen 1
Federal Republic of Germany
Attn: Dr. Michael Geyer

Foster Wheeler Solar Development
Corporation (2)
12 Peach Tree Hill Road
Livingston, NJ 07039
Attn: S. F. Wu
R. Zoschak

Georgia Institute of Technology
GTRI/EMSL Solar Site
Atlanta, GA 30332
Attn: T. Brown

Georgia Power
7 Solar Circle
Shenandoah, GA 30265
Attn: Ed. Ney

Leo Gutierrez
434 School Street
Livermore, CA 94550

HGH Enterprises, Inc.
23011 Moulton Parkway
Suite C-13
Laguna Hills, CA 92653
Attn: Dick Holl

Interatom GmbH (2)
P. O. Box
D-5060 Bergisch-Gladbach
Fededral Republic of Germany
Attn: M. Kiera
W. Meinecke

Lawrence Berkeley Laboratory
MS 90-2024
One Cyclotron Road
Berkeley, CA 94720
Attn: Arlon Hunt

Los Angeles Department of Water
and Power
Alternate Energy Systems
Room 661A
111 North Hope Street
Los Angeles, CA 90012
Attn: Bill Engels

Luz International (2)
924 Westwood Blvd.
Los Angeles, CA 90024
Attn: D. Kearney
M. Lotker

Meridian Corporation
4300 King St.
Suite 400
Alexandria, VA 22302-1508
Attn: D. Kumar

MITI
Electrotechnical Laboratory
Solar Energy Applications
Section
1-1-4 Umezono, Tsukuba
Ibaraki 305, Japan
Attn: Koichi Sakuta

Nevada Power Co.
P. O. Box 230
Las Vegas, NV 89151
Attn: Mark Shank

ORMAT TURBINES LTD.
New Industrial Area
P. O. B. 68 Yavne,
70650 Israel
Attn: Avi Ben Har

Peerless Winsmith, Inc.
172 Eaton St.
P. O. Box 530
Springville, NY 14141
Attn: W. Hellar

Platforma Solar de Almeria
Aptdo. 7
Tabernas (Almeria)
E-04200 Spain

Public Service Company of
New Mexico
M/S 0160
Alvarado Square
Albuquerque, NM 87158
Attn: T. Ussery
A. Martinez

Pacific Gas and Electric
Company (3)
3400 Crow Canyon Road
San Ramon, CA 94526
Attn: G. Braun
T. Hillesland
B. Norris

Polydyne, Inc.
1900 S. Norfolk Street, Suite 209
San Mateo, CA 94403
Attn: P. Bos

PSI (2)
CH-5303 Wurenlingen
Switzerland
Attn: W. Durish
P. Kesselring

Public Service Company of Colorado
System Planning
5909 E 38th Avenue
Denver, CO 80207
Attn: D. Smith

Ramada Energy Systems Ltd.
1421 S. McClintock Drive
Tempe, AZ 85281
Attn: R. Bingman

Gene Riley
7200 Montgomery N.E.
Suite 169
Albuquerque, NM 87109

San Diego Gas and Electric
Company
P.O. Box 1831
San Diego, CA 92112
Attn: R. Figueroa

SCE
P. O. Box 800
Rosemead, CA 91770
Attn: W. vonKleinSmid

Schlaich, Bergermann & Partner
Hohenzollernstr. 1
D-7000 Stuttgart 1
Federal Republic of Germany
Attn: Wolfgang Schiel

Sci-Tech International
Advanced Alternative Energy
Solutions
5673 W. Las Positas Boulevard
Suite 205
P.O. Box 5246
Pleasanton, CA 84566
Attn: Ugur Ortabasi

Science Applications
International Corporation
10260 Campus Point Drive
San Diego, CA 92121
Attn: B. Butler

Solar Energy Research
Institute (6)
1617 Cole Boulevard
Golden, CO 80401
Attn: B. Gupta
L. M. Murphy
J. Anderson
N. Weaver
W. Short
T. Wendelin

Solar Kinetics, Inc.
P.O. Box 540636
Dallas, TX 75354-0636
Attn: J. A. Hutchison

Solar Power Engineering Company
P.O. Box 91
Morrison, CO 80465
Attn: H. C. Wroton

Solar Stream
P. O. Box 32
Fox Island, WA 98333
Attn: D. Wood

Southern California Edison
P.O. Box 325
Daggett, CA 92327
Attn: C. Lopez

Stearns Catalytic Corporation
P.O. Box 5888
Denver, CO 80217
Attn: T. E. Olson

Stone and Webster Engineering
Corporation
P.O. Box 1214
Boston, MA 02107
Attn: R. W. Kuhr

Sulzer Bros, Ltd.
New Technologies
CH-8401 Winterthur
Switzerland
Attn: Hans Fricker, Manager

Robert G. Surette
2253 Micheltorena St.
Los Angeles, CA 90039

Tom Tracey
6922 South Adams Way
Littleton, CO 80122

United Solar Tech, Inc.
3434 Martin Way
Olympia, WA 98506
Attn: R. J. Kelley

University of Arizona
Engineering Experimental Station
Harvil Bldg., Room 151-D
Tucson, AZ 85721
Attn: Don Osborne

University of Houston (3)
Solar Energy Laboratory
4800 Calhoun
Houston, TX 77704
Attn: A. F. Hildebrandt
L. Vant-Hull
C. Pitman

University of Utah
Mechanical and Industrial
Engineering
Salt Lake City, UT 84112
Attn: B. Boehm

Eric Weber
302 Caribbean Lane
Phoenix, AZ 85022

WG Associates
6607 Stonebrook Circle
Dallas, TX 75240
Attn: V. Goldberg

3M Corp.
3M Center
Building 207-1W-08
St. Paul, MN 55144
Attn: B. A. Benson

3141-1	S. A. Landenberger (5)
3151	W. I. Klein (3)
3154-1	C. L. Ward (8) For DOE/OSTI
6200	V. L. Dugan
6210	B. W. Marshall
6215	K. R. Boldt
6215	W. A. Couch
6215	J. V. Otts
6216	J. T. Holmes
6217	D. R. Adkins
6217	J. M. Chavez
6217	J. M. Diggs
6217	P. C. Klimas
6217	G. J. Kolb (10)
6217	D. F. Menicucci
8024	P. W. Dean
8133	A. C. Skinrood
8165	C. L. Mavis
8524	J. R. Wackerly
9133	E. R. Hoover

☆ U.S. GOVERNMENT PRINTING OFFICE: 1989—673-049/81033